Doctoral Thesis

Catalysis involving surface hydroxy group and the catalyst design for its utilization

Feb. 2021

Kota MURAKAMI

Catalysis involving surface hydroxy group and the catalyst design for its utilization

Feb. 2021

Waseda University
Graduate School of Advanced Science and Engineering
Department of Applied Chemistry,
Research on Catalytic Chemistry

Kota MURAKAMI

Table of Contents

Chapter 1 General Introduction

1.1. Catalytic reaction involving H^+ migration

The migration of H atoms over metal oxide surfaces plays a key role in various reactions, including hydrogenation of hydrocarbon, [1–3] CO_2 reduction, [4–6] and NH_3 synthesis. [7] Utilization of the migration is not limited to catalytic reactions. It is also a central subject for hydrogen storage, [8, 9] sensors, and fuel cells. [10, 11]

Conventionally, the migration is induced by the concentration gradient (*i.e.* hydrogen spillover). The H atoms migrate from hydrogen-rich surfaces such as active metals to adjacent hydrogen-poor surfaces such as metal oxides. [12, 13] Khoobiar *et al.* first reported observations of hydrogen spillover in 1964. [14] They found that WO_3 was reduced by H_2 into H_xWO_3 at low temperature (323 K) only when WO_3 is physically contacted with Pt/γ-Al_2O_3. This observation suggests hydrogen spillover from Pt particles onto WO_3. After this publication, many researchers devoted much attention to studying hydrogen spillover. A comprehensive review of research on the subject of hydrogen spillover was written by Prins in 2012. [13] He introduced some points of criticism of the hydrogen spillover onto irreducible metal oxides such as Al_2O_3 and SiO_2. Reducible metal oxides enable fast hydrogen spillover by a coupled proton-electron transfer mechanism, as shown in Fig. 1.1. [15–21] This mechanism is not allowed over irreducible metal oxides. This controversy derives from the lack of in-depth knowledge for migration mechanism and proof of the catalysis involving migrating H atoms. After the report by Prins, investigation using well-fabricated samples, *operando* spectroscopy and Density Functional Theory (DFT) have been researched enthusiastically. [17, 20–25]

Moreover, our group has investigated the active facilitation of H^+ migration using an electric field. [26–29] Such surface H^+ conduction is called surface protonics. Surface protonics over metal oxides is an important factor in activating the decoupling of strong bonds such as C–H bond in CH_4 and N≡N bond in N_2 at the low-temperature region. This finding brought the migration of H^+ over metal oxide surfaces in the spotlight as a fundamentally important research theme in the field of low-temperature catalytic reactions. In this thesis, we specifically examined a detailed understanding of the catalysis related to surface protonics and tuning of the catalytic performance based on electrochemical analysis and DFT calculations. This chapter presents a summary of the catalytic reactions related to H^+ conduction with and without facilitation by the electric field. Subsequently, sophisticated analysis techniques for the conduction are introduced. Finally, the aims of this thesis are presented.

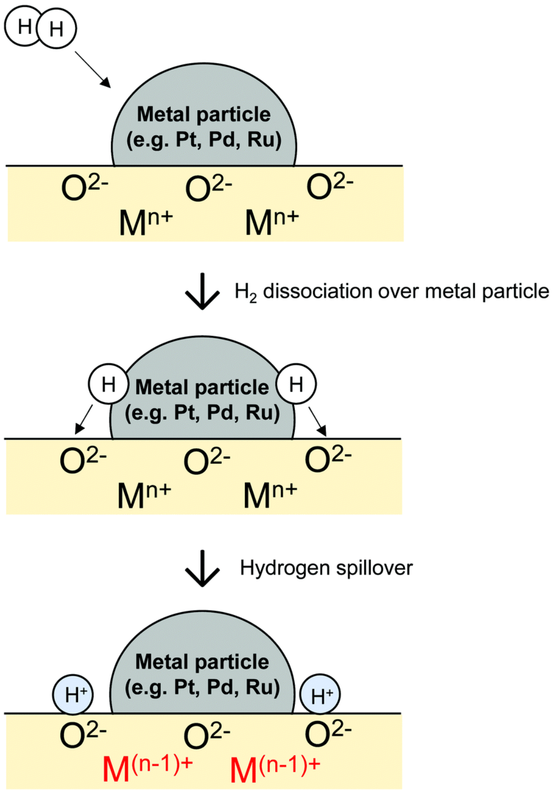

Figure 1.1. Schematic image of hydrogen spillover by coupled-proton electron transfer mechanism. Copyright 2020 RSC publishing.

1.2. Recent studies of catalytic reactions related to hydrogen spillover

Hydrogen spillover has been applied to various catalytic reactions. Its advantages are attributed mainly to two processes. One process is the supply of H atoms to sites that cannot dissociate H_2. Sections 1.2.1–1.2.3 introduce such benefits. The other process is the elimination of H atoms from sites inhibited by excessive amounts of H atoms, as presented in section 1.2.4.

1.2.1. Enhancement of atomic efficiency

Noble metal nanoparticles are well known to be active in various catalytic reactions. However, high atomic efficiency is necessary because of their scarcity on Earth. Recently, many researchers have particularly examined production of smaller supported noble metal particles into a single-atom level for enhancing atomic efficiency. Well-fabricated reviews of single-atom catalysts (SAC) were reported by the Liu group. [30, 31] Those catalysts exhibited high activities for several reactions such as CO oxidation, [32] water–gas shift reaction, [33] and O_2 or CO_2 electroreduction. [34, 35] In contrast, those catalysts cannot function for ketone/aldehyde reduction, which is an important reaction in chemical engineering. The low reaction rates of H_2 dissociation over single atoms cause this difficulty. H_2 heterogeneously dissociates over single-atom catalysts. The barrier of heterolysis is much higher than that of homolysis over metal nanoparticles. Yan *et al.* reported the H_2 reaction order as around 1.2 for 1,3-butadiene hydrogenation over Pd single-atom catalysts, suggesting H_2 dissociation as the rate-determining step. [36]

Kuai *et al*. overcame this difficulty using hydrogen spillover. [1] They loaded Pd single atoms (Pd_1) and Pd nanoparticles (Pd_{NPs}) together over mesoporous TiO_2 (Pd_{1+NPs}/TiO_2) using a spray-assisted method developed by the same group. [37, 38] They compared the performances of Pd_{1+NPs}/TiO_2, Pd_1/TiO_2 and Pd_{NPs}/TiO_2 for 4-methylacetophenone (MAP) hydrogenation. Consequently, Pd_{1+NPs}/TiO_2 exhibited the highest atomic efficiency of Pd among all catalysts. The schematic image for this reaction is presented in Fig. 1.2. In terms of the activity per exposed Pd atom (turn over frequency, TOF), Pd_{1+NPs}/TiO_2 and Pd_{NPs}/TiO_2 exhibited similar values (4361 h^{-1} for Pd_{1+NPs}/TiO_2 and 4565 h^{-1} for Pd_{NPs}/TiO_2), even though Pd_1/TiO_2 exhibited much lower TOF (645 h^{-1}). Those data revealed a synergetic role of Pd_1 and Pd_{NPs}. Pd_{NPs} functions as an active site for H_2 dissociation into H atoms. The obtained H atoms migrate over TiO_2 surface and react with ketone/aldehydes at Pd_1. Therefore, Pd_1 can catalyze hydrogenation of ketone/aldehyde by virtue of the supply of H atoms from Pd_{NPs}. As described above, hydrogen spillover can extend the utility of SACs. Reportedly, specific electronic states of single atoms caused high reactivity [4, 32] although the TOF over Pd_1 and Pd_{NPs} did not change so much in this report. Therefore, this report from Kuai *et al*. can expand the utilities of SACs not only for enhancing atom efficiency but also for the utilization of its novel reactivity at single-atom sites.

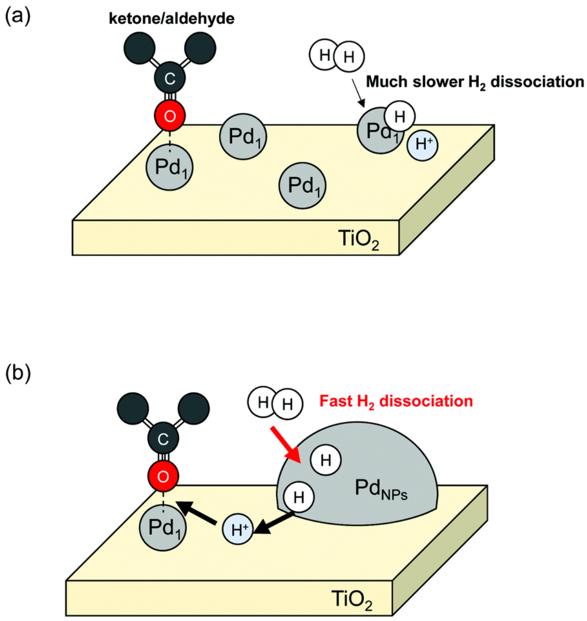

Figure 1.2. Schematic image of the ketone/aldehyde hydrogenation over two types of catalysts. (a) Pd_1/TiO_2 and (b) Pd_{1+NPs}/TiO_2. Copyright 2020 RSC publishing.

1.2.2. Selective hydrogenation

Hydrogen spillover engenders the formation of two separated reaction sites over one catalyst surface (*i.e.* dual site catalysts or tandem catalysts). Usage of this separation is studied for selective hydrogenation of hydrocarbons.

Campisi *et al*. reported that Pd/NiO can convert furfural into tetrahydrofurfuryl alcohol (72%) selectively, although furfuryl alcohol (68%) was formed over Pd/TiO_2. [2] Furfural is a promising platform molecule for various products in biorefineries. Highly selective conversion using tailored catalysts is demanded. Without loading of Pd, no marked difference of activities was observed between NiO and TiO_2. TiO_2 showed no observable activity without Pd loading. NiO also exhibited trivial activity without Pd. In contrast, those two catalysts exhibited completely different performance when Pd was loaded. First, Pd-loaded NiO exhibited high activity. However, the loading amount did not influence activities. Actually, 0.1wt%Pd/NiO exhibited almost identical activity as 1wt%Pd/NiO. In contrast, Pd loading amount had great influence on the activities when TiO_2 was used as a support; 0.1wt%Pd/TiO_2 exhibited much smaller conversion than 1wt%Pd/TiO_2. Those results showed the surface of NiO functions as an active site when H atoms were supplied from Pd particles. Reportedly, the selectivity of furfural hydrogenation was governed strongly by the adsorption structures of the reactant at reaction sites. [39, 40] Therefore, Campisi *et al*. investigated the adsorption structures of furfural over Pd, NiO, and TiO_2 using DFT calculations. A noteworthy difference in adsorption structures over reaction sites was confirmed. Although the roles of the respective adsorption structures were not considered in-depth, they indicated that the parallel adsorption of furan ring and alcohol group over NiO (Fig. 1.3) as crucially important for the selective formation of tetrahydrofurfuryl alcohol. In this manner, hydrogen spillover enables the use of metal oxide surfaces as active sites for various reactions.

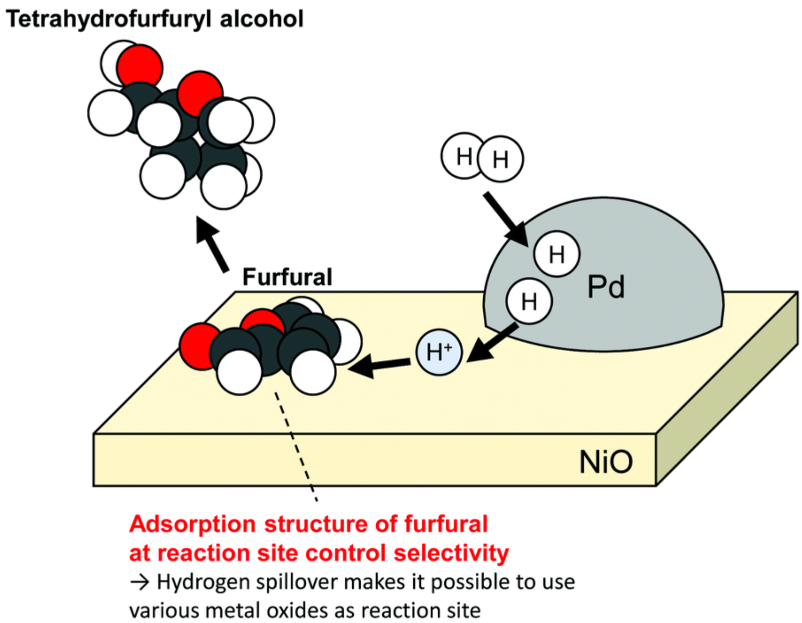

Figure 1.3. Schematic image of furfural hydrogenation over NiO using hydrogen spillover. Copyright 2020 RSC publishing.

Preparation of well-fabricated catalysts that have completely separated two active sites have been researched for selective hydrogenation. Xue *et al*. prepared a Ru/TiO_2 catalyst encapsulated by a porous TiO_2 ((Ru/TiO_2)@*p*-TiO_2) for this purpose. This catalyst exhibited selective hydrogenation of benzene to cyclohexene (benzene conversion, 98.1%; cyclohexene selectivity, 76.6%). [3] The partial hydrogenation of benzene is important in the formation of cyclohexene, which is a fundamental intermediate for various fine chemicals because of its reactive C=C bond. Ru-based catalysts are known as famous candidates. However, its selectivity is limited because Ru favors subsequent hydrogenation into cyclohexane. [41, 42] Xue *et al*. attempted to suppress deep hydrogenation by covering the Ru surface with porous TiO_2. Figure 1.4 portrays a schematic image of selective hydrogenation of benzene using (Ru/TiO_2)@*p*-TiO_2. They conducted H_2-TPD and CO-TPD to evaluate the diffusion of reactants through pores in the mesoporous TiO_2 shell. Results show that only H_2 can reach interior Ru particles. Other reactants are unable to access Ru because of inhibition by the TiO_2 shell. During hydrogenation, H atoms are formed over interior Ru and are supplied to TiO_2 surface. The H atoms migrate toward the external surface of TiO_2 shell. Then, the H atoms at the external surface react with hydrocarbons. The hydrogenation proceeds selectively over TiO_2 shell because of much weaker adsorption of cyclohexene and high barriers of cyclohexene hydrogenation over the TiO_2 surface.

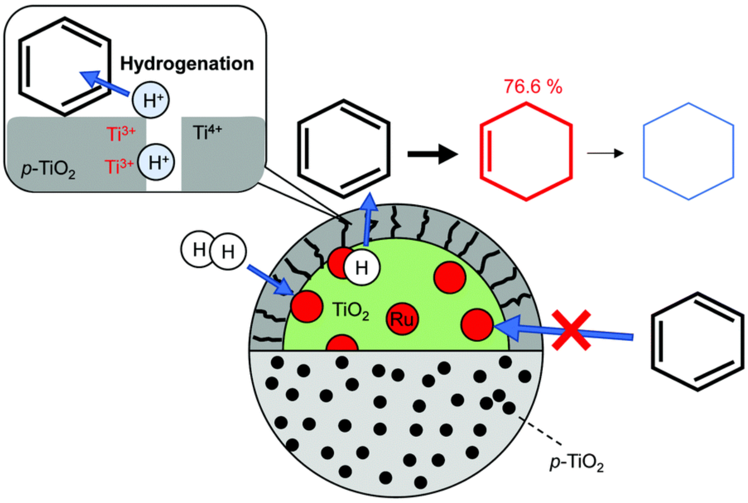

Figure 1.4. Schematic image of selective hydrogenation of benzene to cyclohexene over Ru/TiO_2 catalyst encapsulated by a porous TiO_2 (Ru/TiO_2)@*p*-TiO_2. Copyright 2020 RSC publishing.

1.2.3. Change of reaction mechanism by heterocation doping because of enhanced hydrogen migration

Heterocation doping into metal oxides is expected to have a strong influence on hydrogen spillover. Franken *et al*. reported that Mn doping into $CoAl_2O_4$ affected the hydrogen spillover, resulting in high CO_2 methanation activity. [5] CO_2 is well known as a main component of greenhouse gases. Investigation of CO_2 capture and storage (CCS) or capture and utilization (CCU) is a central research theme. The extremely complex CO_2 reduction mechanism is controversial. In this section, their details will not be shown. Well summarized reviews have explained them. [43, 44] Franken *et al*. investigated the utilization of $CoMn_xAl_{2-x}O_4$ for this reaction. This catalyst was pre-reduced for the formation of Co nanoparticles that work as active sites. They revealed that Mn doping enhanced the CO_2 adsorption ability of $CoAl_2O_4$. Additionally, long-range hydrogen spillover was facilitated by enhancement of redox ability by Mn doping. The activation energy of CO_2 reduction was reduced by those Mn doping effects (108 kJ/mol for $CoAl_2O_4$, and 69 kJ/mol for $CoMn_{0.5}Al_{1.5}O_4$). Furthermore, *Operando* Diffuse reflectance infrared Fourier transform spectroscopy (DRIFTS) measurements revealed a change of reaction sites and mechanisms by virtue of the Mn incorporation, as shown in Fig. 1.5.

Without Mn doping, Co surfaces worked solely as CO_2 reduction sites, with CO formed as a by-product. In contrast, with Mn doping, CO_2 was converted also over metal oxides *via* formate species using H atoms supplied from Co nanoparticles. The CO formation was suppressed because of the change of reaction sties by Mn doping. This finding concealed that heterocation doping can expand the possibilities of metal oxide usage for catalysis involving hydrogen spillover.

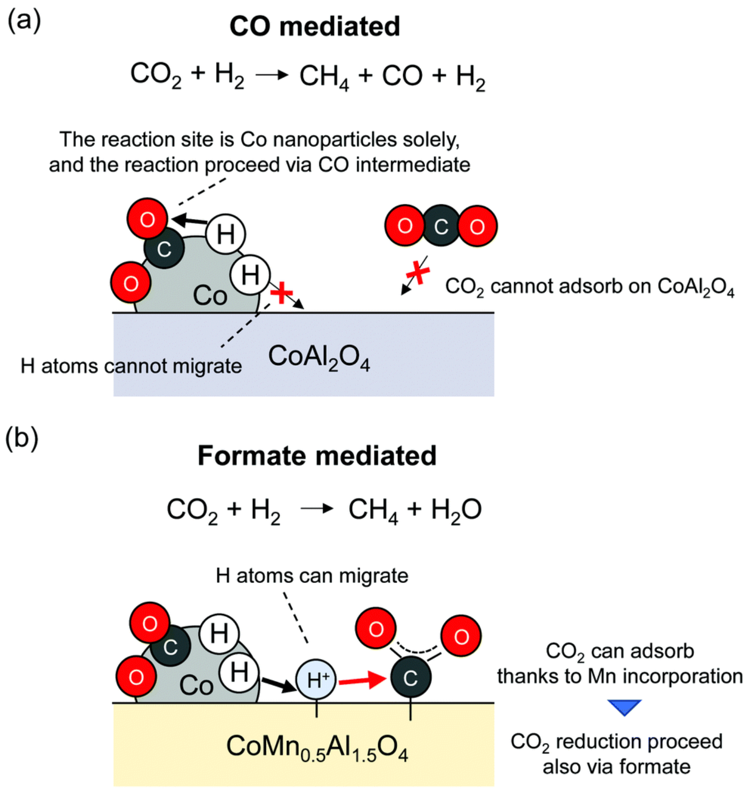

Figure 1.5. Schematic image of CO_2 methanation mechanism (a) over $CoAl_2O_4$ without hydrogen spillover, and (b) over $CoMn_{0.5}Al_{1.5}O_4$ with hydrogen spillover. Copyright 2020 RSC Publishing.

1.2.4. Suppression of hydrogen poisoning

Wu *et al*. investigated the influences of hydrogen spillover on NH_3 synthesis. [7] Many researchers have been keen on NH_3 synthesis in anticipation of its use as a hydrogen carrier. Ozaki and Aika *et al*. found out that Ru-based catalysts exhibited much higher intrinsic activities than doubly promoted iron catalyst ($Fe\text{-}Al_2O_3\text{-}K_2O$), which is used widely in conventional plants. [45, 46] Various Ru-based catalysts, which exhibited markedly high activities, have been developed after their reports. [47–50] Reportedly, N_2 direct dissociation is the rate-determining step over a Ru surface. [51] Furthermore, Ru surfaces are prone to be poisoned by H atoms under high H_2 pressure. Then, H_2 reaction orders for NH_3 synthesis are usually negative over Ru-based catalysts. [52, 53] Therefore, the suppression of H_2 poisoning over Ru surface is fundamentally important. Wu *et al*. reported that the H atoms over Ru surface can be removed using polar MgO (111) instead of MgO (110) or (100). [7] Actually, Ru/MgO (111) exhibited a much higher rate of NH_3 synthesis than with either Ru/MgO (110) or Ru/MgO (100). Regarding reaction orders, the N_2 reaction orders were almost identical among all catalysts (Ru/MgO (111): 0.9, Ru/MgO (110) : 0.9, Ru/MgO (100) : 0.8). In contrast, the H_2 reaction order changed considerably, and Ru/MgO (111) showed a positive value (Ru/MgO(111): 0.6, Ru/MgO (110): -0.2, Ru/MgO (100): -0.5). Consequently, results suggest that the suppression of hydrogen poisoning led to a high NH_3 synthesis rate over Ru/MgO(111). In line with several characterizations (^{1}H NMR, *in-situ* FT-IR measurement, and DFT calculations), it was revealed that polar MgO (111) strongly binds H atoms. Therefore, they indicated that stability of H atoms over supports result in the suppression of hydrogen poisoning over a Ru surface, as shown in Fig. 1.6. This report presents no discussion of the net migration of H atoms and their desorption after migration. To reduce H atom coverage over Ru, the points described above must be considered carefully. Therefore, prudent consideration must be made of hydrogen migration effects on H atom coverage over metal particles using sophisticated techniques.

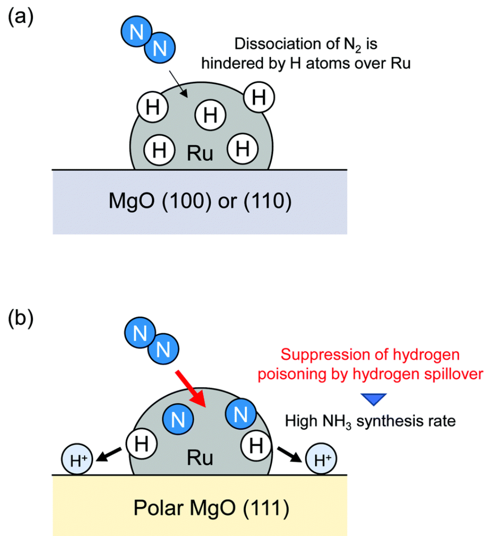

Figure 1.6. Schematic image of hydrogen poisoning suppression over Ru by hydrogen spillover. Copyright 2020 RSC Publishing.

1.3. Catalytic reaction involving active H^+ migration: surface protonics in the electric field

We have been successful in enhancing catalytic activities using an electric field. [26–29] Hereinafter, "the catalytic reactions in the electric field" stands for the catalytic reactions invoked by the application of direct current into semiconductor, and the above operation is referred as "applying the electric field" or "~ in the electric field". We used two electrodes attached to catalyst granules for applying direct current. A schematic image of the reactor is shown in Fig. 1.7. In this method, current density plays an important role in the enhancement of the catalytic activities. [54] The Faradaic efficiency in this process exceeds 1.0 which is the limit of conventional electrolytic synthesis. [55] Hence, the phenomena occurring during the catalytic reactions in the electric field are totally different from those in conventional electrochemical reactions. We have confirmed that the increase in catalyst bed temperatures due to Joule heating would not be an intrinsic effect of the application of the electric field using Near infrared (NIR) camera and extended x-ray absorption fine structure (EXAFS) measurements. Those methods cannot detect the existence of heating at local sites such as a few percent of the active sites. However, the catalysts, which do not exhibit catalytic activities even when heated to high temperatures, showed high performances in the electric field. [56] Hence, we considered that the catalytic reactions in the electric field cannot be explained by existing disciplines. Therefore, we have applied this method to various catalytic reactions and revealed the peculiar reaction mechanisms. In this section, the main works related to surface protonics are summarized.

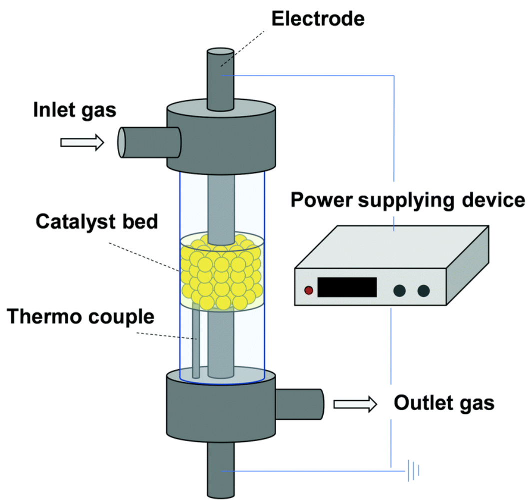

Figure 1.7. Illustration of the apparatus for catalytic reactions in the electric field. Copyright 2020 RSC Publishing.

1.3.1. Steam reforming of CH_4

We have applied the approach described above to steam reforming of various compounds (*e.g.* CH_4, [57-61] dimethyl ether, [62] toluene, [63] ethanol [64]). As a result, we obtained much higher activities in a low-temperature region by virtue of assistance with an electric field. Furthermore, we have reported details of benefits of electric fields using CH_4 steam reforming as a case reaction. Steam reforming of CH_4 is a common process for H_2 production. The obtained H_2 is used for several reactions including oil refining and NH_3 synthesis. First, we conducted *operando*-DRIFTS measurements using 1wt%Pd/CeO_2 as a sample. Figure 1.8 shows the spectra obtained with and without the electric field. As a result, a peak was observed specifically at 855 cm^{-1} in the electric field. This peak can be assigned to the rocking vibration of H_2O adsorbed over CeO_2, [65] suggesting that the electric field facilitated surface protonics *via* the Grotthuss mechanism. [10, 11, 66] This surface protonics played an important role in enhancing the conversion of CH_4 at low temperatures.

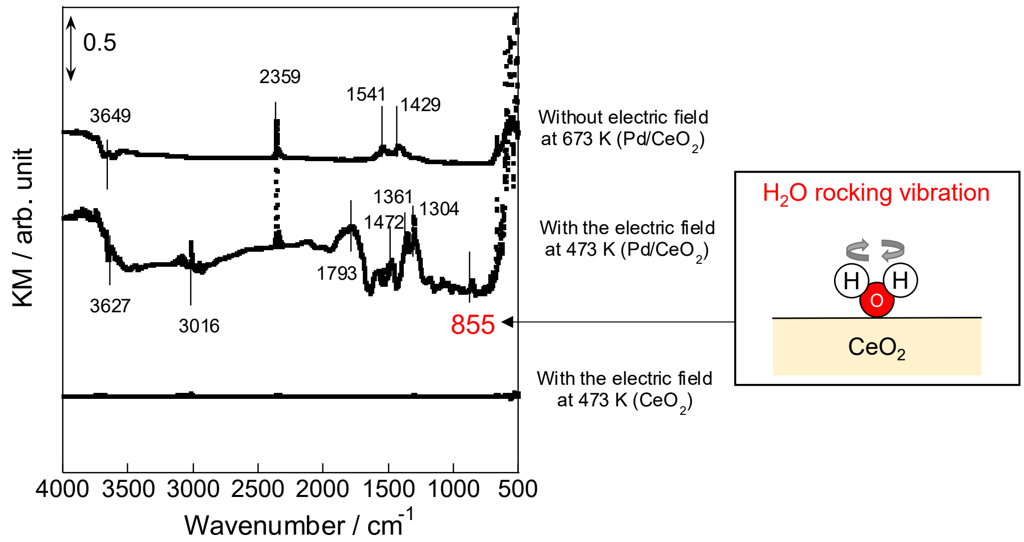

Figure 1.8. *Operando*-DRIFTS measurement with and without the electric field. (Catalyst, 1.0wt%Pd/CeO_2 or CeO_2; Flow, CH_4 : H_2O : Ar = 1 : 2 : 62 SCCM; Current, 0 or 5 mA.)[63]

Correlation between metal particle sizes and TOFs (TOF-s and TOF-p) has been regarded as elucidating the reaction sites (Fig. 1.9). Hereinafter, TOF-s means the reaction rate normalized by the amount of the exposed metal atoms. TOF-p represents the rate normalized by the amount of metal atoms at the nanoparticle perimeter. Commonly, CH_4 reacts over metal surfaces during steam reforming. [67] Therefore, TOF-s shows almost constant values irrespective of particle sizes without the electric field (Fig. 1.9 (a)). In contrast, TOF-p represents constant values with application of the electric field (Fig. 1.9 (b)). This specific trend elucidated that the reaction of the rate-determining step proceeded at the Pd particle perimeter.

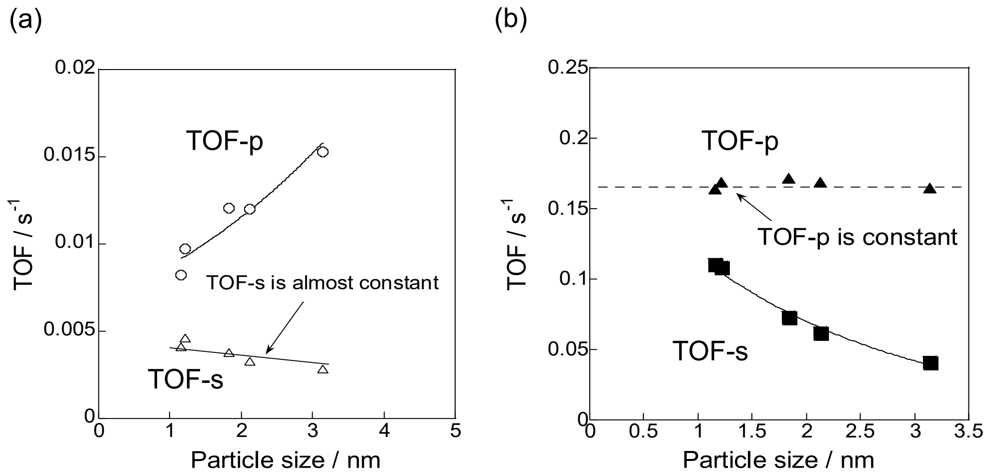

Figure 1.9. Correlation between TOFs and Pd particle sizes (a) with the electric field at 473 K and (b) without the electric field at 673 K. (Catalyst, 1.0wt%Pd/CeO_2 ; Flow, CH_4 : H_2O : Ar = 1 : 2 : 62 SCCM; Current, 0 or 5 mA.)[63]

For further consideration, isotope effects on CH_4 steam reforming in the electric field were investigated using D_2O and CD_4.[58] Conventionally, a primary kinetic isotope effect is observed in this reaction. It shows that the rate-determining step is the cleavage of C–H bond in CH_4. [68] In contrast, an inverse kinetic isotope effect was confirmed in the electric field. This novel trend can be explained with the novel reaction mechanism through C–H–H transition state. The H^+ supplied from supports collide with CH_4 over metal particles and assisted cleavage of C–H bonds in the electric field. Three atom (C–H–H) states have a stronger bond than C–H at the initial state. [69–71] This is expected to be the reason why the activation energy decreased with heavier deuterium, as shown in Fig. 1.10. In this manner, the reaction mechanism involving surface protonics in the electric field has been elucidated.

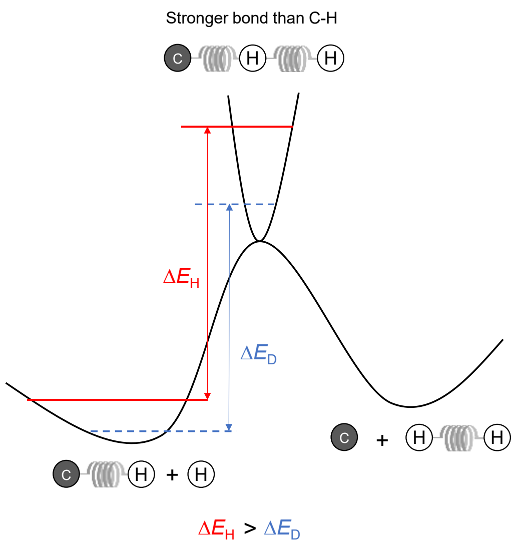

Figure 1.10. Schematic image of inverse kinetic isotope effects on C-H dissociation *via* C-H-H. [61]

1.3.2. NH_3 synthesis

Similar facilitation of the reaction by surface protonics was revealed for NH_3 synthesis, even without the supply of H_2O. [54-56, 72]

Commonly, NH_3 synthesis proceeds through a "dissociative mechanism", by which N_2 directly dissociates. [51]

$$N_2(g) \rightarrow 2N_{ad} \quad (1.1)$$
$$H_2(g) \rightarrow 2H_{ad} \quad (1.2)$$
$$N_{ad} + 3H_{ad} \rightarrow NH_3(g) \quad (1.3)$$

In contrast, we assumed that NH_3 synthesis in the electric field should proceed *via* the "associative mechanism", where N_2 reacts with H^+ over supports before dissociation. Such a mechanism has been reported for NH_3 synthesis using homogeneous catalysts. [73]

$$H_2(g) \rightarrow 2H_{ad} \quad (1.4)$$
$$H_{ad} \rightarrow H^+_{ad} + e^- \quad (1.5)$$
$$N_{2ad} + H^+_{ad} + e^- \rightarrow N_2H_{ad} \quad (1.6)$$
$$N_2H_{ad} + H^+_{ad} + e^- \rightarrow N_2H_{2\,ad} \quad (1.7)$$
$$N_2H_{2\,ad} + H^+_{ad} + e^- \rightarrow N_{ad} + NH_3 \quad (1.8)$$

In the equations above, "g" denotes a gaseous species; "ad" denotes adsorbed species. The N_2 and N_2H adsorb onto active metals, whereas H^+ adsorbs over lattice oxygen of supports (O_{lat}). This novel reaction through the "associative mechanism" was elucidated based on the governing factors of NH_3 synthesis rate in the electric field from the perspective of supports and active metals.

First, the role of supports in NH_3 synthesis in the electric field was investigated using DFT calculations and experiments. [72] $SrZrO_3$ (SZO) was chosen as the host metal oxide. The cations were partially replaced by heterocations (A-site (Sr), Ba, Ca; B-site (Zr), Al, Y). Ru was chosen as the supported metal. We placed a finite Ru rod on the SZO surface as a loading metal, as shown in Fig. 1.11(a). The Ru facets of the rod were set as (1011) and (0001) facets, which were observed using TEM. [55] Correlation between the N_2H formation energy at the Ru periphery and the NH_3 synthesis rate in the electric field was considered using the model supports described above and an active metal, as shown in Fig. 1.11(b). Consequently, the NH_3 synthesis rate was found to increase as N_2H formation became more favorable. The analysis of electron density and adsorption energy of the intermediates revealed that the NH_3 synthesis rate in the electric field depends on the electron-donating and proton-donating capacities of the support.

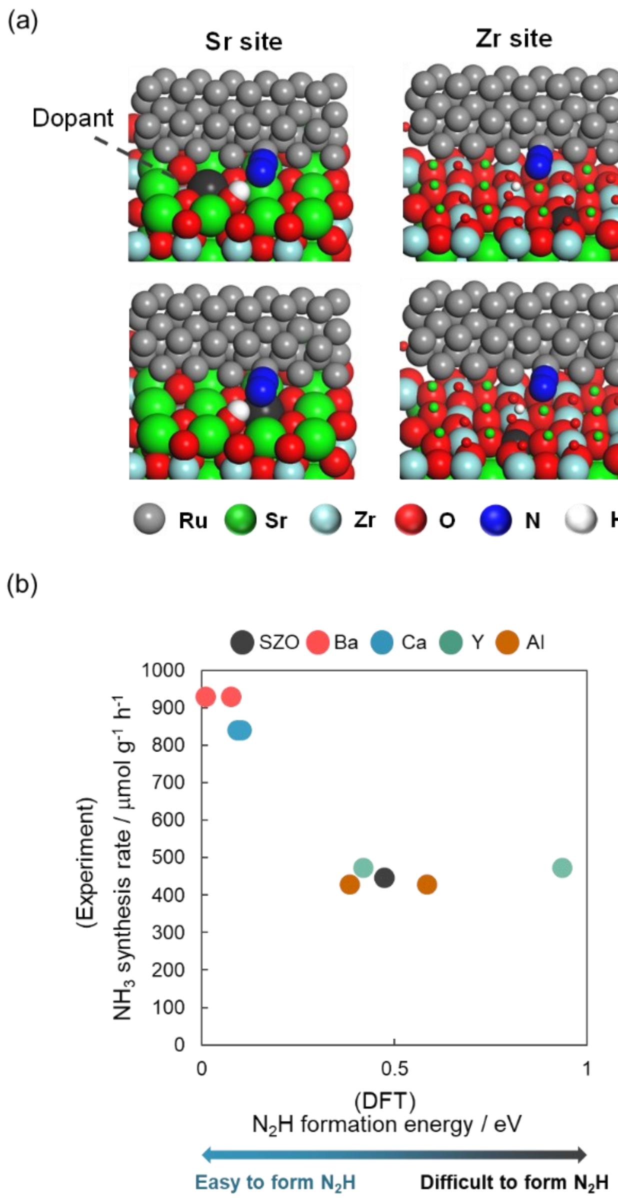

Figure 1. 11. (a) Ru-rod loaded SZO model with dopants used for DFT calculations, and (b) correlation between the DFT-calculated N_2H formation energy and NH_3 synthesis rate in the electric field. Copyright 2020 RSC publishing.

Second, we studied the effects of active metals on the NH_3 synthesis rate in the electric field using CeO_2 as a support.[56] Figure 1.12 shows DFT calculation models and correlation between the TOFs and DFT calculated energies of N_2 dissociation or N_2H formation. Regarding results achieved without the electric field (Fig. 1.12(a)), the volcano-shaped relation was confirmed, corresponding to conventional reports. [74] It is noteworthy that Fe and Ni exhibit higher performance than Ru in the electric field. Therefore, the relation between TOF-p in the electric field and *pseudo*-ΔE(N_2H formation) was regarded as presented in Fig. 1.12(b). Consequently, the linear relation was confirmed, indicating that NH_3 synthesis in the electric field proceeds *via* N_2H intermediate.

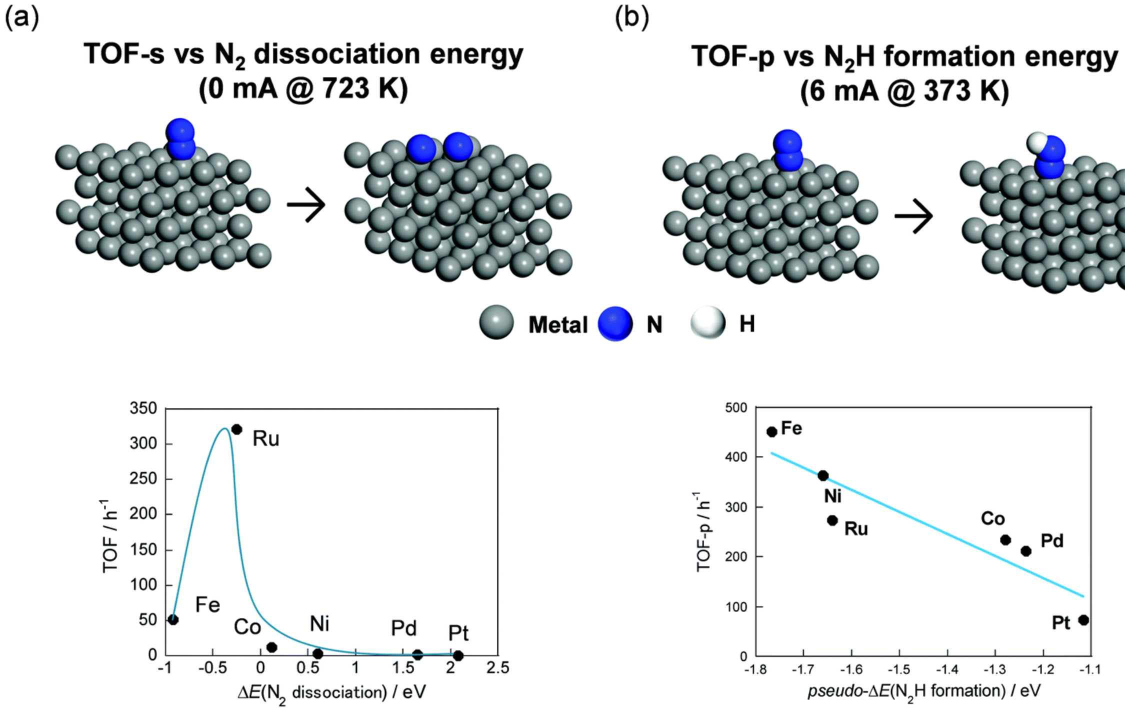

Figure 1. 12. Schematic images of DFT-calculated metal surface models and the correlation between (a) TOF-s without the electric and DFT-calculated N_2 dissociation energy, (b) TOF-p with the electric field, and DFT-calculated N_2H formation energy. Copyright 2020 RSC publishing.

1.3.3. Dehydrogenation of methylcyclohexane

Reports have also described that MCH dehydrogenation in an electric field is facilitated by surface proton conduction (Fig. 1.13). [75, 76]

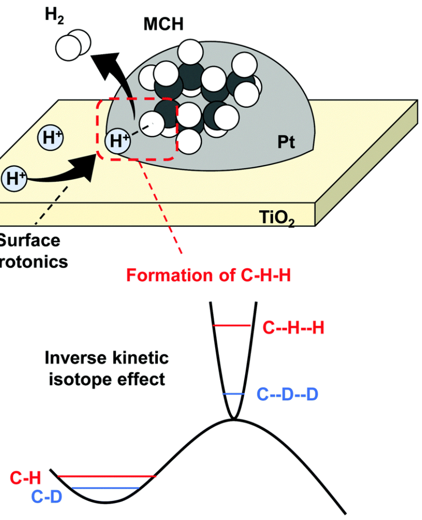

Figure 1.13. Schematic image of MCH dehydrogenation assisted by surface protonics in the electric field, and the energy diagram related to inverse kinetic isotope effect. Copyright 2020 RSC publishing.

The H_2 reaction order is usually negative, as for dehydrogenation. [77] However, the reaction order in the electric field was positive. Therefore, we inferred that MCH dehydrogenation is also activated by surface protonics. Actually, H^+ is expected to be supplied from H_2 derived from MCH. Similarly to CH_4 steam reforming, an inverse kinetic isotope effect was observed when MCH (C_7H_{14}) was replaced by MCH_D (C_7D_{14}).

1.4. Sophisticated techniques for detecting hydrogen migration

In this section, recent state-of-the-art works for the evaluation of hydrogen spillover and surface protonics are introduced.

1.4.1. *In-situ* FT-IR measurement

It has been revealed that metal nanoparticles (Au, Cu, Pt, Ru, Rh) supported by reducible metal oxides (*e.g.* ZnO [78, 79] and TiO_2 [18, 19, 21]) show broad-band IR background absorbance around 1000–4000 cm^{-1} after H_2 supply. Those signals were assigned to the electronic characters of metal oxides instead of vibrations of atoms. Panayotov *et al*. explained this electronic character using the reaction of H_2 with Rh-loaded or Au-loaded TiO_2 as examples. [19, 21] First, gaseous H_2 dissociates over loading metals. Subsequently, H atoms spill over onto the support (TiO_2 in this case). At that time, H atoms turn to H^+ and donate an electron to the shallow trap (ST) state, signifying n-doping by hydrogen spillover on semiconductor supports. Some doped electrons are excited thermally or by IR radiation. Fermi level difference between TiO_2 and H atoms induces such n-doping. In this manner, hydrogen spillover can be detected sensitively using IR spectroscopic method. Additionally, they reported that an in-depth understanding of the hydrogen spillover procedure is obtainable by simultaneous detection of broad-band IR background absorbance and adsorbed CO (carbonyl species), as shown in Fig. 1.14. [21]

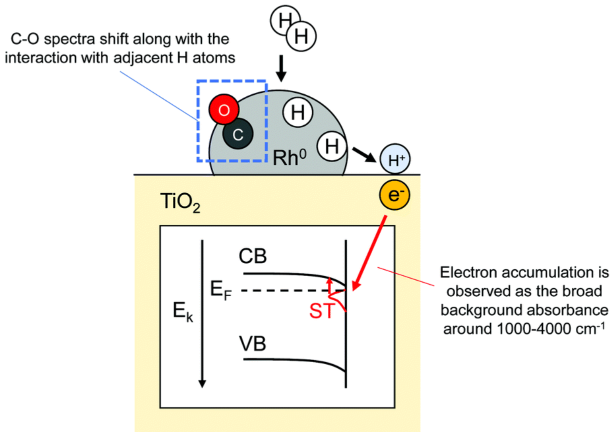

Figure 1.14. Schematic image of *in-situ* FT-IR measurement for detecting hydrogen spillover from Rh^0 to TiO_2 with CO probe. Copyright 2020 RSC publishing.

First, they prepared Rh/TiO_2 partially covered with CO. Then, H_2 was supplied there. As a result, the peaks assigned to carbonyl species shifted in accordance with dissociative adsorption of H atoms over Rh^0 surface. Therefore, it was revealed that CO can function as a probe for co-adsorbed H atoms. [30] They also evaluated the time dependence of the n-doping amount in TiO_2. The time-resolved data showed kinetic branches of two types. One is rapid electron accumulation during the initial 10 min of H_2 exposure. The other is a slow accumulation thereafter. At the first stage, H atoms can quickly spill over onto TiO_2, followed by an immediate electron accumulation. As the hydrogen spillover proceeds, the conduction band (CB) of TiO_2 at the edge of Rh^0 bends down and gets closer to the Fermi level, signifying the decrease in the difference of Fermi level between TiO_2 and H atoms. This bending hinders n-doping further. In summary, Panayotov *et al*. revealed that FT-IR measurements provide detailed mechanistic insight into hydrogen spillover.

1.4.2. X-ray adsorption spectromicroscopy with clearly separated iron oxide and Pt pairs

Karim *et al*. compared irreducible and reducible metal oxides using well-fabricated samples formed and confirmed using electron beam lithography [80] and STM measurement. [17] They prepared pairs of Pt nanoparticle and iron oxide over TiO_2 (reducible) and Al_2O_3 (irreducible) support. Distances between Pt particles and iron oxides were controlled precisely. Then they used *in-situ* X-ray absorption spectromicroscopy (XAS) to observe the reduction of iron oxides by H atoms migrated from Pt particles. [80] This examination clearly provided information about the length of hydrogen migration over each support, as shown in Fig. 1.15. In terms of Al_2O_3, 15 nm was the limitation of hydrogen migration. They confirmed the adsorption of H atoms over Al_2O_3 by detecting three-coordinated surface Al adsorption sites. [81, 82] Therefore, H atoms can migrate over Al_2O_3, although the migration length was limited. Regarding TiO_2, all iron oxides were reduced, indicating total difference from irreducible oxides. Their investigation quantitatively illustrated the difference of H atoms migration over irreducible oxides and reducible oxides.

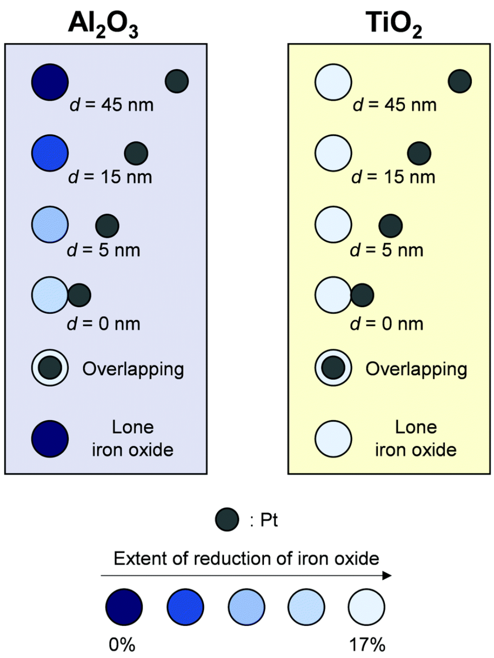

Figure 1.15. Schematic image of spillover on Al_2O_3 (irreducible) and TiO_2 (reducible) traced using Pt-iron oxide pairs. Copyright 2020 RSC publishing.

1.4.3. Surface-enhanced Raman spectroscopy using Au/TiO_2/Pt sandwich sample

Wei *et al*. examined hydrogen spillover and catalysis involving migration using well-arranged Au/TiO_2/Pt sandwich nanostructures and surface-enhanced Raman spectroscopy (SERS). [22] Actually, SERS is a sensitive analysis of vibration derived from adsorbed molecules over rough metal surfaces, which is enabled by Raman signals enhanced by a strong electromagnetic field. [83–85] Therefore, this method is a strong tool for *in-situ* tracking of catalytic reactions. [86, 87] The well-designed sample (Au/TiO_2/Pt) has spatially divided active sites, as shown in Fig. 1.16: Pt is a hydrogen activation site; TiO_2 is a hydrogen migration site; and Au is a hydrogenation site. They used large Au particles. Therefore, H_2 dissociation over Au is negligible. [88] They used the Langmuir–Blodgett (LB) method to prepare a single layer of TiO_2 nanoparticles (10 nm). The TiO_2 layer height was adjusted by changing the number of deposition layers over Pt film. At the final step, a monolayer of Au particles (55 nm) with a probe of hydrogenation (para-nitrothiophenol, pNTP) was loaded. Using this sample, hydrogenation of pNTP was performed. The reaction was traced using SERS. First, efficient conversion of pNTP was confirmed over Au/10 nm-TiO_2/Pt, meaning that H atoms can be supplied from Pt to Au *via* the TiO_2 surface. Increasing the TiO_2 layer thickness increased the activation energy of hydrogenation. The reaction proceeded only slightly with a 50 nm TiO_2 layer. Furthermore, the selectivity was affected by the TiO_2 thickness. They suggested that the change of H atom coverage over Au along with TiO_2 thickness caused different selectivity. They revealed clearly that the *in-situ* SERS with well-designed samples can quantitatively evaluate the role of hydrogen spillover in reactivity and selectivity of hydrogenation.

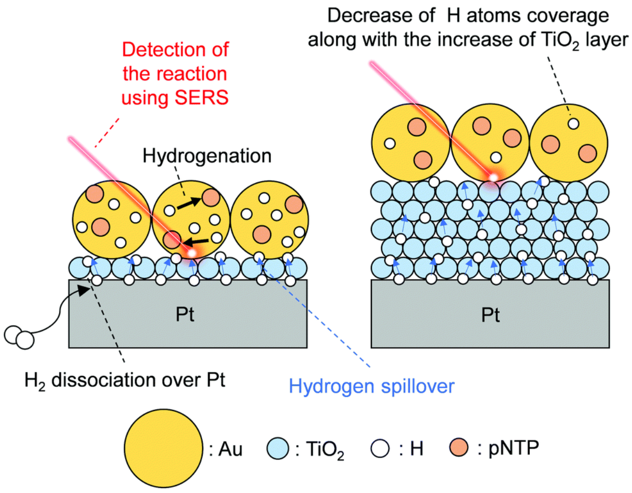

Figure 1.16. Schematic image of catalytic reaction related to hydrogen spillover detected over Au/TiO_2/Pt sandwich sample using SERS. Copyright 2020 RSC publishing.

1.4.4. Encapsulated sample and DFT calculation

As described in section 1.1, hydrogen spillover on irreducible oxides such as SiO_2, Al_2O_3, and zeolites has persisted as a controversial issue. [13] Recently, direct evidence for the hydrogen spillover on surfaces of zeolites was obtained using encapsulated samples. [23, 24] Experimental works for encapsulated samples were well-summarized by Choi *et al*. [89] Furthermore, the concept of the sample design is the same as that in an earlier study described in part 1.2.2. Therefore, only DFT calculations for the hydrogen spillover mechanism are introduced herein. Im *et al*. and Shin *et al*. reported that defect generation and annihilation occur during long-range hydrogen spillover on aluminosilicate. [23, 25] Sufficient Brønsted acid sites are necessary for this migration. Figure 1.17 presents a schematic image of the hydrogen spillover mechanism. Al at the left end in Fig. 1.15 describes the external aluminosilicate surface, which has three covalent bonds. Without defect, one H atom at Brønsted acid sites moves to the adjacent site (Fig. 1.17 (a)). The activation energy was calculated as 0.98 eV. Placing the Pd_6 cluster lowered the activation energy of this initial step to 0.52 eV, suggesting the important role of the supported metal particles. $[AlO_4H_2]^+$ and $[AlO_4]^-$ were produced simultaneously after the first migration. The formation of these defect pairs led to the subsequent migration at both sites (Fig. 1.17 (b)). Actually, $[AlO_4]^-$ accepts a H radical (H·), thereby forming $[AlO_4]^-$ H·. The obtained $[AlO_4]^-$ H· has a three-centered bond (O–H–O) and can be regarded as a local distortion of the original Brønsted acid sites ($[AlO_4]^-$ H^+) induced by the spatially localized unpaired electron (*i.e.* polaron). This electron at $[AlO_4]^-$ easily diffuses into the neighboring Brønsted acid sites. Thereby, another O–H–O bond is formed (*i.e.* polaron conduction) as shown in Fig. 1.17(c). After long-range migration, H^+ recombines with the electron at the external support surface. The H^+ can hydrogenate the adsorbed species if there is a molecule such as benzene (Fig. 1.17 (d)).

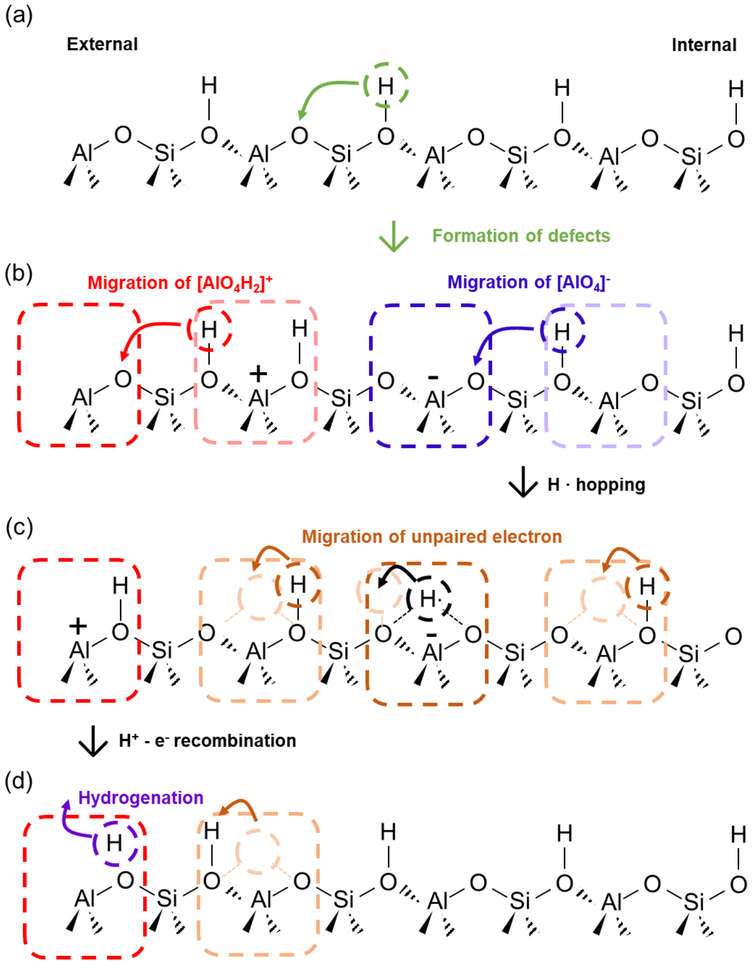

Figure 1.17. Schematic images of long-range H atoms migration mechanism over aluminosilicate. (a) Formation of $[AlO_4H_2]^+$ and $[AlO_4]^-$. (b) H atoms migration at $[AlO_4H_2]^+$ and $[AlO_4]^-$. (c) Migration of unpaired electron. (d) Hydrogenation using supplied H^+ at the external aluminosilicate surface. Copyright 2020 RSC publishing.

1.4.5. Electrochemical impedance spectroscopy using porous pellets

Recently, surface protonics mediated by adsorbed H_2O onto metal oxides (*e.g.* Y-stabilized ZrO_2 [10, 11] and CeO_2 [63]) has been evaluated successfully using porous pellets. They used metal oxide pellets with low relative density (approx. 70%, [10] 60%, [63] 50% [11]). Under a H_2O atmosphere, adsorbed H_2O layers are formed onto the pores of samples with low density. Then, the H^+ transportation *via* those adsorbed species can be detected using electrochemical impedance spectroscopy (EIS). A schematic image is shown in Fig. 1.18.

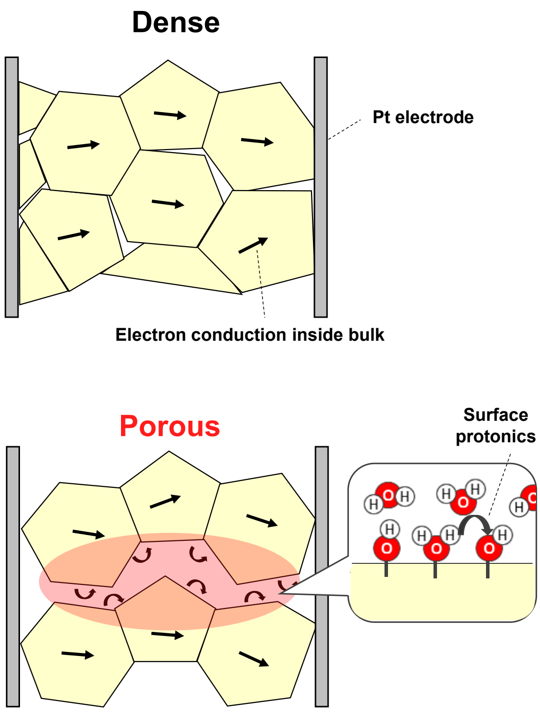

Figure 1.18. Schematic images of EIS measurements using dense and porous samples under H_2O atmosphere. Copyright 2020 RSC publishing.

Because of conduction mediated by adsorbed species, the surface conductivity under adequate relative humidity exhibited peculiar temperature dependence. Conductivity increased along with the decrement in temperature. The H_2O layer thickness increased under the lower temperature region, leading to surface conductivity enhancement. The H^+ transport mechanism under H_2O atmosphere has been revealed by combining EIS measurements with porous pellets and *ab initio* molecular dynamics simulation. [90] The mechanism changed along with the H_2O layer thickness. H^+ is transported *via* the Grotthuss mechanism when the H_2O layer is thin (*i.e.* ice-like water). In contrast, the mechanism shifted to the vehicle mechanism with a thick layer of H_2O (*i.e.* liquid-like water). In this mechanism, H^+ does not move to adjacent oxygen, but moves as H_3O^+.

As explained in parts 1.3.2 and 1.3.3, we have demonstrated that surface protonics under H_2 atmosphere without the supply of H_2O (dry condition) is also crucially important for the catalysis in the electric field. Therefore, the development of observation techniques for surface protonics under H_2 atmosphere is necessary. Consequently, using porous (R.D. = 60%) and dense (R.D. = 90%) pellets, EIS measurements were performed under N_2 or $N_2 + H_2$ atmosphere. [91] Figure 1.19 shows the temperature dependence of electrochemical conductivity over each sample and in each atmosphere. Results show that the pellets of two types exhibited completely different responses to the change of atmospheres. Regarding the porous sample, the apparent activation energy of the electrochemical conductivity decreased drastically as the atmosphere shifted from N_2 to $N_2 + H_2$. However, with a dense sample, no marked change was observed even with supply of H_2. This difference might derive from the adsorption of H^+ species over exposed surfaces of the porous pellet. This H^+ is expected to be formed by the dissociative adsorption of H_2. Furthermore, D_2

isotope effects were regarded as elucidating the main conductive carrier under H_2 atmosphere, and the conduction mechanism. Consequently, the porous sample exhibited a primary isotope effect at all measured temperatures, indicating H^+ conduction *via* the Grotthuss mechanism. This primary isotope effect is explainable by a semi-classical theory. [92–97] The difference of zero-point energies between O–H^+ and O–D^+ is greater than that at a transition state. The weakening of the O–H^+ (D^+) is attributable to the difference described above. No isotope effect is expected to be detected because there is no dissociation of O-H^+ (D^+) bond if the conduction proceeds *via* a vehicle mechanism. Therefore, the D_2 isotope effects on the conductivity revealed the surface protonics *via* the Grotthuss mechanism on a porous pellet under a H_2 atmosphere.

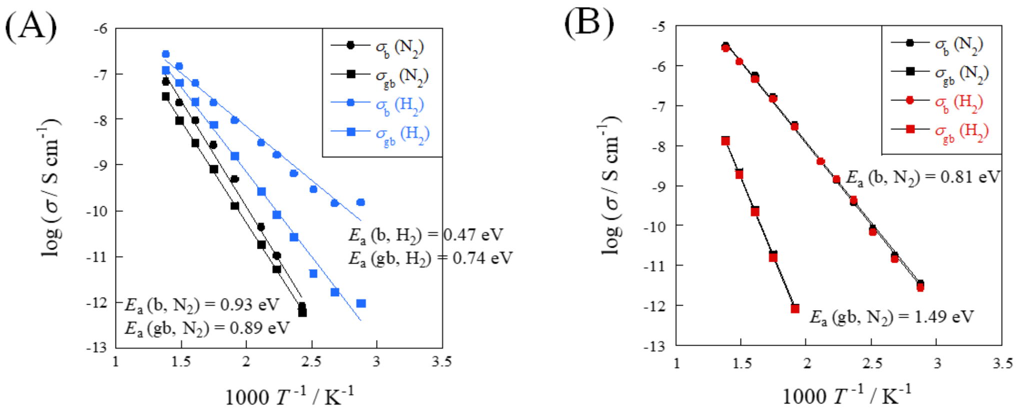

Figure 1.19. Temperature dependences of electrochemical conductivity (σ) under N_2 and N_2+H_2 atmosphere: (A) porous pellet of $SrZrO_3$ (R.D. = 60%), and (B dense pellet of $SrZrO_3$ (R.D. = 90%). Copyright 2020 RSC publishing.

1.5. Aims of the thesis

As introduced through this chapter, hydroxy (OH) groups over metal oxides surface play a crucially important role in catalysis. Therefore, we can facilitate the development of catalysis by obtaining in-depth knowledge of the interaction between OH and metal oxide surfaces. In this context, the aims of the thesis are the following.

1. To obtain knowledge for controlling factors of interaction between OH and metal oxides
2. To elucidate the role of OH stability in catalytic reactions

Chapters 2 and 3 show the controlling factors of H_2O and H_2 adsorption over CeO_2-based materials. DFT calculations revealed that electron-deficient O_{lat} and lattice flexibility play an important role in strong adsorption. Furthermore, the DFT-obtained results were confirmed experimentally using XRD, Raman, *in-situ* DRIFTS, and XPS. Chapter 4 explained the role of OH stability in catalysis. NH_3 synthesis in the electric field is affected strongly by OH coverage.

Moreover, heterocation doping controlled the stability of the OH group and altered the temperature dependence. Finally, the catalytic science for OH groups is summarized in chapter 5.

References

1. L. Kuai, Z. Chen, S. Liu, E. Kan, N. Yu, Y. Ren, C. Fang, X. Li, Y. Li, and B. Geng, Titania supported synergistic palladium single atoms and nanoparticles for room temperature ketone and aldehydes hydrogenation, *Nat. Commun.*, 2020, **11**, 48.
2. S. Campisi, C. E. Chan-Thaw, L. E. Chinhilla, A. Chutia, G. A. Botton, K. M. H. Mohammed, N. Dimitratos, P. P. Wells, and A. Villa, Dual-Site-Mediated Hydrogenation Catalysis on Pd/NiO: Selective Biomass Transformation and Maintenance of Catalytic Activity at Low Pd Loading, *ACS Catal.*, 2020, **10**, 5483 – 5492.
3. X. Xue, J. Liu, D. Rao, S. Xu, W. Bing, B. Wang, S. He, and M. Wei, Double-active site synergistic catalysis in Ru–TiO_2 toward benzene hydrogenation to cyclohexene with largely enhanced selectivity, *Catal. Sci. Technol.*, 2017, **7**, 650 – 657.
4. Y. Guo, S. Mei, K. Yuan, D. -J. Wang, H. -C. Liu, C. -H. Yan, and Y. W. Zhang, Low-Temperature CO_2 Methanation over CeO_2-Supported Ru Single Atoms, Nanoclusters, and Nanoparticles Competitively Tuned by Strong Metal–Support Interactions and H-Spillover Effect, *ACS Catal.*, 2018, **8**, 6203 – 6215.
5. T. Franken, J. Terreni, A. Borgschulte, and A. Heel, Solid solutions in reductive environment – A case study on improved CO_2 hydrogenation to methane on cobalt based catalysts derived from ternary mixed metal oxides by modified reducibility, *J. Catal.*, 2020, **382**, 385 – 394.
6. S. K. Beaumont, S. Alayoglu, C. Specht, N. Kruse, and G. A. Somorjai, A Nanoscale Demonstration of Hydrogen Atom Spillover and Surface Diffusion Across Silica Using the Kinetics of CO_2 Methanation Catalyzed on Spatially Separate Pt and Co Nanoparticles, *Nano. Lett.*, 2014, **14(8)**, 4792 – 4796.
7. S. Wu, Y. -K. Peng, T. -Y. Chen, J. Mo, A. Large, I. McPherson, H. -L. Chou, I. Willkinson, F. Venturini, D. Grinter, P. F. Escorihuela, G. Held, and S. C. E. Tsang, Removal of Hydrogen Poisoning by Electrostatically Polar MgO Support for Low-Pressure NH_3 Synthesis at a High Rate over the Ru Catalyst, *ACS Catal.*, 2020, **10**, 5614 – 5622.
8. A. Lueking and R. T. Yang, Hydrogen Spillover from a Metal Oxide Catalyst onto Carbon Nanotubes—Implications for Hydrogen Storage, *J. Catal.*, 2002, **206**, 165–168.
9. F. H. Yang and R. T. Yang, Ab initio molecular orbital study of adsorption of atomic hydrogen on graphite:: Insight into hydrogen storage in carbon nanotubes, *Carbon*, 2002, **40(3)**, 437–444.
10. S. Miyoshi, Y. Akao, N. Kuwata, J. Kawamura, Y. Oyama, T. Yagi, and S. Yamaguchi, Low-Temperature Protonic Conduction Based on Surface Protonics: An Example of Nanostructured Yttria-Doped Zirconia, *Chem. Matter.*, 2014, **26(18)**, 5194 – 5200.
11. S. Ø. Stub, E. Vøllestad, and T. Norby, Mechanisms of Protonic Surface Transport in Porous Oxides: Example of YSZ, *J. Phys. Chem. C*, 2017, **121**, 12817 – 12825.
12. W. C. Conner and J. L. Falconer, Spillover in Heterogeneous Catalysis, *Chem. Rev.*, 1995, **95**, 759 – 788.
13. R. Prins, Hydrogen Spillover. Facts and Fiction, *Chem. Rev.*, 2012, **112**, 2714 – 2738.

14. S. Khoobiar, Particle to Particle Migration of Hydrogen Atoms on Platinum-Alumina Catalysts from Particle to Neighboring Particles, *J. Phys. Chem.*, 1964, **68**, 411 – 412.
15. L. Chen, A. C. Cooper, G. P. Pez, and H. Cheng, On the Mechanisms of Hydrogen Spillover in MoO_3, *J. Phys. Chem. C*, 2008, **112(6)**, 1755 – 1758.
16. X. Sha, L. Chem, A. C. Cooper, G. P. Pez, and H. Cheng, Hydrogen Absorption and Diffusion in Bulk α-MoO_3, *J. Phys. Chem. C*, 2009, **113(26)**, 11399 – 11407.
17. W. Karim, C. Spreafic, A. Kleibert, J. Gobrecht, J. VandeVondele, Y. Ekinci, and J. A. van Bokhoven, Catalyst support effects on hydrogen spillover, *Nature*, 2017, **541**, 68 – 71.
18. D. A. Panayotov, and J. T. Yates, Spectroscopic Detection of Hydrogen Atom Spillover from Au Nanoparticles Supported on TiO_2: Use of Conduction Band Electrons, *J. Phys. Chem. C*, 2007, **111(7)**, 2959 – 2964.
19. D. A. Panayotov, S. P. Burrows, J. T. Yates, and J. R. Morris, Mechanistic Studies of Hydrogen Dissociation and Spillover on Au/TiO_2: IR Spectroscopy of Coadsorbed CO and H-Donated Electrons, *J. Phys. Chem. C*, 2011, **115(45)**, 22400 – 22408.
20. D. Panayotov, M. Mihaylov, D. Nihitianova, T. Spassov, and K. Hadjiivanov, Spectral evidence for hydrogen-induced reversible segregation of CO adsorbed on titania-supported rhodium, *Phys. Chem. Chem. Phys.*, 2014, **16**, 13136 – 13144.
21. D. Panayotov, E. Ivanova, M. Mihaylov, K. Chakarova, T. Spassov, and K. Hadjiivanov, Hydrogen spillover on Rh/TiO_2: the FTIR study of donated electrons, co-adsorbed CO and H/D exchange, *Phys. Chem. Chem. Phys.*, 2015, **17**, 20563 – 20573.
22. J. Wei, S. -N. Qin, J. -L. Liu, X. -Y. Ruan, Z. Guan, H. Yan, D. -Y. Wei, H. Zhang, J. Cheng, H. Xu, Z. -Q. Tian, and J. -F. Li, In Situ Raman Monitoring and Manipulating of Interfacial Hydrogen Spillover by Precise Fabrication of Au/TiO_2/Pt Sandwich Structures, *Angew. Chem. Int. Ed.*, 2020, **59**, 1 – 6.
23. J. Im, H. Shin, H. Jang, H. Kim, and M. Choi, Maximizing the catalytic function of hydrogen spillover in platinum-encapsulated aluminosilicates with controlled nanostructures, *Nat. Commun.*, 2014, **5**, 3370.
24. S. Lee, K. Lee, J. Im, H. Kim, and M. Choi, Revisiting hydrogen spillover in Pt/LTA: Effects of physical diluents having different acid site distributions, *J. Catal.*, 2015, **325**, 26 – 34.
25. H. Shin, M. Choi and H. Kim, A mechanistic model for hydrogen activation, spillover, and its chemical reaction in a zeolite-encapsulated Pt catalyst, *Phys. Chem. Chem. Phys.*, 2016, **18**, 7035 – 7041.
26. S. Ogo, Y. Sekine, Catalytic reaction assisted by plasma or electric field, *Chem. Rec.*, 2017, **17(8)**, 726 – 738.
27. M. Torimoto, K. Murakami, Y. Sekine, Low-temperature heterogenous catalytic reaction by surface protonics, *Bull. Chem. Soc. Jpn.*, 2019, **92(10)**, 1785 – 1792.
28. Y. Sekine and R. Manabe, Reaction mechanism of low-temperature catalysis by surface protonics in an electric field, *Faraday Discuss.*, *in press*. DOI: 10.1039/C9FD00129H

29. K. Murakami and Y. Sekine, Recent Progress in use and observation of surface hydrogen migration over metal oxides, *Phys. Chem. Chem. Phys.*, 2020, **22**, 22852 – 22863.
30. X. F. Yang, A. Wang, B. Qiao, J. Li, J. Liu, and T. Zhang, Single-Atom Catalysts: A New Frontier in Heterogeneous Catalysis, *Acc. Chem. Res.*, 2013, **46(8)**, 1740 – 1748.
31. J. Liu, Catalysis by Supported Single Metal Atoms, *ACS Catal.*, 2017, **7(1)**, 34 – 59.
32. B. Qiao, A. Wang, X. Yang, L. F. Allard, Z. Jiang, Y. Cui, J. Liu, J. Li, and T. Zhang, Single-atom catalysis of CO oxidation using Pt_1/FeO_x, *Nat. Chem.*, 2011, **3**, 634 – 641.
33. M. Yang, S. Li, Y. Wang, J. A. Herron, Y. Xu, L. F. Allard, S. Lee, J. Huang, M. Marvrikakis, and M. F. Stephanopoulos, Catalytically active Au-O(OH)$_x$- species stabilized by alkali ions on zeolites and mesoporous oxides, *Science*, 2014, **346 (6216)**, 1498 – 1501.
34. C. Zhao, X. Dai, T. Yao, W. Chen, X. Wang, J. Wang, J. Yang, S. Wei, Y. Wui, and Y. Li, Ionic Exchange of Metal–Organic Frameworks to Access Single Nickel Sites for Efficient Electroreduction of CO_2, *J. Am. Chem. Soc.*, 2017, **139**, 8078 – 8081.
35. Y. Zhao, K. R. Yang, Z. Wang, X. Yan, S. Cao, Y. Ye, Q. Dong, X. Zhang, J. E. Thorne, L. Jin, K. L. Materna, A. Trimpalis, H. Bai, S. C. Fakra, X. Zhong, P. Wang, X. Pan, J. Guo, M. F. Stephanopoulos, G. Brudvig, V. S. Batista, and D. Wang, Stable iridium dinuclear heterogeneous catalysts supported on metal-oxide substrate for solar water oxidation, *Proc. Natal. Acad. Sci. USA*, 2018, **115**, 29028 – 2907.
36. H. Yan, H. Lv, H. Yi, W. Liu, Y. Xia, X. Huang, W. Huang, S. Wei, X. Wu, and J. Lu, Understanding the underlying mechanism of improved selectivity in Pd_1 single-atom catalyzed hydrogenation reaction, *J. Catal.*, 2018, **366**, 70 – 79.
37. R. Liu, Y. Yang, N. Sun, and L. Kuai, Mesoporous Cu-Ce-O_x Solid Solutions from Spray Pyrolysis for Superior Low-Temperature CO Oxidation, *Chem. Eur. J*, 2019, **25**, 15586 – 15593.
38. L. Kuai, S. Liu, S. Cao, Y. Ren, E. Kan, Y. Zhao, N. Yu, F. Li, X. Li, Z. Wu, X. Wang, and B. Geng, Atomically Dispersed Pt/Metal Oxide Mesoporous Catalysts from Synchronous Pyrolysis–Deposition Route for Water–Gas Shift Reaction, *Chem. Mater.*, 2018, **30 (16)**, 5534 – 5538.
39. Y. Nakagawa, M. Tamura, and K. Tomishige, Catalytic Reduction of Biomass-Derived Furanic Compounds with Hydrogen, *ACS Catal.*, 2013, **3(12)**, 2655 – 2668.
40. X. Meng, Y. Yang, L. Chen, M. Xu, X. Zhang, and M. Wei, A Control over Hydrogenation Selectivity of Furfural via Tuning Exposed Facet of Ni Catalysts, *ACS Catal.*, 2019, **9(5)**, 4226 – 4235.
41. G. Zhou, Y. Pei, Z. Jiang, K. Fan, M. Qiao, B. Sun, and B. Zong, Doping effects of B in ZrO_2 on structural and catalytic properties of Ru/B-ZrO_2 catalysts for benzene partial hydrogenation, *J. Catal.*, 2014, **311**, 393 – 403.
42. J. Liu, S. Xu, W. Bing, F. Wang, C. Li, M. Wei, G. Evans, and X. Duan, Cu-Decorated Ru Catalysts Supported on Layered Double Hydroxides for Selective Benzene Hydrogenation to Cyclohexene, *ChemCatChem*, 2015, **7(5)**, 846 – 855.

43. B. Miao, S. S. K. Ma, X. Wang, H. Su, and S. H. Chan, Catalysis mechanisms of CO_2 and CO methanation, *Catal. Sci. Technol.*, 2016, **6**, 4048 – 4058.
44. S. Kattel, P. Liu and J. G. Chen, Tuning Selectivity of CO_2 Hydrogenation Reactions at the Metal/Oxide Interface, *J. Am. Chem. Soc.*, 2017, **139**, 9739 – 9754.
45. A. Ozaki, K. Aika, and H. Hori, A New Catalyst System for Ammonia Synthesis, *Bull. Chem. Soc. Jpn.*, 1971, **44(11)**, 3216.
46. K. Aika, H. Hori, and A. Ozaki, Activation of nitrogen by alkali metal promoted transition metal I. Ammonia synthesis over ruthenium promoted by alkali metal, *J. Catal.*, 1972, **27(3)**, 424 – 431.
47. M. Kitano, Y. Inoue, Y. Yamazaki, F. Hayashi, S. Kanbara, S. Matsuishi, T. Yokoyama, S. W. Kim, M. Hara, and H. Hosono, Ammonia synthesis using a stable electride as an electron donor and reversible hydrogen store, *Nat. Chem.*, 2012, **4**, 934 – 940.
48. M. Kitano, Y. Inoue, M. Sasase, K. Kishida, Y. Kobayashi, K. Nishiyama, T. Tada, S. Kawamura, T. Yokoyama, M. Hara, and H. Hosono, Self-organized Ruthenium-Barium Core-Shell Nanoparticles on a Mesoporous Calcium Amide Matrix for Efficient Low-Temperature Ammonia Synthesis, *Angew. Chem. Int. Ed.*, 2018, **57**, 2648 – 2652.
49. M. Kitano, J. Kujirai, K. Ogasawara, S. Matsuishi, T. Tada, H. Abe, Y. Niwa, and H. Hosono, Low-Temperature Synthesis of Perovskite Oxynitride-Hydrides as Ammonia Synthesis Catalysts, *J. Am. Chem. Soc.*, 2019, **141(51)**, 20344 – 20353.
50. Y. Ogura, K. Sato, S. Miyahara, Y. Kawano, T. Toriyama, T. Yamamoto, S. Matsumura, S. Hosokawa, and K. Nagaoka, Efficient ammonia synthesis over a $Ru/La_{0.5}Ce_{0.5}O_{1.75}$ catalyst pre-reduced at high temperature, *Chem. Sci.*, 2018, **9**, 2230 – 2237.
51. K. Honkala, A. Hellman, I. N. Remediakis, A. Logadottir, A. Carlsson, S. Dahl, C. H. Christensen, and J. K. Nørskov, Ammonia synthesis from first-principles calculations, *Science*, 2005, **307**, 555 – 558.
52. K. Aika, Role of alkali promoter in ammonia synthesis over ruthenium catalysts-Effect on reaction mechanism, *Catal. Today*, 2017, **286**, 14 – 20.
53. H. Bielawa, O. Hinrichsen, A. Birkner, and M. Muhler, The Ammonia-Synthesis Catalyst of the Next Generation: Barium-Promoted Oxide-Supported Ruthenium, *Angew. Chem., Int. Ed.*, 2001, **40**, 1061 – 1063.
54. K. Murakami, R. Manabe, H. Nakatsubo, T. Yabe, S. Ogo, Y. Sekine, Elucidation of the role of electric field on low temperature ammonia synthesis using isotopes, *Catal. Today*, 2018, **303**, 271 – 275.
55. R. Manabe, H. Nakatsubo, A. Gondo, K. Murakami, S. Ogo, H. Tsuneki, M. Ikeda, A. Ishikawa, H. Nakai, and Y. Sekine, Electrocatalytic synthesis of ammonia by surface proton hopping, *Chem. Sci.*, 2017, **8**, 5434 – 5439.
56. K. Murakami, Y. Tanaka, R. Sakai, K. Toko, K. Ito, A. Ishikawa, T. Higo, T. Yabe, S. Ogo, M. Ikeda, H. Tsuneki, H. Nakai, Y. Sekine, The important role of N_2H formation energy for low-temperature ammonia synthesis in an electric field, *Catal. Today*, 2020, **351**, 119 – 124.

57. R. Manabe, S. Okada, R. Inagaki, K. Oshima, S. Ogo, and Y. Sekine, Surface protonics promotes catalysis, *Sci. Rep.*, 2016, **6**, 38007.
58. S. Okada, R. Manabe, R. Inagaki, S. Ogo, and Y. Sekine, Methane dissociative adsorption in catalytic steam reforming of methane over Pd/CeO_2 in an electric field, *Catal. Today*, 2018, **307**, 272 – 276.
59. M. Torimoto, S. Ogo, D. Harjowinoto, T. Higo, J. G. Seo, S. Furukawa and Y. Sekine, Enhanced methane activation on diluted metal–metal ensembles under an electric field: breakthrough in alloy catalysis, *Chem. Commun.*, 2019, **55**, 6693 – 6695.
60. A. Takahashi, R. Inagaki, M. Torimoto, Y. Hisai, T. Matsuda, Q. Ma, J. G. Seo, T. Higo, H. Tsuneki, S. Ogo, T. Norby and Y. Sekine, Effects of metal cation doping in CeO_2 support on catalytic methane steam reforming at low temperature in an electric field, *RSC Adv.*, 2020, **10**, 14487 – 14492.
61. M. Torimoto, S. Ogo, Y. Hisai, N. Nakano, A. Takahashi, Q. Ma, J. G. Seo, H. Tsuneki, T. Norby and Y. Sekine, Support effects on catalysis of low temperature methane steam reforming, *RSC Adv.*, 2020, **10**, 26418 – 26424.
62. R. Inagaki, R. Manabe, Y. Hisai, Y. Kamite, T. Yabe, S. Ogo, Y. Sekine, Steam reforming of dimethyl ether promoted by surface protonics in an electric field, *Int. J. Hydrog. Energy*, 2018, **43(31)**, 14310 – 14318.
63. K. Takise, A. Sato, K. Muraguchi, S. Ogo, and Y. Sekine, Steam reforming of aromatic hydrocarbon at low temperature in electric field, *Appl. Catal. A*, 2019, **573**, 56 – 63.
64. S. Sakurai, S. Ogo, and Y. Sekine, Hydrogen production by steam reforming of ethanol over Pt/CeO_2 catalyst in electric field at low temperature, *J. Jpn. Petrol. Inst.*, 2016, **59(5)**, 174 – 183.
65. D. F. Torre, K. Kośmider, J. Carrasco, M. V. G. Pirovano, and R. Pérez, Insight into the Adsorption of Water on the Clean CeO_2(111) Surface with van der Waals and Hybrid Density Functionals, *J. Phys. Chem.*, 2012, **116**, 13584 – 13593.
66. R. Manabe, S. Stub, T. Norby, Y. Sekine, Evaluating surface protonic transport on cerium oxide via electrochemical impedance spectroscopy measurement, *Solid State Commun.*, 2018, **270**, 45 – 49.
67. J. Wei and E. Iglesia, Mechanism and Site Requirements for Activation and Chemical Conversion of Methane on Supported Pt Clusters and Turnover Rate Comparisons among Noble Metals, *J. Phys. Chem. B*, 2004, **108(13)**, 4094 – 4103.
68. A. Yamaguchi and E. Iglesia, Catalytic activation and reforming of methane on supported palladium clusters, *J. Catal.*, 2010, **274**, 52 – 63.
69. K. B. Wiberg, The Deuterium Isotope Effect, *Chem. Rev.*, 1955, **55(4)**, 713 – 743.
70. B. Kerkeni and D. C. Clary, Quantum reactive scattering of H + hydrocarbon reactions, *Phys. Chem. Chem. Phys.*, 2006, **8**, 917 – 925.
71. M. J. Kurylo, G. A. Hollinden and R. B. Timmons, Classical trajectory studies of the reaction CH_4+H→CH_3+H_2, *J. Chem. Phys.*, 1970, **52**, 1773.

72. K. Murakami, Y. Tanaka, S. Hayashi, R. Sakai, Y. Hisai, Y. Mizutani, A. Ishikawa, H. Nakai, Y. Sekine, Governing factors of supports of ammonia synthesis in an electric field found using density functional theory, *J. Chem. Phys.*, 2019, **151**, 064708.
73. D. V. Yandulov and R. R. Schrock, Catalytic reduction of dinitrogen to ammonia at a single molybdenum center, *Science*, 2003, **301**, 76 – 78.
74. S. Dahl, A. Logadottir, C. J. H. Jacobsen, and J. K. Nørskov, Electronic factors in catalysis: the volcano curve and the effect of promotion in catalytic ammonia synthesis, *Appl. Catal., A*, 2001, **222**, 19 – 29.
75. K. Takise, A. Sato, K. Murakami, S. Ogo, J. G. Seo, K. Imagawa, S. Kado, and Y. Sekine, Low-temperature selective catalytic dehydrogenation of methylcyclohexane by surface protonics, *RSC Adv.*, 2019, **9**, 5918-5924.
76. M. Kosaka, T. Higo, S. Ogo, J. G. Seo, K. Imagawa, S. Kado, and Y. Sekine, Low-temperature selective dehydrogenation of methylcyclohexane by surface protonics over Pt/anatase-TiO_2 catalyst, *Int. J. Hydrog. Energy*, 2020, **45(1)**, 738 – 743.
77. F. Alhumaidan, D. Cresswell, and A. Garforth, Hydrogen Storage in Liquid Organic Hydride: Producing Hydrogen Catalytically from Methylcyclohexane, *Energy Fuels*, 2011, **25**, 4217 – 4234.
78. F. Boccuzzi, A. Chiorino, G. Ghiotti and E. Guglielminotti, Metal/n-zinc oxide interaction: effect of the surrounding atmosphere on IR transparency, *Langmuir*, 1989, **5(1)**, 66 – 70.
79. E. Guglielminotti, F. Boccuzzi, G. Ghiotti and A. Chiorino, Infrared evidence of metal-semiconductor interaction in a Ru/ZnO system, *Surf. Sci.*, 1987, **189-190**, 331 – 338.
80. W. Karim, A. Kleibert, U. Hartfelder, A. Balan, J. Gobrecht, J. A. van Bokhoven and Y. Ekinci, Size-dependent redox behavior of iron observed by *in-situ* single nanoparticle spectro-microscopy on well-defined model systems, *Sci. Rep.*, 2016, **6**, 18818.
81. J. A. van Bokhoven, A. M. J. van der Eerden and D. C. Koningsberger, Three-Coordinate Aluminum in Zeolites Observed with In situ X-ray Absorption Near-Edge Spectroscopy at the Al K-Edge: Flexibility of Aluminum Coordinations in Zeolites, *J. Am. Chem. Soc.*, 2003, **125**, 7435 – 7442.
82. R. Wischert, P. Laurent, C. Copéret, F. Delbecq and P. Sautet, γ-Alumina: The Essential and Unexpected Role of Water for the Structure, Stability, and Reactivity of "Defect" Sites, *J. Am. Chem. Soc.*, 2012, **134**, 14430 – 14449.
83. K. Kneipp, Y. Wang, H. Kneipp, L. T. Perelman, I. Itzkan, R. R. Dasari and M. S. Feld, Single Molecule Detection Using Surface-Enhanced Raman Scattering (SERS), *Phys. Rev. Lett.*, 1997, **78**, 1667 – 1670.
84. S. Nie and R. Emory, Probing Single Molecules and Single Nanoparticles by Surface-Enhanced Raman Scattering, *Science*, 1997, **275**, 1102 – 1106.
85. J. F. Li, Y. F. Huang, Y. Ding, Z. L. Yang, S. B. Li, X. S. Zhou, F. R. Fun, W. Zhang, Z. Y. Zhou, D. Y. Wu, B. Ren, Z. L. Wang and Z. Q. Tian, Shell-isolated nanoparticle-enhanced Raman spectroscopy, *Nature*, 2010, **464**, 392 – 395.

86. V. Joseph, C. Engelbrekt, J. Zhang, U. Gernert, J. Ulstrup and J. Kneipp, Characterizing the Kinetics of Nanoparticle-Catalyzed Reactions by Surface-Enhanced Raman Scattering, *Angew. Chem. Int. Ed.*, 2012, **51**, 7592 – 7596.
87. W. Xie and S. Schlüker, Surface-enhanced Raman spectroscopic detection of molecular chemo- and plasmo-catalysis on noble metal nanoparticles, C*hem. Commun.*, 2018, **54**, 2326 – 2336.
88. E. Bus, J. T. Miller and J. A. van Bokhoven, Hydrogen Chemisorption on Al_2O_3-Supported Gold Catalysts, *J. Phys. Chem. B*, **109(30)**, 14581 – 14587.
89. M. Choi, S. Yook and H. Kim, Hydrogen Spillover in Encapsulated Metal Catalysts: New Opportunities for Designing Advanced Hydroprocessing Catalysts, *ChemCatChem*, 2015, **7**, 1048 – 1057.
90. R. Sato, S. Ohkuma, Y. Shibuta, F. Shimojo, and S. Yamaguchi, Proton Migration on Hydrated Surface of Cubic ZrO2: Ab initio Molecular Dynamics Simulation, *J. Phys. Chem. C*, 2015, **119**, 28925 – 28933.
91. Y. Hisai, K. Murakami, Y. Kamite, Q. Ma, E. Vøllestad, R. Manabe, T. Matsuda, S. Ogo, T. Norby, Y. Sekine, First observation of surface protonics on $SrZrO_3$ perovskite under H_2 atmosphere, *Chem. Commun.*, 2020, **56**, 2699-2702.
92. A.S. Nowick and A.V. Vaysley, Isotope effect and proton hopping in high-temperature protonic conductors, *Solid State Ionics*, 1997, **97**, 17 – 26.
93. R. Mukundan, E.L. Brosha, S.A. Birdsell, A.L. Costello, F.H. Garzon, and R.S. Williams, Tritium Conductivity and Isotope Effect in Proton-Conducting Perovskites, *J. Electrochem. Soc.*, 1999, **146**, 2184 – 2187.
94. T. Scherban, A.S. Nowick, Bulk protonic conduction in Yb-doped $SrCeO_3$, *Solid State Ionics*, 1989, **35**, 189 – 194.
95. T. Scherban, W-K Lee, and A.S. Nowick, Bulk protonic conduction in Yb-doped $SrCeO_3$ and $BaCeO_3$, *Solid State Ionics*, 1988, **28–30**, 585 – 588.
96. W.-K. Lee, A.S. Nowick, and L.A. Boatner, Protonic conduction in acceptor-doped $KTaO_3$ crystals, *Solid State Ionics*, 1986, **18–19**, 989 – 993.
97. T. Scherban, and A.S. Nowick, Protonic conduction in Fe-doped $KTaO_3$ crystals, *Solid State Ionics*, 1992, **53–56**, 1004 – 1008.

Chapter 2 H_2O–CeO_2 Interaction Control by Heterocation Doping

The content in this chapter is partly reproduced from K. Murakami, S. Ogo, A. Ishikawa, Y. Takeno, T. Higo, H. Tsuneki, H. Nakai, and Y. Sekine, Heteroatom doping effects on interaction of H_2O and CeO_2 (111) surfaces studied using density functional theory: Key roles of ionic radius and dispersion, *J. Chem. Phys.*, 2020, **152**, 014707. Copyright AIP Publishing.

2.1. Introduction

Cerium oxide (ceria, CeO_2) has been used for various catalytic reactions including exhaust gas purification, [1, 2] steam reforming, [3, 4] water–gas shift reaction, [5–7] and NH_3 synthesis. [8, 9] Additionally, surface H^+ conduction *via* H_2O adsorbed onto CeO_2 surfaces has attracted much attention for novel low-temperature catalytic reactions, as described in chapter 1. [10, 11] These studies require knowledge of H_2O–CeO_2 interaction. Therefore, many researchers have investigated H_2O adsorption over CeO_2 at an atomic scale. [12–17]

Heterocation doping is widely known to be effective for tuning the CeO_2 performance. Particularly, the influences of heterocation doping on oxygen storage capacity (OSC) and oxygen ion conductivity have been studied extensively. Reportedly, high performance can be achieved by adding Zr, Ti, Sn, alkali earth metals, transition metals, and lanthanides. [18–27] Modification of CeO_2 by heterocation doping also plays an important role in reactions and conduction *via* adsorbed H_2O. [28] Therefore, some demand exists to elucidate heterocation-doping effects on the interaction between H_2O and CeO_2-based materials.

In this context, we specifically examined heterocation-doping effects on H_2O interaction onto CeO_2-based compounds in this chapter. DFT calculations revealed that the ionic radius of heterocations plays a key role in controlling the interaction between H_2O and CeO_2-based materials. Furthermore, *in-situ* DRIFTS measurements elucidated the heterocation-doping effects on the vibrational frequency of OH over CeO_2-based materials.

2.2. Experimental

2.2.1. Computational details

We performed all calculations using the Vienna *ab initio* simulation package (VASP 5.4.4.) [29–32] Configurations of valence electrons used for all calculations are presented in Table A.2.1. Projector-augmented wave (PAW) method including Perdew–Burke–Ernzerhof (PBE) was used for the expression of core–valence effects. [33] Electron Kohn–Sham orbital sets with kinetic energy lower than 400 eV were used. For all calculations, spin polarization was considered. Regarding *k*-space, 0.04 $Å^{-1}$ in Monkhorst–Pack reciprocal space was adopted for bulk structures; also, (1 × 1

× 1) mesh was adopted for all surface models. [34] Gaussian smearing was used for all considerations. The van der Waals force was considered using the DFT-D3 method described by Grimme. [35] Regarding on-site Coulomb repulsion of Ce 4*f* orbitals, DFT + *U* method was used. The *U* value was set as 5.0 eV. [14, 36–42] The H_2O molecular adsorption energy was calculated as −0.51 eV under these calculation conditions. This obtained value coincided with previously reported energies (*e.g.* −0.58 eV, [12] −0.52 eV,[13] −0.66 to −0.65 eV,[14] −0.49 eV,[15] and −0.45 to −0.76 eV [16]). This agreement suggests that the chosen *U* value was appropriate to describe the H_2O–CeO_2 interaction. The most stable H_2O adsorption structure in this calculation is portrayed in Fig. 2.1. Geometry optimization was performed using two adsorption forms reported as the most stable conformation. One has a single hydrogen bond between the H_2O and the lattice oxygen (O_{lat}). The other has two hydrogen bonds. Our calculations showed that the former is more stable.

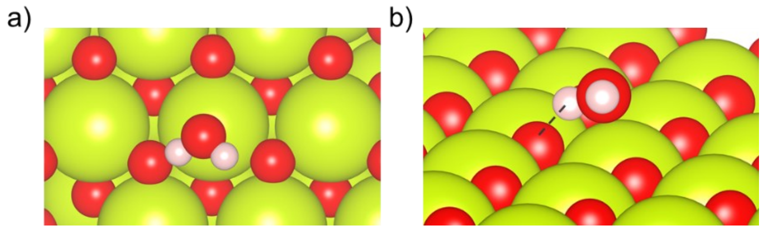

Figure 2.1. DFT-optimized structure of H_2O adsorbed over CeO_2 (111).: (a) top view, and (b) bird's eye view. A broken line represents the hydrogen bond. Yellow ball means Ce, red stands for O, and pink denotes H. Copyright 2020 AIP Publishing.

The CeO_2 (111) surface was expressed as a repeated (4 × 4) supercell with O–Ce–O tri-layers separated by a 20 Å vacuum gap in the *z*-direction, as shown in Fig. 2.2. Lattice constants were obtained from the DFT optimized bulk structures. Dopants were added by replacing two Ce at the uppermost surface. The bottom O–Ce–O layer was fixed. Other atoms were relaxed during geometry optimizations.

Molecules (H_2, O_2, and H_2O) were placed in a 10 × 10 × 10 Å cubic box. BCC-Fe bulk structures were calculated at the Γ point.

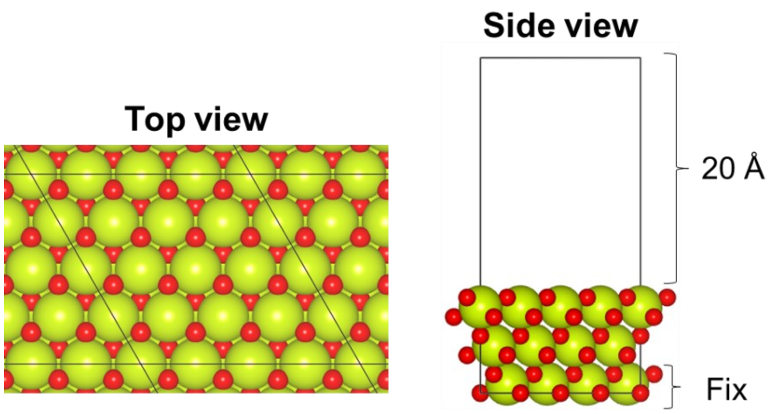

Figure 2.2. DFT-optimized structure of CeO_2 (111).: (a) top view, and (b) side view. Yellow ball means Ce, and red stands for O. Copyright 2020 AIP Publishing.

2.2.2. Sample preparation

$Ce_{1-x}M_xO_{2-\delta}$ (M: Zr, Al, Y, and Sr, x: 0, 0.1, 0.2 and 0.3) were synthesized using a complex polymerization method. First, citric acid monohydrate and ethylene glycol were dissolved with stoichiometric precursors listed in Table A.2.2. The solution was stirred at 343 K overnight. After evaporation of solvents, the obtained powder was calcined at 773 K for 5 h. Then they were sieved into particles of 355–500 μm for *in-situ* DRIFTS measurements.

2.2.3. Characterization

The crystalline structures of CeO_2-based compounds were evaluated by XRD measurements using X-ray diffraction (XRD, MiniFlex600; Rigaku Corp.) with Cu-Kα radiation sources.

Raman spectroscopy (NRS-4500; Jasco Corp.) was performed under ambient conditions with no pre-treatment. Raman signals were recorded in green laser (532 nm) excitation. The Raman shift has accuracy of 4 cm^{-1}.

2.2.4. *In-situ* DRIFTS measurement

In-situ DRIFTS measurements (FT-IR 6200; Jasco Corp.) obtained using a ZnSe window and a MCT detector were taken to evaluate adsorbed hydroxy (OH) groups over CeO_2-based compounds. The measurement scheme is shown in Fig. A.2.1. First, the sample was pre-treated at 473 K with Ar (60 SCCM) for 1 h. Later, background data were measured. Finally, the IR signals were collected under Ar (59.7 SCCM) and H_2O (0.3 SCCM) at 473 K.

2.3. Results and discussion

2.3.1. Construction of heterocation-doped CeO_2 (111)

This part describes examination of the most stable structure of pristine and heterocation-doped CeO_2 (111) surfaces using DFT calculations. First, the heterocation arrangements were optimized. The options for heterocation distribution are shown in Fig. A.2.2. We present the most stable structures obtained for all heterocations in Fig. 2.3. As might be readily apparent, the heterocation-doped CeO_2 surface became most stable when two heterocations adjoin each other for Ca, Al, Ga, Sc, Y, and Ti systems. In contrast, two heterocations have a separated configuration for Sr, Ba, La, and Zr doping. This trend suggests that heterocations with smaller ionic radii and lower valences are arranged preferentially side by side to alleviate the lattice strain. For several heterocations (Ba, Ga, Sc), the heterocation arrangements were investigated with oxygen vacancies (O_{vac}).

Consequently, a similar trend was confirmed (Table A.2.3). It is particularly interesting that Al doping induced the formation of the peroxide ion (O_2^{2-}) between two Al. The peroxide ion formation was also reported for La doping over a CeO_2 (100) or (110) surface. [43] One can reasonably infer that the formation of peroxide is feasible over unstable surfaces.

The Ce ion in CeO_2 exists as a quadrivalent cation when there is no O_{vac} or dopant. Consequently, the charge compensation by replacing lattice O^{2-} from the surface with divalent and trivalent heterocations must be considered. The calculated O_{vac} formation energies ($E(O_{vac})$) are presented in Table 2.1. $E(O_{vac})$ was defined as shown below.

$$E(\mathrm{O_{vac}}) = \frac{\{E(\text{slab with } n\ \mathrm{O_{vac}}) - E(\text{slab without } \mathrm{O_{vac}}) - n/2\ E(\text{molecular } \mathrm{O_2})\}}{n} \tag{2.1}$$

E(slab with n O_{vac}) and E(slab without O_{vac}) denote the energy of the surface with and without O_{vac}. The "n" presents the amount of O_{vac}. E(molecular O_2) shows the energy of gaseous O_2. In this consideration, we performed calculations for all possible sites of O_{vac} on the surface and sub-surface. In addition, the most stable configuration obtained was used for subsequent calculations. All $E(O_{vac})$ for the charge compensation showed negative values except for Al, meaning that O_{vac} should be formed with lower valent heterocations without oxidants such as O_2 or H_2O. Regarding Al, the formation of peroxide ion compensated the charge difference.

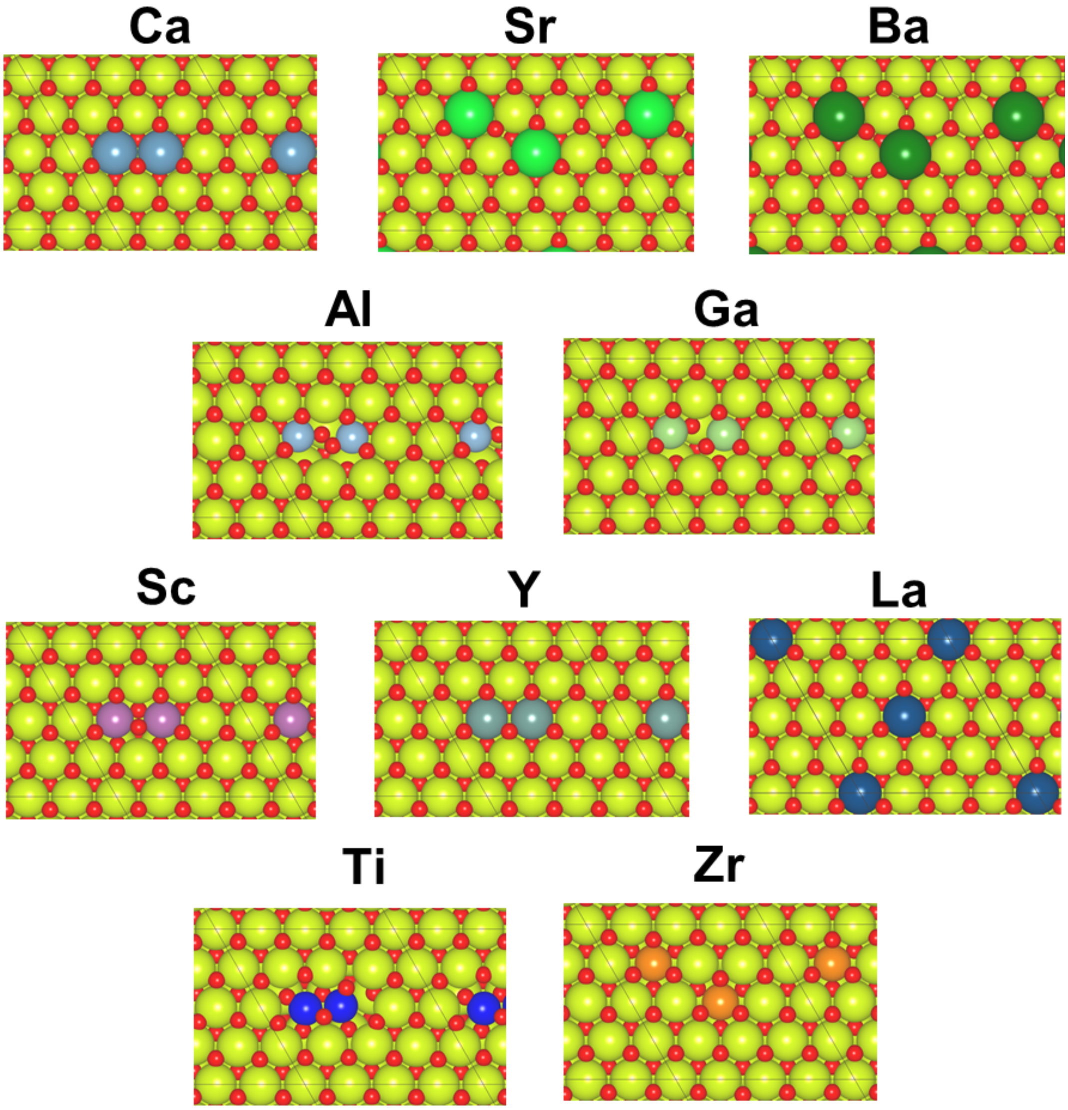

Figure 2.3. DFT-optimized structures of $Ce_xM_{1-x}O_{2-\delta}$ (111). Yellow ball means Ce, red stands for O, and other colors show heterocations. Copyright 2020 AIP Publishing.

Table 2.1. Oxygen vacancy (O_{vac}) formation energy ($E(O_{vac})$) over $Ce_{1-x}M_xO_{2-\delta}$ (111). Copyright 2020 AIP Publishing.

Dopant	Amount of O_{vac} (n)	$E(O_{vac})$ (eV)
Without dopant	1	2.98
Ca	1	−0.80
	2	−1.41
	3	0.83
Sr	1	−0.66
	2	−1.23
	3	1.25
Ba	1	−0.71
	2	−0.61
	3	2.49
Al	1	0.59
Ga	1	−0.63
	2	0.08
Sc	1	−0.95
	2	0.76
Y	1	−0.72
	2	2.36
La	1	−0.67
	2	2.59
Ti	1	0.42
Zr	1	1.92

Reportedly, O_{vac} is backfilled easily by H_2O under H_2O atmosphere. [44–46] Therefore, we calculated the dissociative adsorption energy of H_2O with and without backfilling of O_{vac} (E(H_2O adsorption with backfilling) and E(H_2O adsorption without backfilling)). The energies were expressed as presented below.

$$E(\text{H}_2\text{O adsorption with/without backfilling}) = E(\text{slab with/without backfilling}) - E(\text{slab with the charge compensating O}_{vac}) - E(\text{molecular H}_2) \quad (2.2)$$

E(slab with the charge compensating O_{vac}) denotes the energy of the slab with O_{vac} for the charge compensation. E(slab with backfilling) represents the energy of the slab with backfilled O_{vac}. E(molecular H_2O) shows the energy of gaseous H_2O. The calculated ΔE(with/without backfilling) is presented in Table 2.2. As a result, backfilling was found to be more feasible. The surfaces obtained with hydroxy are shown in Fig. 2.4.

Table 2.2. Comparison between H_2O dissociative adsorption energies with and without backfilling of O_{vac}. Copyright 2020 AIP Publishing.

Dopant	*E*(backfilling) (eV)	*E*(without backfilling) (eV)
Ca	−1.94	−0.42
Sr	−2.00	−0.43
Ba	−1.86	−0.44
Ga	−1.95	−0.79
Sc	−1.33	−0.58
Y	−1.95	−0.53
La	−1.82	−0.44

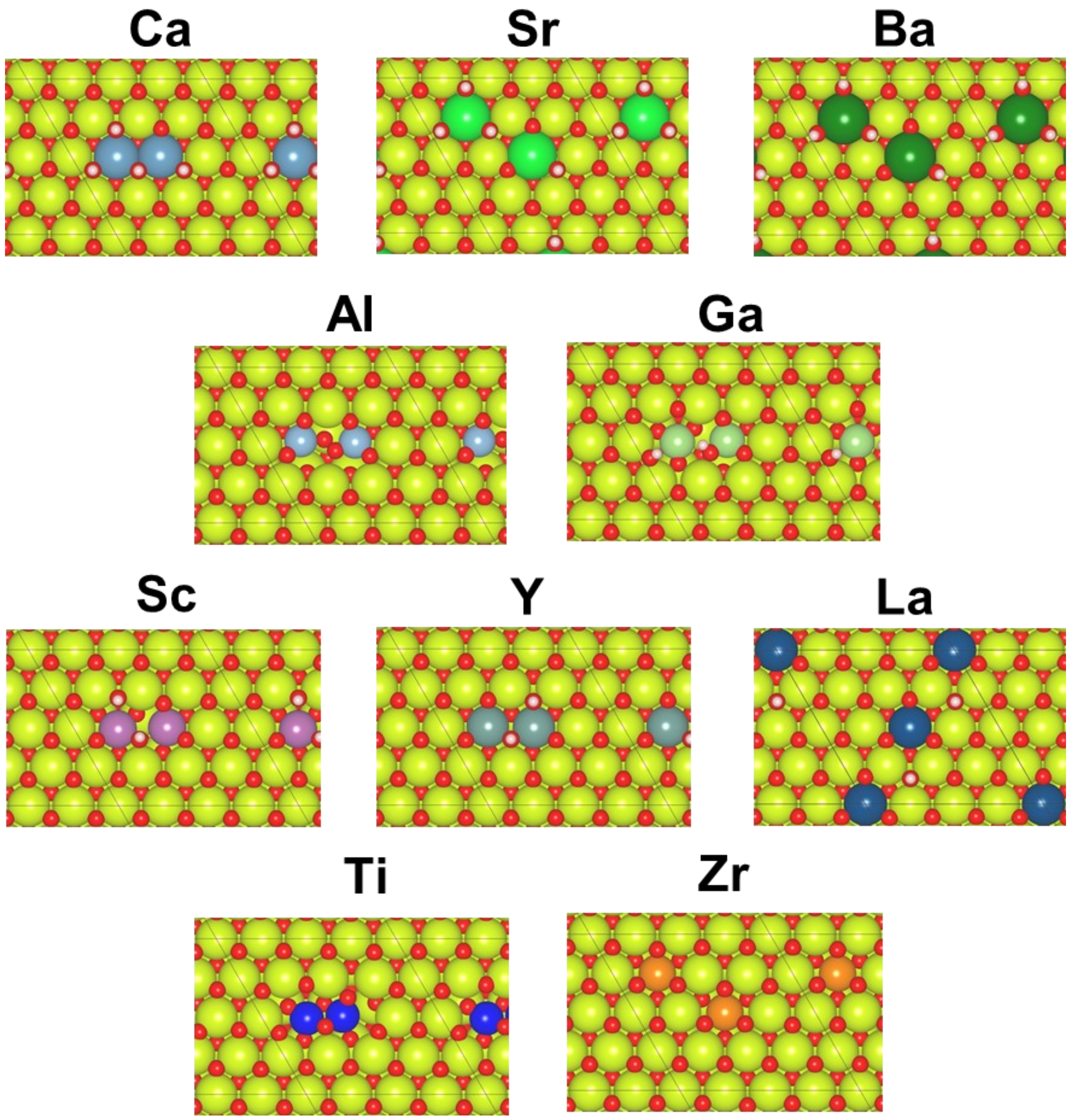

Figure 2.4. DFT-optimized structures of $Ce_xM_{1-x}O_{2-\delta}$ (111) taking into account the backfilling of O_{vac} by H_2O. Yellow ball means Ce, red stands for O, and other colors show heterocations. Copyright 2020 AIP Publishing.

2.3.2. Experimental confirmation of DFT-calculated surfaces

Differences in the dispersion of each heterocation were examined experimentally. First, we took XRD measurements for $Ce_{1-x}M_xO_{2-\delta}$ (M: Zr, Al, Y, and Sr, x: 0, 0.1, 0.2 and 0.3). The obtained signals are presented in Figs. A.2.3 – A.2.7. The obtained spectra were nearly identical among almost all samples, although slight peak shifts were observed. Only spectra of $Ce_{0.7}Sr_{0.3}O_{2-\delta}$ showed the existence of impurities ($SrCO_3$). Furthermore, mean atomic volumes were calculated using the obtained peaks assigned to (111) of $Ce_{1-x}M_xO_{2-\delta}$. Figure 2.5 presents the correlation between the dopant amount (x) and mean atomic volumes. Results show linear correlation, indicating that heterocations were doped successfully into the CeO_2 matrix (*i.e.* Zen's law [47]). It is noteworthy that Zr-doped CeO_2 exhibited a smaller mean atomic volume than that of Al-doped CeO_2. This result suggests that doped Al would form smaller clusters, as suggested from the DFT-optimized surface (Figs. 2.3 and 2.4).

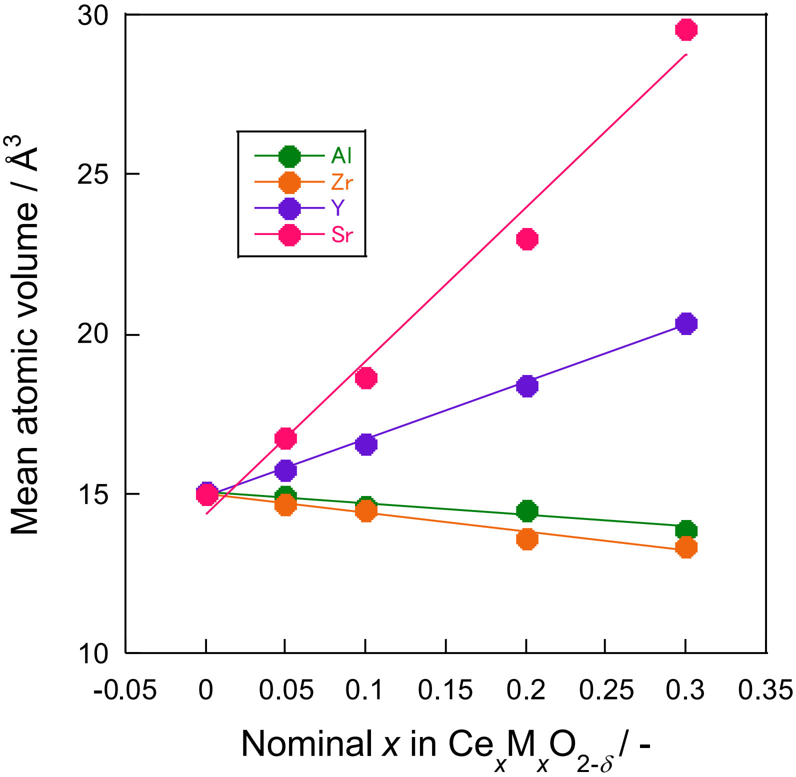

Figure 2.5. Correlation between dopants amount (x) in $Ce_xM_xO_{2-\delta}$ and mean atomic volume. The legends present dopants (M).

Second, we performed Raman spectroscopy using CeO_2 and $Ce_{0.9}Al_{0.1}O_{2-\delta}$ (Fig. 2.6). The peaks at 458 cm^{-1} were assignable to the F_{2g} symmetric Ce–O–Ce stretching vibration. [48, 49] The band at 827 cm^{-1} was detected only when Al was doped into CeO_2. This band can be assigned to μ-η1: η1 peroxide. [48–50] The frequency of peroxide over DFT-calculated Al-doped surface was also calculated as 833 cm^{-1}, supporting the assignment of 827 cm^{-1} band to peroxide. Moreover, the peroxide ion was observed only when the Al was set side by side, indicating validity of the DFT-obtained stable arrangements of heterocations.

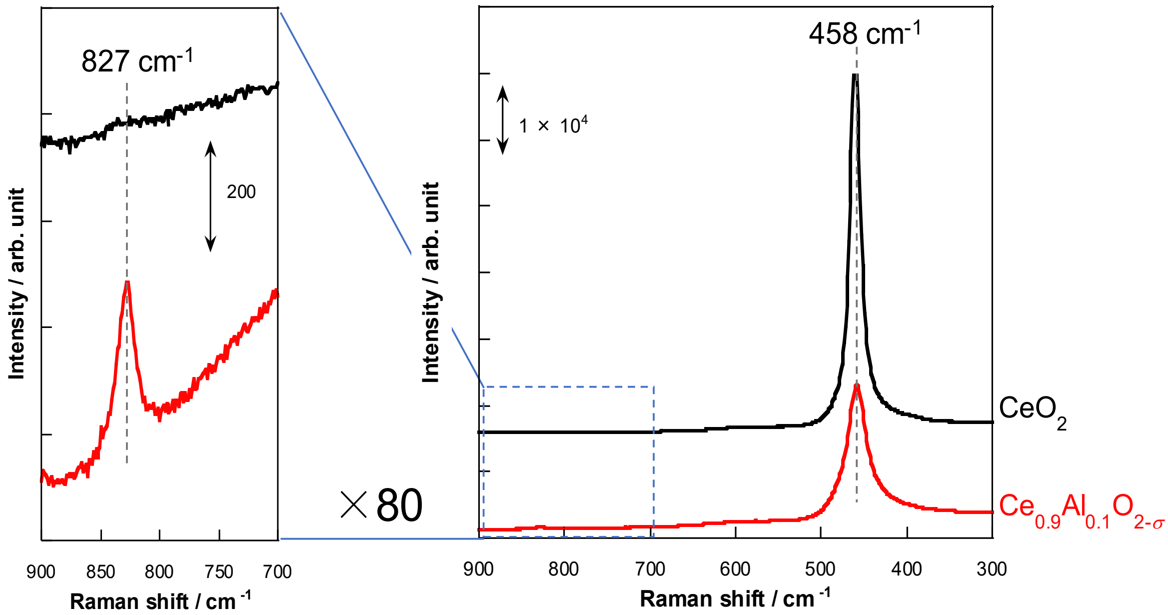

Figure 2.6. Raman spectra of CeO_2 and $Ce_{0.9}Al_{0.1}O_{2-\delta}$. Copyright 2020 AIP Publishing.

2.3.3. Heterocation-doping effects on H_2O–CeO_2 interaction (111)

The DFT-obtained surface models were confirmed as explained earlier. We analyzed the interaction between H_2O and CeO_2-based composite surfaces using the models presented in Fig. 2.4. First, heterocation-doping effects on the molecular adsorption of H_2O were evaluated. Figure 2.7 describes changes of H_2O molecular adsorption energy (ΔE(H_2O ad)) concomitantly with heterocation doping. The ΔE(H_2O ad) was calculated as shown below.

$$E(\mathrm{H_2O\ ad}) = E(\text{slab with H}_2\text{O}) - E(\text{slab without H}_2\text{O}) - E(\text{molecular H}_2\text{O}) \qquad (2.3)$$

E(slab with H_2O) and E(slab without H_2O) present the energy of CeO_2-based surfaces with and without H_2O adsorption. In Fig. 2.7, only outermost cations are depicted. The names of the heterocations are presented inside the circles. The other circles without notation stand for Ce cations. The surface cations are colored based on the difference of H_2O adsorption energy (ΔE(H_2O ad)). The energy over pristine CeO_2 was used as a reference value. Red sites present stronger H_2O adsorption. The blue sites mean the opposite (weak adsorption of H_2O). Red sites tend to be observed around smaller heterocation-doped surfaces. Furthermore, brown balls show sites at which H_2O voluntarily dissociates during the geometry optimization, meaning the H_2O would dissociate without a reaction barrier. Such spontaneous dissociation of H_2O was detected around Ce sites next to Al and onto heterocations with small ionic radii (Ga, Sc, Zr, and Ti). Over black ball sites, H_2O desorbed. Such sites were observed on Sr-, Ga-, and Al-doped surfaces. Regarding Sr, repulsion by a surface OH group formed by backfilling of O_{vac} with H_2O led to H_2O desorption.

Regarding Ga and Al, the heterocations sank into the CeO_2 matrix because of the small ionic radius; H_2O was unable to reach the sites. Summarizing the trend revealed from Fig. 2.7, one can infer that doping by heterocations with small ionic radius facilitates the H_2O molecular adsorption.

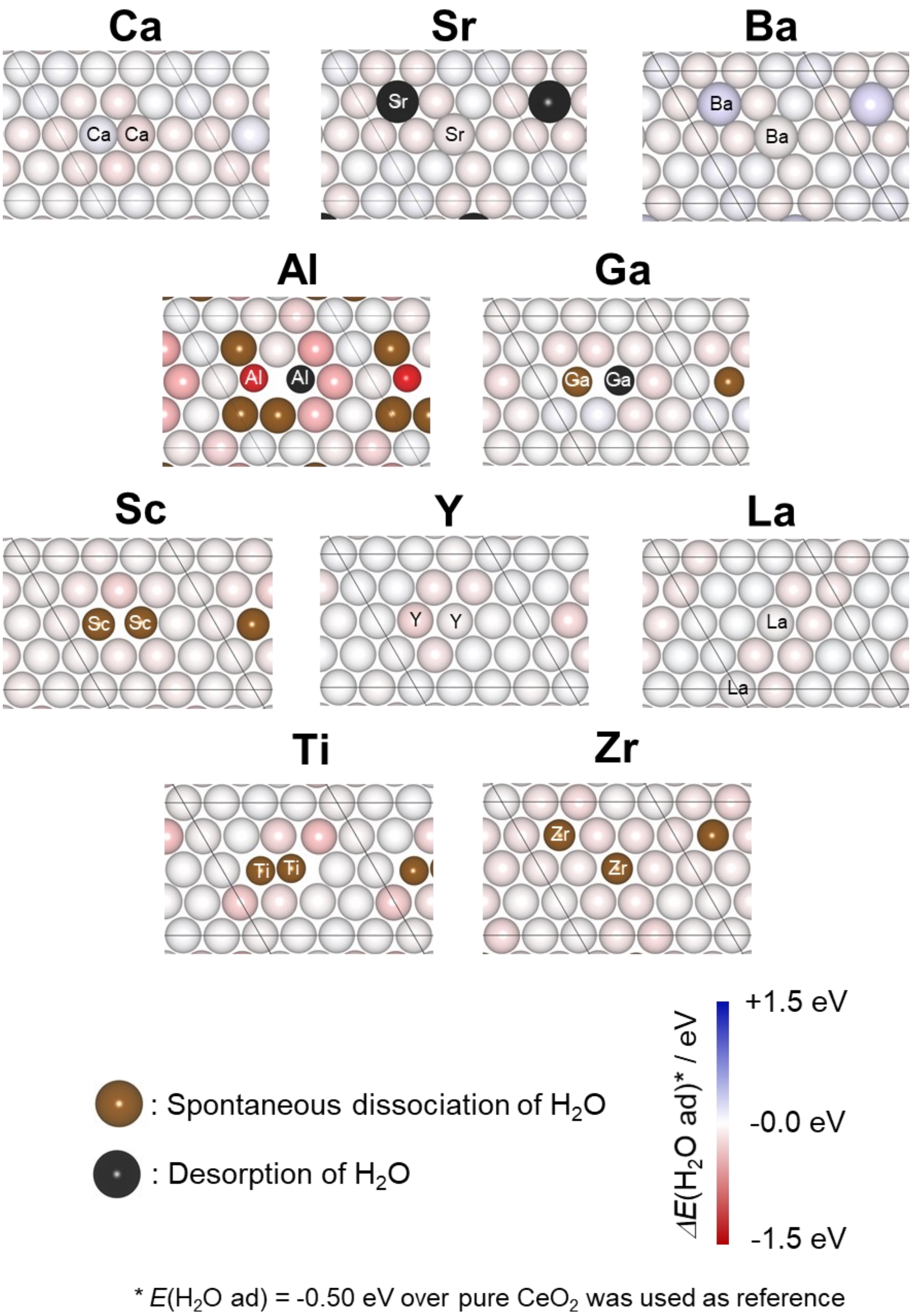

Figure 2.7. Energy map of the H_2O molecular adsorption. The balls are colored along with the difference in the *E*(H_2O ad) over pristine CeO_2 (111). Red balls represent the stronger adsorption of H_2O. Blue balls show the opposite site. Brown and black balls meant that the H_2O spontaneous dissociate and desorb over those sites, respectively. Copyright 2020 AIP Publishing.

Secondly, we investigated the heterocation-doping effects on H_2O dissociative adsorption. The dissociation of H_2O is an important step for various catalytic reactions. [51] The formed OH plays a key role in surface protonics under H_2O atmosphere. [52] In Fig. 2.8, the change of H_2O dissociative adsorption energy (ΔE(H_2O dis)) along with heterocation doping was depicted in the same manner as shown in Fig. 2.7. When H_2O dissociated over surfaces, OH adsorbed onto cation sites, and H atom adsorbed onto the outermost O_{lat} sites. The value of E(H_2O dis) is calculated as shown below.

$$E(H_2O\text{ dis}) = E(\text{slab with dissociative adsorbed } H_2O) - E(\text{slab without } H_2O) - E(\text{molecular } H_2O) \quad (2.4)$$

Here, E(slab with dissociative adsorbed H_2O) presents the energy of the slab with H and OH derived from H_2O. Figure 2.7 and Fig. 2.8 used the common color scale to compare the role of heterocations on E(H_2O ad) and E(H_2O dis) clearly. The color map shown in Fig. 2.8 showed a more vivid color contrast than Fig. 2.7 showed, signifying that heterocation doping has stronger influences on H_2O dissociative adsorption than on H_2O molecular adsorption. Consequently, it can be inferred that heterocation doping can manipulate the interaction between H atoms and outermost O_{lat}. Details of this inference are evaluated in the next chapter. Returning to Fig. 2.8, the heterocation-doping effects are remarkable next to heterocations, as might be apparent in surfaces with small dopants (Al, Ga, Sc, and Ti). However, the effects were local. In contrast, Zr doping globally facilitates the H_2O dissociative adsorption because the Zr prefers to be mutually separated on the CeO_2 (111) surface.

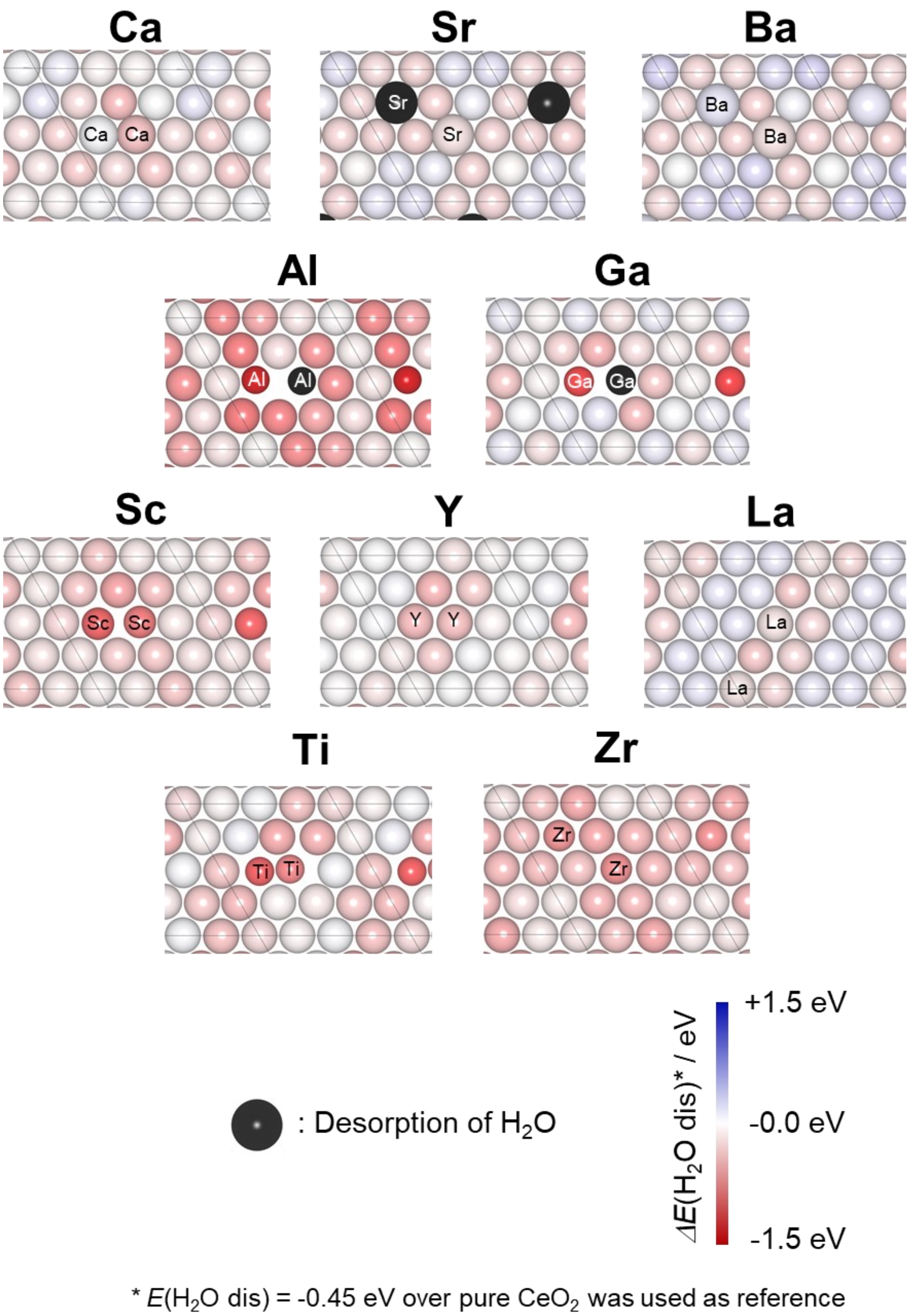

Figure 2.8. Energy map of the H_2O dissociative adsorption. The balls are colored along with the difference in the E(H_2O dis) over pristine CeO_2 (111). Red balls represent the stronger adsorption of H_2O. Blue balls show the opposite site. Brown and black balls meant that the H_2O spontaneous desorb over those sites. Copyright 2020 AIP Publishing.

To clarify the correlation between H_2O dissociative adsorption and ionic radius of heterocations, we show E(H_2O dis) with an ionic radius, as shown in Fig. 2.9. In the figure, E(H_2O dis) are grouped as follows: (i) "dopant" – the H_2O dissociative adsorption over heterocations; (ii) “nnce (nearest neighbor Ce)” – the H_2O dissociative adsorption at Ce next to heterocations; and (iii) “nnnce (next nearest neighbor Ce)” – the Ce atoms which are next nearest neighbors to heterocations. Points in Fig. 2.9 represent the average values at the respective sites ((i)–(iii)). Regarding the general trend, the promotion effect of heterocations with small ionic radii on H_2O dissociative adsorption is apparent. This trend is useful as an extremely useful milestone when we try to tune the catalysis related to surface protonics under a H_2O atmosphere. Furthermore, this study showed that facilitation by heterocations with smaller ionic radii are localized in nature. The enhancement of dispersion of heterocations also plays a key role.

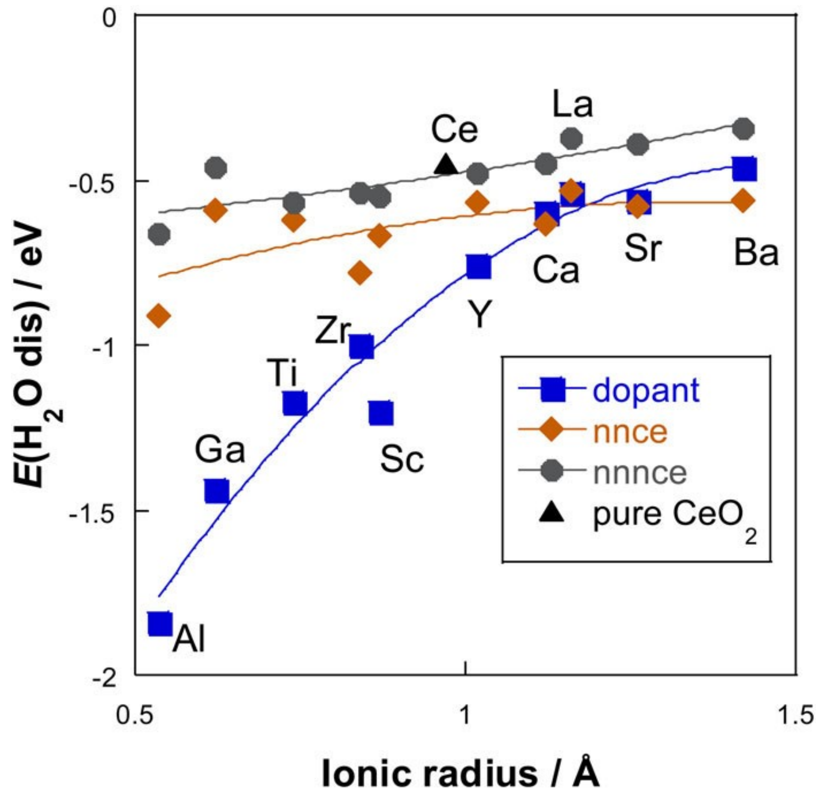

Figure 2.9. Correlation between the ion radius of heterocations and average of E(H_2O dis) at each site. The legends stand for the H_2O adsorption site. The "dopant” shows dopant sites, “nnce” means Ce next to dopants, and “nnnce” represents the next nearest neighbor Ce. Copyright 2020 AIP Publishing.

2.3.4. Observation of hydroxy groups over CeO_2-based materials

In-situ DRIFTS measurements were taken to investigate heterocation-doping effects on OH groups experimentally over CeO_2-based materials suggested by DFT calculations. Commonly, the peaks observed when H_2O is supplied include the effects of multilayer adsorption of H_2O. However, we considered heterocation-doping effects on the adsorption of a single H_2O using DFT calculations. We evaluated the OH groups that directly adsorb over cations with the following approach. First, CeO_2-based materials were pretreated under mild conditions (473 K for 1 h under Ar). After pre-treatment, small amounts of OH groups remain over surfaces of CeO_2-based materials. When H_2O is supplied to such pre-treated surfaces, OH-residuals interacted with supplied H_2O. Because of this interaction, the frequencies assigned to the OH species are red-shifted. Negative peaks are observed. [53]

Figure 2.10 presents spectra over CeO_2 from 1 to 30 min after H_2O supply. Negative peaks were observed at around 3720 cm^{-1} and 3650 cm^{-1}. Those peaks were assignable to terminal ("*t*-OH", one bond between OH and surface cations) and multi-coordinated ("*m*-OH", two or more bonds between OH and surface cations) OH groups over CeO_2 surfaces. [54, 55] The peaks at around 3670 cm^{-1} were attributable to the red-shift of peaks assigned to *t*-OH. The broad bands at lower than 3600 cm^{-1} are derived from H-bonded H_2O. Those band intensities increased over time, indicating the increment of H_2O adsorbed over CeO_2. Bands at around 3800–4000 cm^{-1} did not change to any marked degree, which suggests that the H_2O supply mainly caused not a blue-shift but a red-shift of OH-derived peaks.

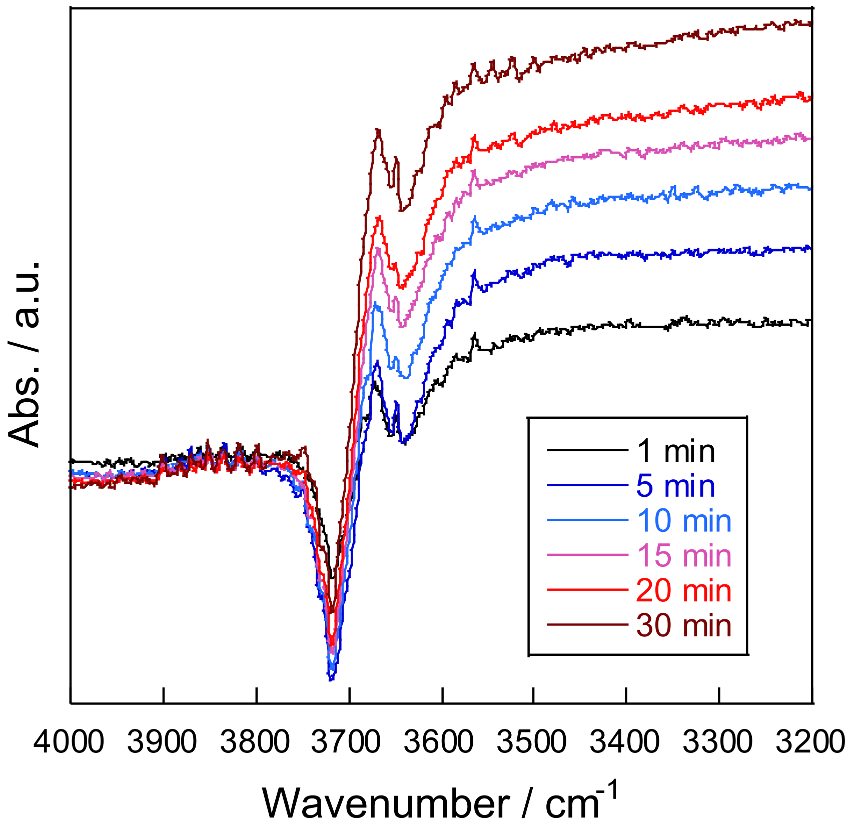

Figure 2.10. Time-course analysis of *in-situ* DRIFTS spectra for CeO_2 under Ar (59.7 SCCM) and H_2O (0.3 SCCM) at 473 K.

Heterocation-doping effects on the H_2O adsorption were considered using peaks assigned to *t*-OH. Figure 2.11 presents the obtained spectra over $Ce_{0.9}M_{0.1}O_{2-\delta}$ (M: Sr, Al, and Zr). Results show that Al doping and Zr doping led to a marked blue-shift of *t*-OH peaks. As described earlier, DFT calculations suggest that those two dopants (Al and Zr) had a much more positive influence on H_2O adsorption. The correlation between the experimentally obtained *t*-OH wavenumber and the average of DFT-calculated H_2O dissociative adsorption energies was considered (Fig. 2.12).

Results indicate strong correlation between those two values. In this manner, the validity of DFT-obtained heterocation-doping effects on H_2O adsorption was elucidated using *in-situ* DRIFTS measurements.

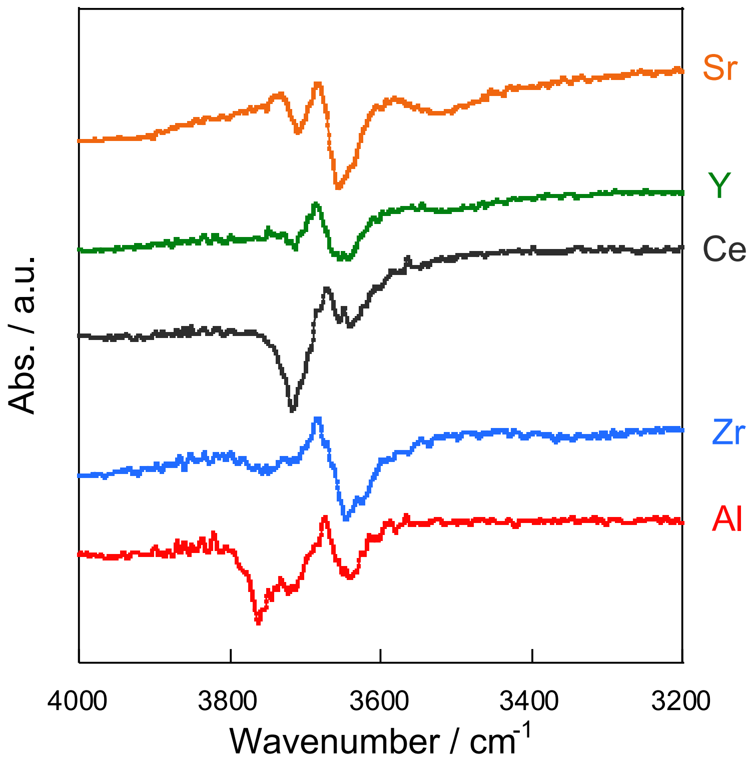

Figure 2.11. Heterocation-doping effects on *in-situ* DRIFTS spectra under Ar (59.7 SCCM) and H_2O (0.3 SCCM) at 473 K.

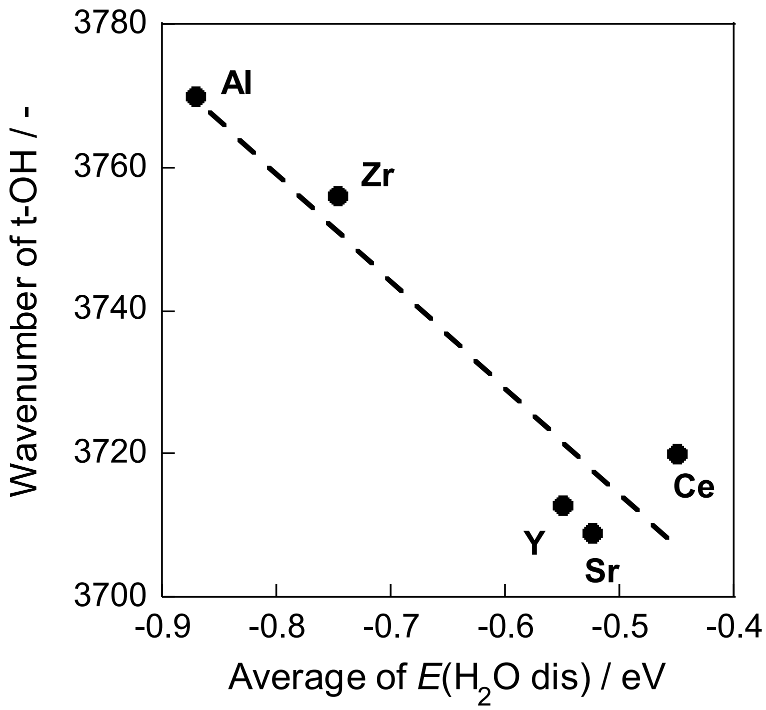

Figure 2.12. Correlation between wavenumber and average of DFT-calculated $E(H_2O$ dis).

2.4. Chapter conclusion

Effects of heterocation doping on interaction between H_2O and CeO_2 have been revealed using DFT calculations. Moreover, the DFT-obtained results were confirmed experimentally using XRD, Raman, and *in-situ* DRIFTS measurements. Consequently, valence and ionic radius were found to be key factors for heterocation distribution and heterocation-doping effects on H_2O adsorption. Heterocations with lower valence and smaller ionic radii tend to adjoin mutually. That led to localization of the heterocation-doping effects. Regarding H_2O adsorption, heterocations with small cations facilitated the adsorption. In addition, much greater facilitation effects were observed for dissociative adsorption than for molecular adsorption, which means that heterocation doping has much greater influence on adsorption over O_{lat} than that over cations. An evident reason why small heterocation-doped surfaces are feasible is examined in the next chapter along with other factors manipulating the adsorption energies.

References

1. H. C. Yao, and Y. F. Yu Yao, Ceria in automotive exhaust catalysts: I. Oxygen storage, *J. Catal*. 1984, **86(2)**, 254 – 265.
2. J. Kašper, P. Fornasiero, and M. Graziani, Use of CeO_2-based oxides in the three-way catalysis, *Catal*. *Today*, 1999, **50**, 285 – 298.
3. J. Llorca, N. Homs, J. Sales, and P. R. Piscina, Efficient Production of Hydrogen over Supported Cobalt Catalysts from Ethanol Steam Reforming, *J. Catal*., 2002, **209**, 306 – 317.
4. C. N. Xian, H. Li, L. Q. Chen, and J. S. Lee, Morphological and catalytic stability of mesoporous peony-like ceria, *Microporous Mesoporous Mat*., 2011, **142 (1)**, 202 – 207.
5. Q. Fu, A. Weber, and M. Flytzani-Stephanopoulos, Active nonmetallic Au and Pt species on ceria-based water-gas shift catalysts, *Science*, 2003, **301**, 935 – 938.
6. J. A. Rodriguez, S. Ma, P. Liu, J. Hrbek, J. Evans, and M. Pérez, Activity of CeO_x and TiO_x Nanoparticles Grown on Au(111) in the Water-Gas Shift Reaction, *Science*, 2007, **14**, 1757 – 1760.
7. C. Schilling and C. Hess, Elucidating the Role of Support Oxygen in the Water–Gas Shift Reaction over Ceria-Supported Gold Catalysts Using *Operando* Spectroscopy, *ACS Catal*., 2019 **9(2)**, 1159 – 1171.
8. Y. Ogura, K. Sato, S. Miyahara, Y. Kawano, T. Toriyama, T. Yamamoto, S. Matsumura, S. Hosokawa, and K. Nagaoka, Efficient ammonia synthesis over a $Ru/La_{0.5}Ce_{0.5}O_{1.75}$ catalyst pre-reduced at high temperature, *Chem*. *Sci*., 2018, **9**, 2230 – 2237.
9. B. Lin, Y. Heng, X. Wang, J. Ni, J. Lin, and L. Jiang, Preparation of a Highly Efficient Carbon-Supported Ruthenium Catalyst by Carbon Monoxide Treatment, *Ind*. *Eng*. *Chem*. *Res*., 2018, **57(28)**, 9127 – 9135.
10. R. Manabe, S. Okada, R. Inagaki, K. Oshima, S. Ogo, and Y. Sekine, Surface protonics promotes catalysis, *Sci*. *Rep*., 2016, **6**, 38007.
11. R. Inagaki, R. Manabe, Y. Hisai, Y. Kamite, T. Yabe, S. Ogo, Y. Sekine, Steam reforming of dimethyl ether promoted by surface protonics in an electric field, *Int. J. Hydrog*. *Energy*, 2018, **43(31)**, 14310 – 14318.
12. S. Kumar and P. K. Schelling, Density functional theory study of water adsorption at reduced and stoichiometric ceria (111) surfaces, *J. Chem*. *Phys*., 2006, **125**, 204704.
13. H. T. Chen, Y. M. Choi, M. Liu, and M. C. Lin, A Theoretical Study of Surface Reduction Mechanisms of CeO_2(111) and (110) by H_2, *ChemPhysChem*, 2007, **8**, 849–855.
14. M. B. Watkins, A. S. Foster, and A. L. Shluger, Hydrogen Cycle on CeO_2 (111) Surfaces: Density Functional Theory Calculations, *J. Phys*. *Chem*. *C*, 2007, **111(42)**, 15337 – 15341.
15. M. Fronzi, S. Piccinin, B. Delley, E. Traversa, and C. Stampfl, Water adsorption on the stoichiometric and reduced CeO_2(111) surface: a first-principles investigation, *Phys*. *Chem*. *Chem*. *Phys*., 2009, **11**, 9188–9199.

16. D. F. Torre, K. Kośmider, J. Carrasco, M. V. G. Pirovano, and R. Pérez, Insight into the Adsorption of Water on the Clean $CeO_2(111)$ Surface with van der Waals and Hybrid Density Functionals, *J. Phys. Chem. C*, 2012, **116**, 13584 – 13593.
17. A. Röckert, J. Kullgren, P. Broqvist S. Alwan, and K. Hermansson, The water/ceria(111) interface: Computational overview and new structures, *J. Chem. Phys.*, 2020, **152**, 104709.
18. T. Baidya, A. Gupta, P. A. Deshpandey, G. Madras, and M. S. Hegde, High Oxygen Storage Capacity and High Rates of CO Oxidation and NO Reduction Catalytic Properties of $Ce_{1-x}Sn_xO_2$ and $Ce_{0.78}Sn_{0.2}Pd_{0.02}O_{2-\delta}$, *J. Phys. Chem. C*, 2009, 113, 4059 – 4068.
19. T. Baidya, M. S. Hegde, and J. Gopalakrishnan, Oxygen-Release/Storage Properties of $Ce_{0.5}M_{0.5}O_2$ (M = Zr, Hf) Oxides: Interplay of Crystal Chemistry and Electronic Structure, *J. Phys. Chem. B*, 2007, **111**, 5149 – 5154.
20. G. Dutta, U. V. Waghmare, T. Baidya, M. S. Hegde, K. R. Priolkar, and P. R. Sarode, Origin of Enhanced Reducibility/Oxygen Storage Capacity of $Ce_{1-x}Ti_xO_2$ Compared to CeO_2 or TiO_2, *Chem. Matter.*, 2006, **18(14)**, 3249 – 3256.
21. Y. Nagai, T. Yamamoto, T. Tanaka, S. Yoshida, T. Nonaka, T. Okamoto, A. Suda, and M. Sugiura, X-ray absorption fine structure analysis of local structure of CeO_2–ZrO_2 mixed oxides with the same composition ratio (Ce/Zr=1), *Catal. Today*, 2002, **74**, 225 – 234.
22. G. Vlaic, P. Fornasiero, S. Geremia, J. Kašpar, and M. Graziani, Relationship between the Zirconia-Promoted Reduction in the Rh-Loaded $Ce_{0.5}Zr_{0.5}O_2$Mixed Oxide and the Zr–O Local Structure, *J. Catal.*, 1997, **168(2)**, 386 – 392
23. C. E. Hori, H. Permana, K. Y. S. Ng, A. Bernner, K. More, K. M. Rahmoeller, and D. Belton, Thermal stability of oxygen storage properties in a mixed CeO_2-ZrO_2 system, *Appl. Catal. B: Environ.*, 1998, **16**, 105 – 117.
24. B. Liu, C. Li, G. Zhang, X. Yao, S. S. C. Chuang, and Z. Li, Oxygen Vacancy Promoting Dimethyl Carbonate Synthesis from CO_2 and Methanol over Zr-Doped CeO_2 Nanorods, *ASC Catal.*, 2018, **8(11)**, 10446 – 10456.
25. B. C. H. Steele, Appraisal of $Ce_{1-y}Gd_yO_{2-y/2}$ electrolytes for IT-SOFC operation at 500°C, Solid State Ionics, 2000, **129(1 – 4)**, 95 – 110 (2000).
26. Y. Q. Su, I. A. W. Filot, J. X. Liu, and E. J. M. Hensen, Stable Pd-Doped Ceria Structures for CH_4 Activation and CO Oxidation, *ACS Catal.*, 2018, **8(1)**, 75 – 80.
27. V. J. Ferreria, P. Tavares, J. L. Figueiredo, and J. L. Faria, Effect of Mg, Ca, and Sr on CeO_2 Based Catalysts for the Oxidative Coupling of Methane: Investigation on the Oxygen Species Responsible for Catalytic Performance, *Ind. Eng. Chem. Res.*, 2012, **51**, 10535 – 10541.
28. A. Takahashi, R. Inagaki, M. Torimoto, Y. Hisai, T. Matsuda, Q. Ma, J. G. Seo, T. Higo, H. Tsuneki, S. Ogo, T. Norby and Y. Sekine, Effects of metal cation doping in CeO_2 support on catalytic methane steam reforming at low temperature in an electric field, *RSC Adv.*, 2020, **10**, 14487 – 14492.

29. G. Kresse and J. Hafner, *Ab initio* molecular dynamics for liquid metals, *Phys. Rev. B*, 1993, **47**, 558 – 561.
30. G. Kresse and J. Hafner, *Ab initio* molecular-dynamics simulation of the liquid-metal–amorphous-semiconductor transition in germanium, *Phys. Rev. B*, 1994, **49**, 14251 – 14269.
31. G. Kresse, J. Furthmüller, Efficiency of ab-initio total energy calculations for metals and semiconductors using a plane-wave basis set, *Comput. Mat. Sci.*, 1996, **6(1)**, 15 – 50.
32. G. Kresse, J. Furthmüller, Efficient iterative schemes for *ab initio* total-energy calculations using a plane-wave basis set, *Phys. Rev. B*, 1996, **54**, 11169 – 11186.
33. J. P. Perdew, K. Burke, and M. Ernzerhof, Generalized Gradient Approximation Made Simple, *Phys. Rev. Lett.*, 1996, **77**, 3865 – 3868.
34. H. J. Monkhorst and J. D. Pack, Special points for Brillouin-zone integrations, *Phys. Rev. B*, 1976, **13**, 5188 – 5192.
35. S. Grimme, J. Antony, S. Ehrlich, and S. Krieg, A consistent and accurate *ab initio* parametrization of density functional dispersion correction (DFT-D) for the 94 elements H-Pu, *J. Chem. Phys.*, 2010, **132**, 154104.
36. M. D. Krcha, A. D. Mayernick, and M. J. Janik, Periodic trends of oxygen vacancy formation and C–H bond activation over transition metal-doped CeO_2 (1 1 1) surfaces, *J. Catal.*, 2012, **293**, 102 – 115.
37. H. T. Chen and J. G. Chang, Oxygen vacancy formation and migration in Ce1−*x*Zr*x*O2 catalyst: A DFT+U calculation, *J. Chem. Phys.*, 2010, **132**, 214702.
38. M. Nolan, Healing of oxygen vacancies on reduced surfaces of gold-doped ceria, *J. Chem. Phys.*, 2009, **130**, 144702.
39. M. Nolan, Enhanced oxygen vacancy formation in ceria (111) and (110) surfaces doped with divalent cations, *J. Mater. Chem.*, 2011, **21**, 9160 – 9168.
40. M. Nolan, Charge Compensation and Ce^{3+} Formation in Trivalent Doping of the CeO_2(110) Surface: The Key Role of Dopant Ionic Radius, *J. Phys. Chem. C*, 2011, **115**, 6671 – 6681.
41. Z. X. Yang, G. X. Luo, Z. S. Lu, and K. Hermansson, Oxygen vacancy formation energy in Pd-doped ceria: A DFT+U study, *J. Chem. Phys.*, 2007, **127**, 074704.
42. A. D. Mayernick, and M. J. Janik, Methane Activation and Oxygen Vacancy Formation over CeO_2 and Zr, Pd Substituted CeO_2 Surfaces, *J. Phys. Chem. C*, 2008, **112(38)**, 14955 – 14964.
43. P. R. L. Keatingm, D. O. Scanlon, and G. W. Watson, The nature of oxygen states on the surfaces of CeO_2 and La-doped CeO_2, *Chem. Phys. Lett.*, 2014, **608**, 239 – 243.
44. Y. G. Wang, D. Mei, J. Li, and R. Rousseau, DFT+U Study on the Localized Electronic States and Their Potential Role During H_2O Dissociation and CO Oxidation Processes on CeO_2(111) Surface, *J. Phys. Chem. C*, 2013, **117**, 23082 – 23089.
45. S. Rhatigan and M. Nola, CO_2 and water activation on ceria nanocluster modified TiO_2 rutile (110), *J. Mater. Chem. A*, 2018, **6(19)**, 9139 – 9152.
46. H. A. Hansen and C. Wolverton, Kinetics and Thermodynamics of H_2O Dissociation on Reduced CeO_2(111), *J. Phys. Chem. C*, 2014, **118**, 27402 – 27414.

47. E. Zen, Validity of "vegard's law", *Am. Mineral.*, 1956, **41**, 523 – 524.
48. J. E. Spanier, R. D. Robinson, F. Zhang, S. W. Chan, and I. P. Herman, Size-dependent properties of CeO_{2-y} nanoparticles as studied by Raman scattering, *Phys. Rev. B*, 2001, **64**, 245407.
49. J. Guzman, S. Carrettin, and A. Corma, Spectroscopic Evidence for the Supply of Reactive Oxygen during CO Oxidation Catalyzed by Gold Supported on Nanocrystalline CeO_2, *J. Am. Chem. Soc.*, 2005, **127(10)**, 3286 – 3287.
50. Y. M. Choi, H. Abernathy, H. T. Chen, M. C. Lin and M. Liu, Characterization of O_2-CeO_2 interactions using in situ Raman spectroscopy and first-principle calculations, *ChemPhysChem*, 2006, **7**, 1957 – 1963.
51. M. Li, Y. Song, and G. Wang, The Mechanism of Steam-Ethanol Reforming on Co_{13}/CeO_{2-x}: A DFT Study, *ACS Catal.*, 2019, **9**, 2355 – 2367.
52. R. Sato, S. Ohkuma, Y. Shibuta, F. Shimojo, and S. Yamaguchi, Proton Migration on Hydrated Surface of Cubic ZrO2: Ab initio Molecular Dynamics Simulation, *J. Phys. Chem. C*, 2015, **119**, 28925 – 28933.
53. E. Köck, M. Kogler, B. Klötzer, M. F. Noistering, and S. Penner, Structural and Electrochemical Properties of Physisorbed and Chemisorbed Water Layers on the Ceramic Oxides Y_2O_3, YSZ, and ZrO_2, *ACS Appl. Mater. Interfaces*, 2016, **8**, 16428 – 16443.
54. A. Badri, C. Binet, and J. C. Lavalley, An FTIR study of surface ceria hydroxy groups during a redox process with H_2, *J. Chem. Soc., Faraday Trans.*, 1996, **92 (23)**, 4669 – 4673.
55. C. Binet, M. Daturi, and J. C. Lavalley, IR study of polycrystalline ceria properties in oxidised and reduced states, *Catal. Today*, 1999, **50**, 207 – 225.

Appendix of Chapter 2

A.2.1. Effects of O_{vac} formation and backfilling of O_{vac} by H_2O on electronic state of O 1*s*

Doping of lower valent heterocations into metal oxides is known to cause the formation of localized electron holes on the O_{lat}. [1-3] O_{vac} and OH^- formed by backfilling of O_{vac} compensate this charge deviation. The O 2*p* PEDOS of CeO_2(111) and heterocations (Ba or Sc)-doped CeO_2 (111) surfaces were considered to elucidate this phenomenon (Figures A.2.8 – A.2.10). For both heterocations, spin-up unoccupied states were confirmed above Fermi level when charge compensation by O_{vac} or backfilling was not considered. Those polarization represent the O^- polaron formation by doping with lower valent heterocations. Such unoccupied states were not observed for the calculation models with O_{vac} and OH termination. It indicates that the charge difference was compensated by O_{vac} formation and OH termination.

A.2.2. Calculation models with dopants in subsurface

Th models that have heterocations at subsurface were calculated for several cations (Ba, Al, Sc and Zr). Figure A.2.11 describes the considered arrangement of dopants. Geometry optimization was conducted in the similar manner as shown in the main text. Al doping did not lead to the formation of peroxide for this heterocation arrangement. Figure A.2.12 represents the obtained surfaces and energy maps for H_2O molecular adsorption and dissociative adsorption. The energy map was drawn in the same way as Figures 2.7 and 2.8 The heterocation-doping effects for this arrangement is similar to that shown in Figures 2.7 and 2.8. Firstly, heterocation-doping has stronger influences on H_2O dissociative adsorption than H_2O molecular adsorption. Additionally, doping of cations with smaller ionic radius (Al and Sc) facilitates the H_2O adsorption.

References

1. M. Nolan, and G. W. Watson, The electronic structure of alkali doped alkaline earth metal oxides: Li doping of MgO studied with DFT-GGA and GGA + *U*, *Surf. Sci.*, 2005, **586(1 – 3)**, 25 – 37.
2. M. Nolan, and G. W. Watson, Hole localization in Al doped silica: A DFT+*U* description, *J. Chem. Phys.*, 2006, **126**, 144701.
3. O. F. Schirmer, O^- bound small polarons in oxide materials, *J. Phys.*; *Condens. Matter.*, 2006, **18**, 667 – 704.

Figures and Tables

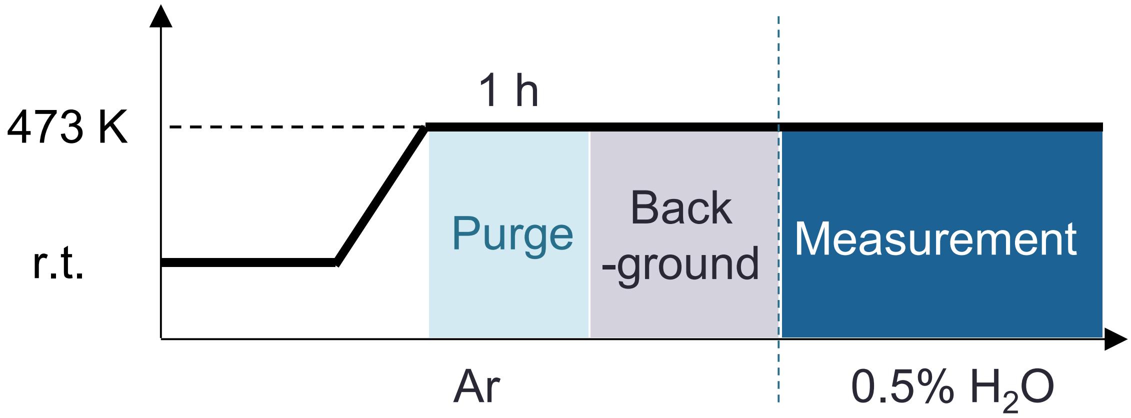

Figure A.2.1. Flow of *in-situ* DRIFTS measurement.

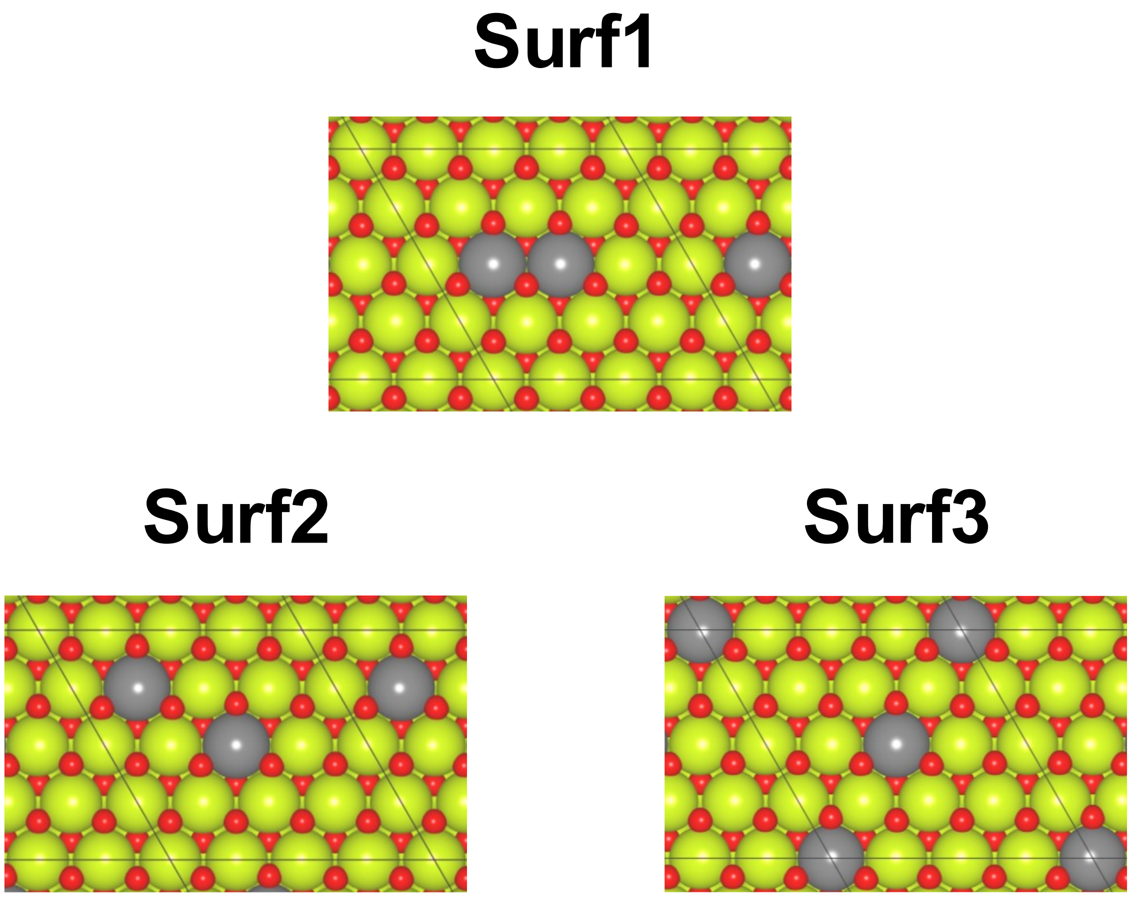

Figure A.2.2. Heterocation distributions considered in DFT calculations. Yellow ball means Ce, red stands for O, and gray shows heterocation. Copyright 2020 AIP Publishing.

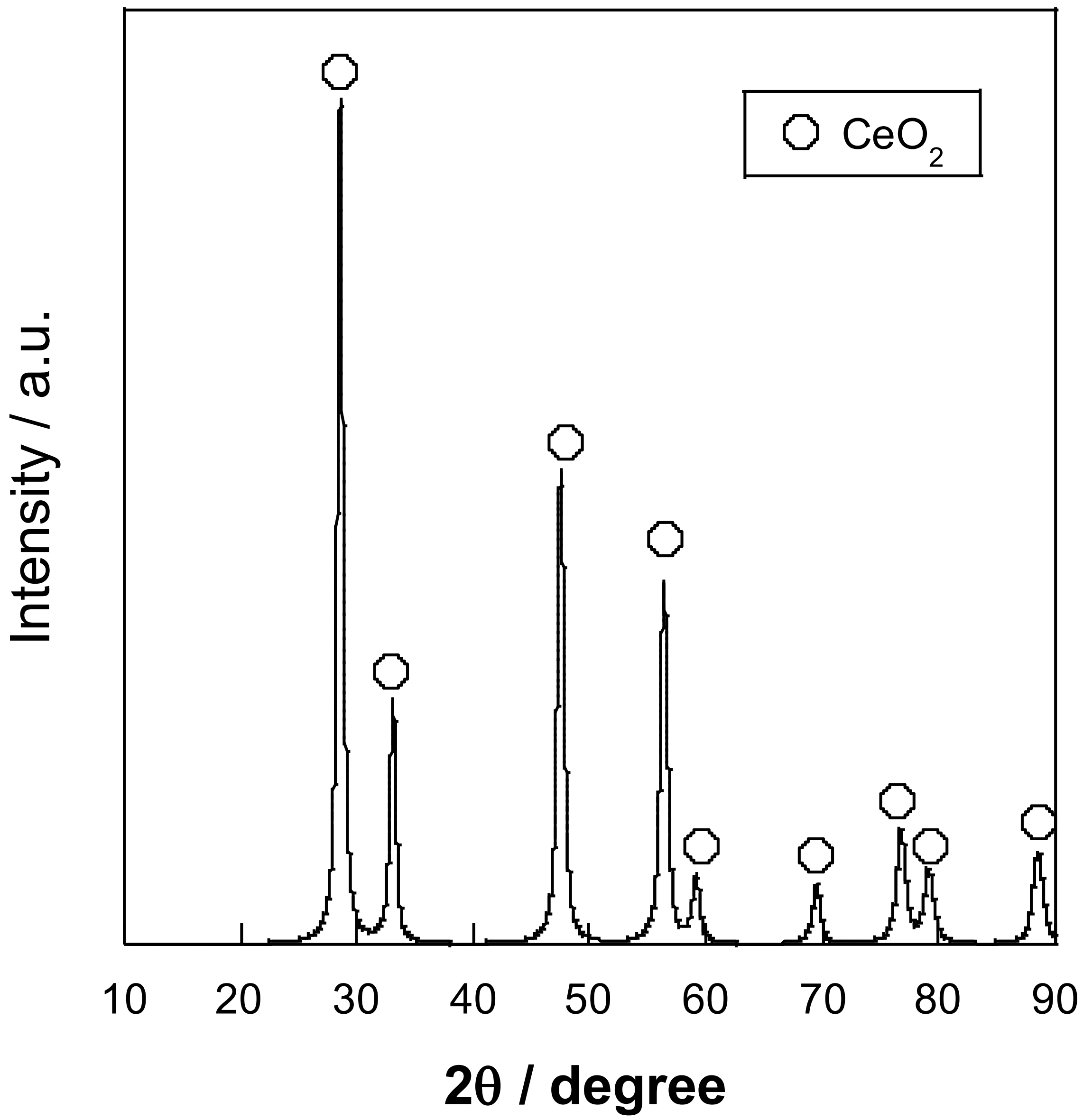

Figure A.2.3. XRD spectrum of CeO_2.

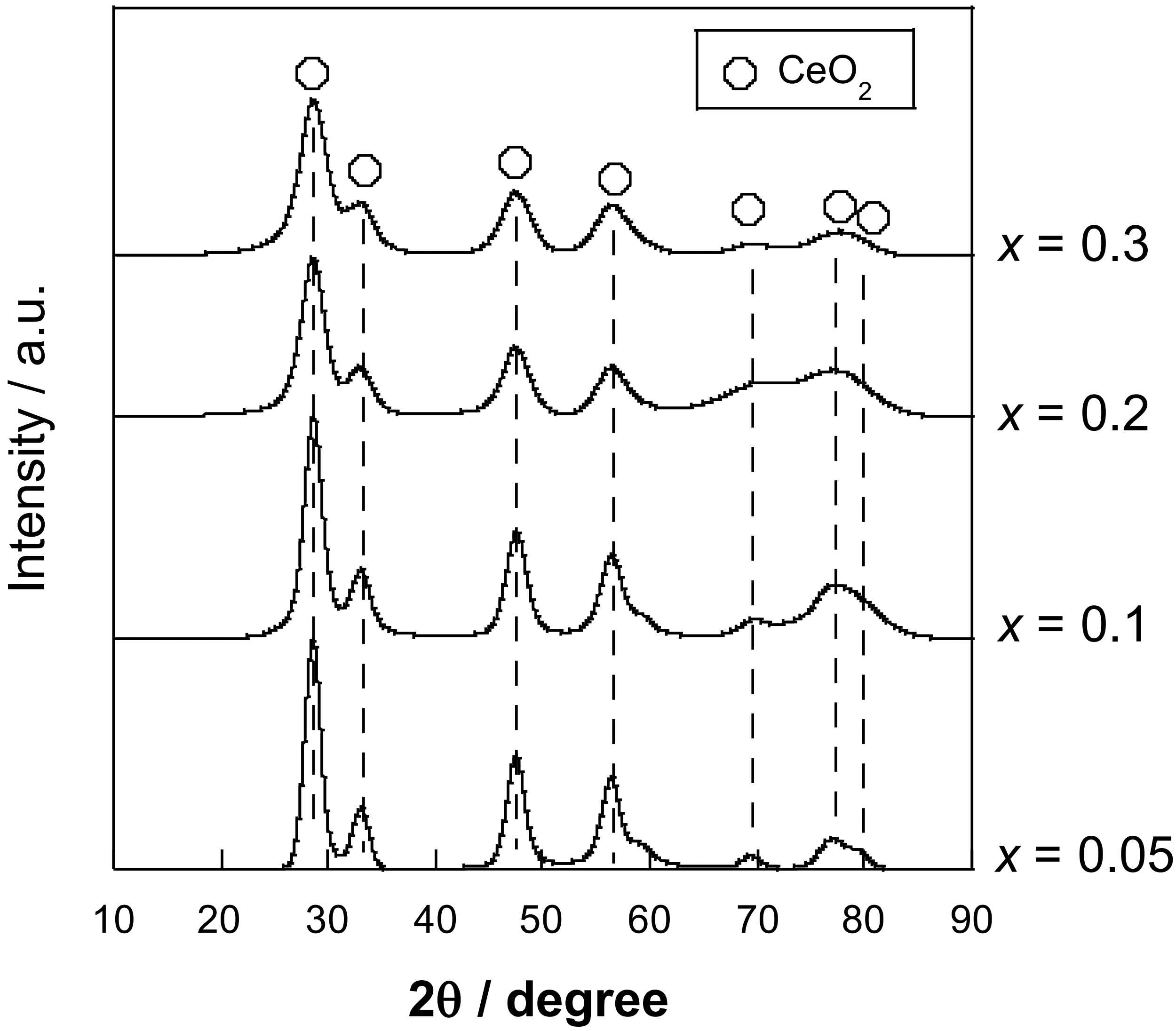

Figure A.2.4. XRD spectra of $Ce_{1-x}Al_xO_{2-\delta}$ (x = 0.05, 0.1, 0.2, 0.3).

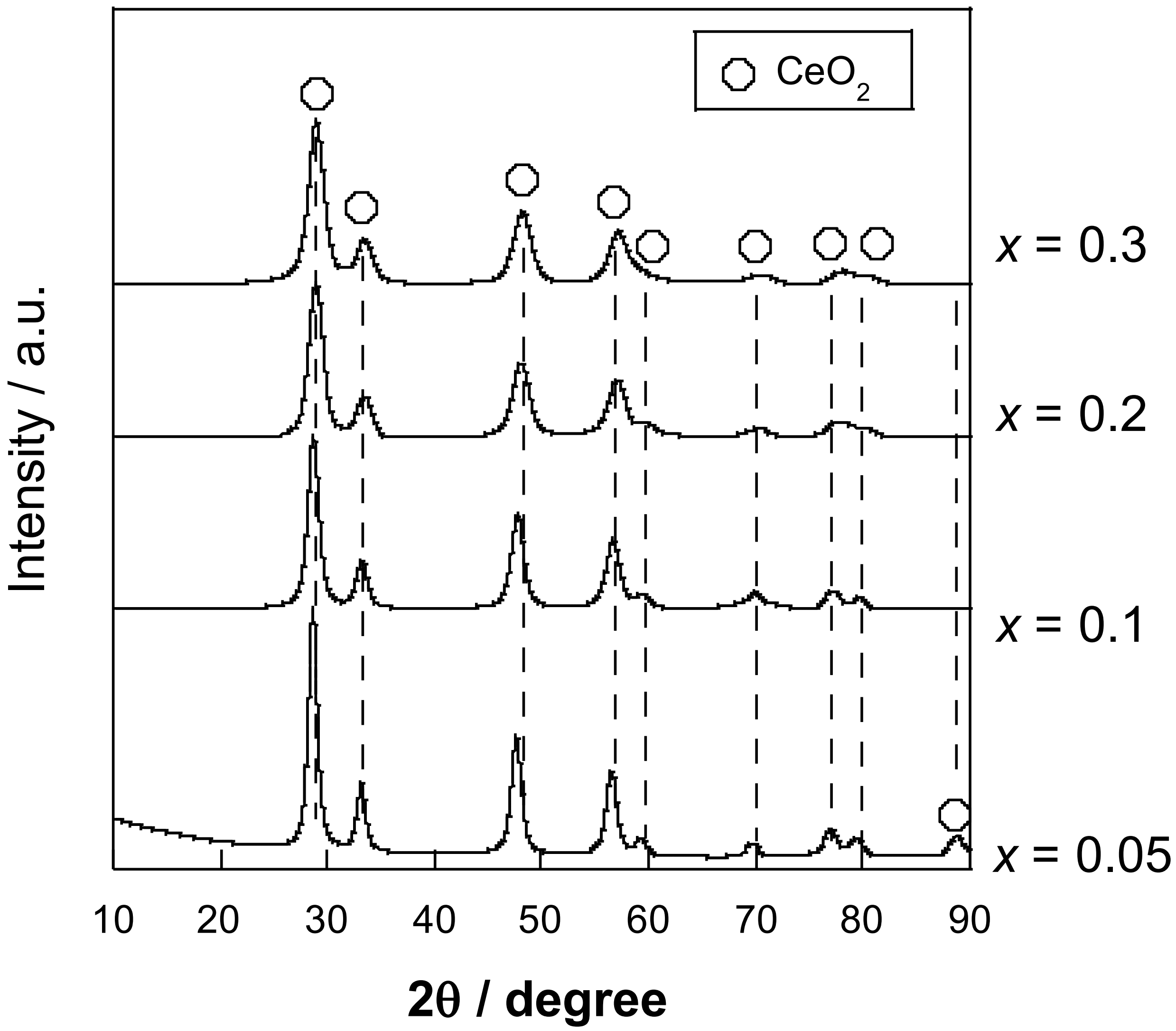

Figure A.2.5. XRD spectra of $Ce_{1-x}Zr_xO_{2-\delta}$ (x = 0.05, 0.1, 0.2, 0.3).

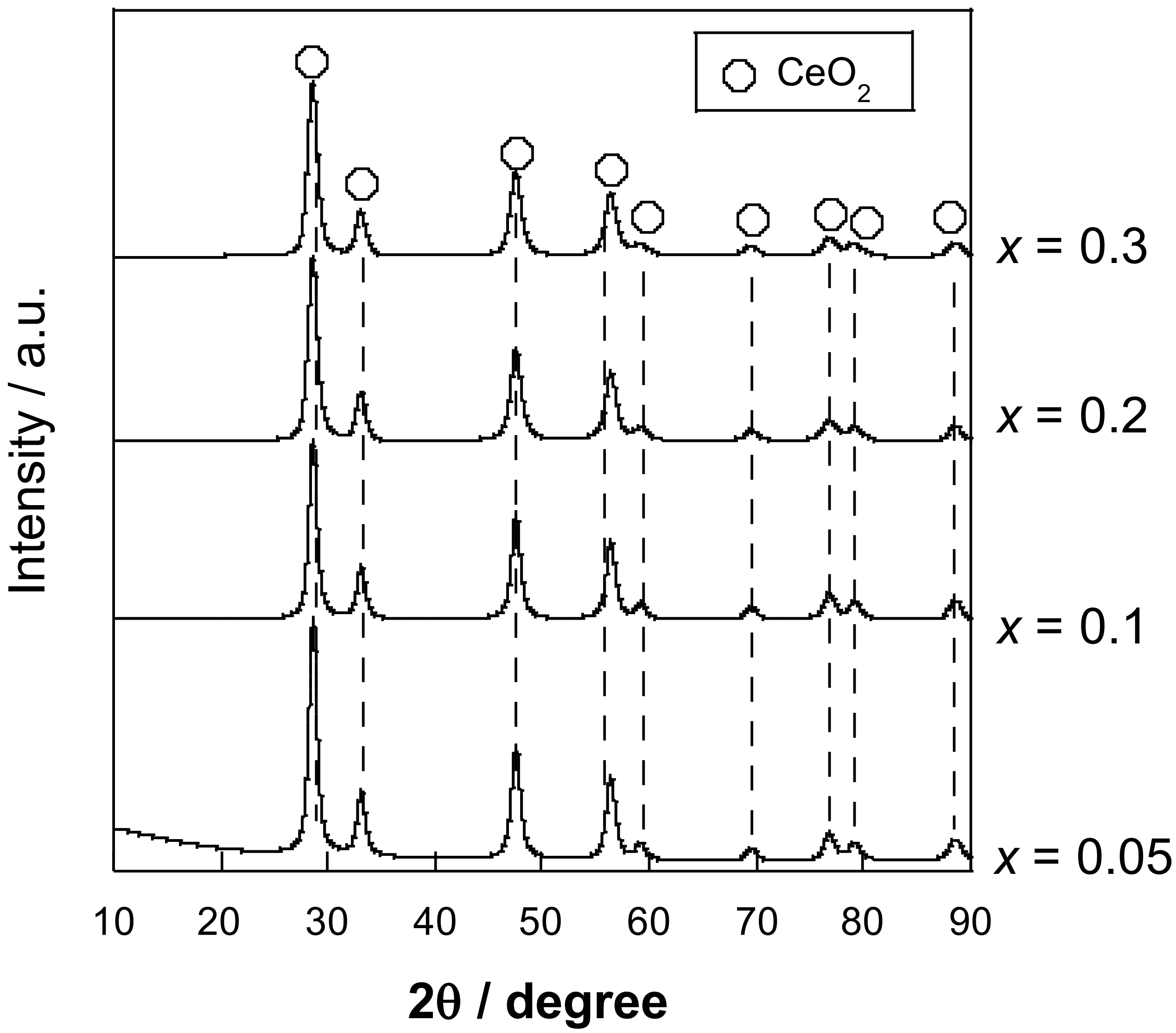

Figure A.2.6. XRD spectra of $Ce_{1-x}Y_xO_{2-\delta}$ (x = 0.05, 0.1, 0.2, 0.3).

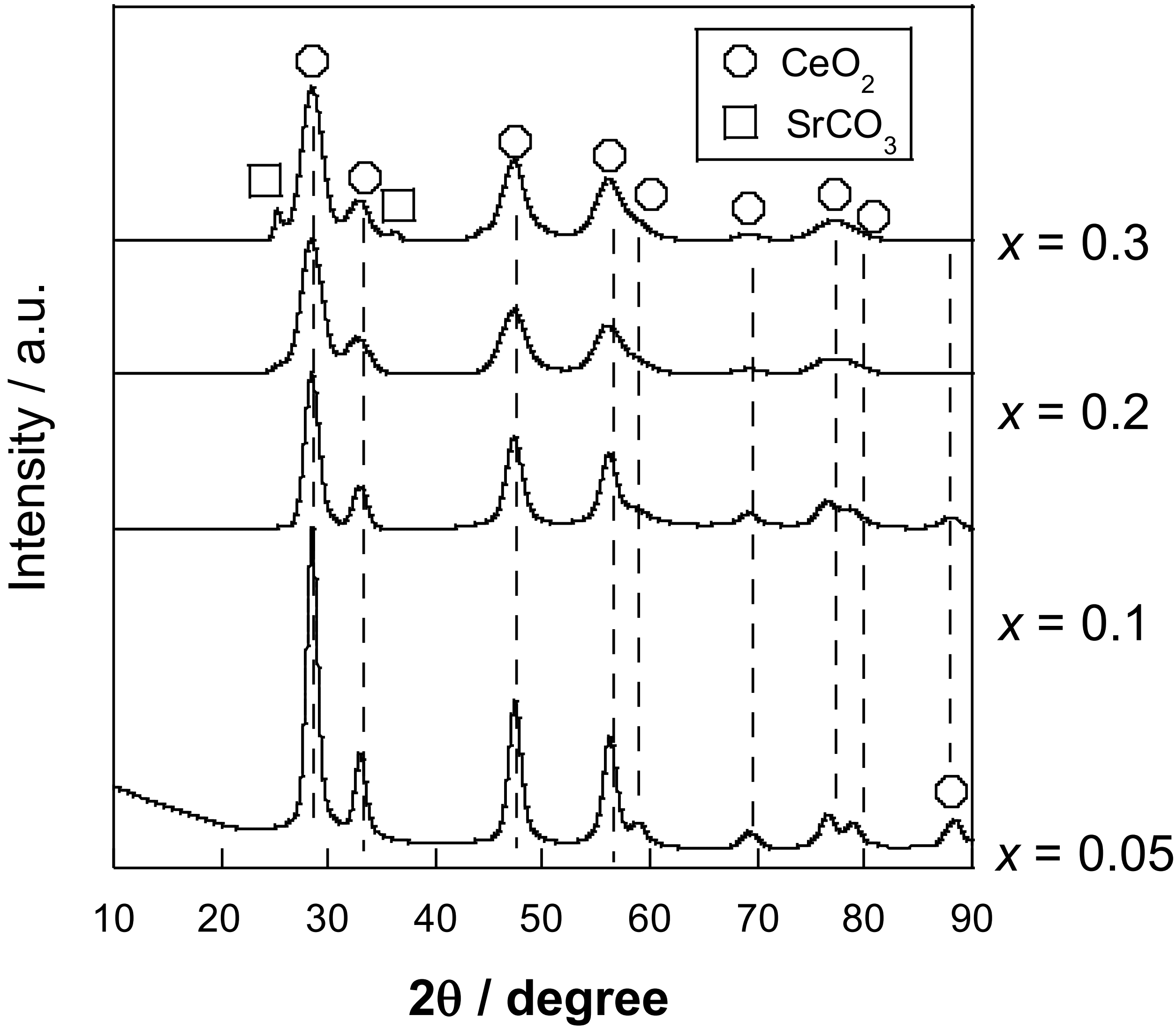

Figure A.2.7. XRD spectra of $Ce_{1-x}Sr_xO_{2-\delta}$ (x = 0.05, 0.1, 0.2, 0.3).

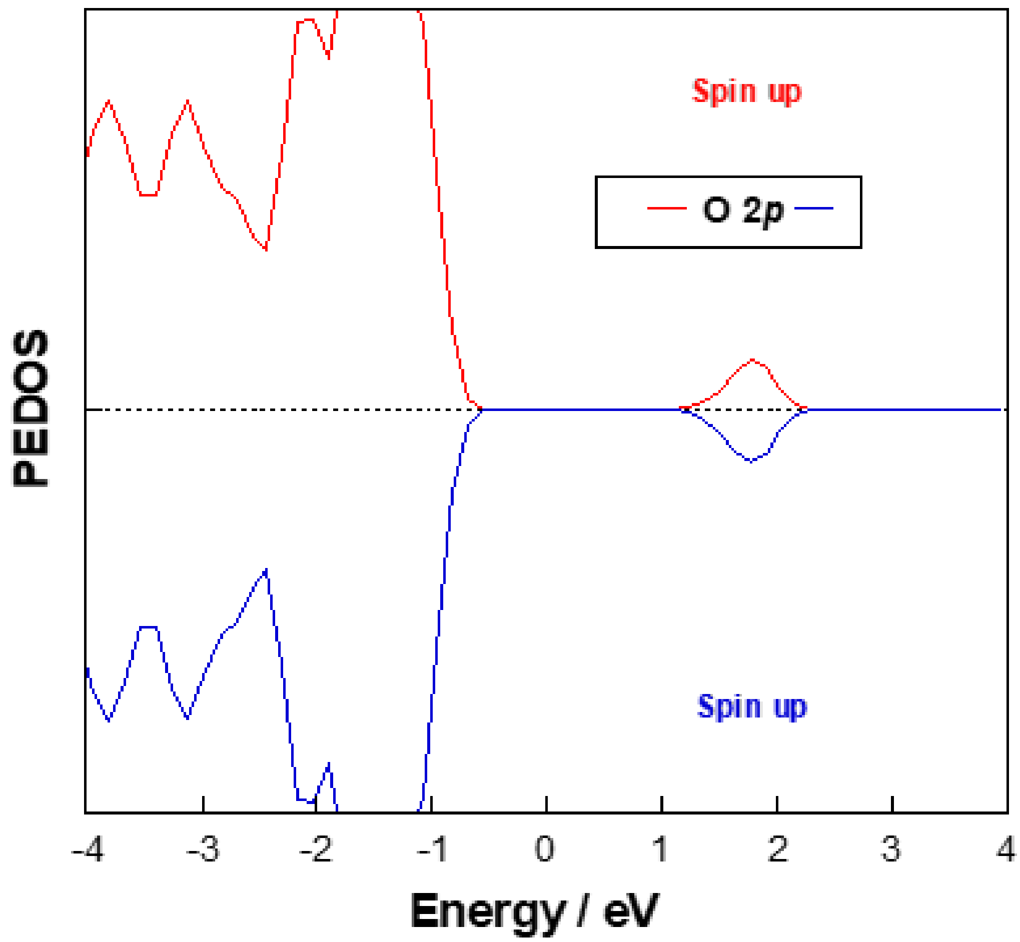

Figure A.2.8. PDOS of O 2*p* for CeO_2 (111) surface. Copyright 2020 AIP Publishing.

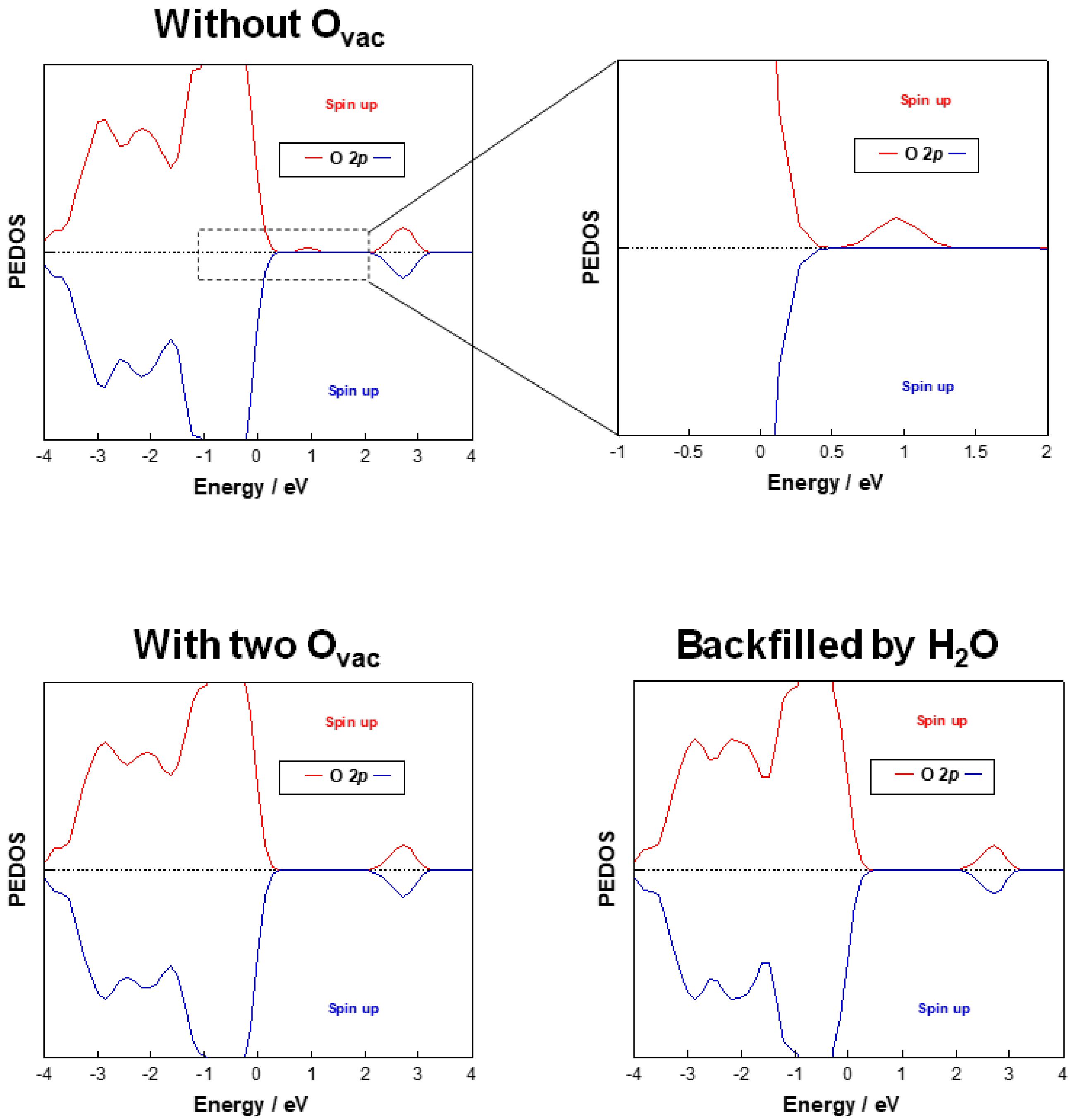

Figure A.2.9. PDOS of O 2*p* for Ba doped CeO_2 (111) surface. Copyright 2020 AIP Publishing.

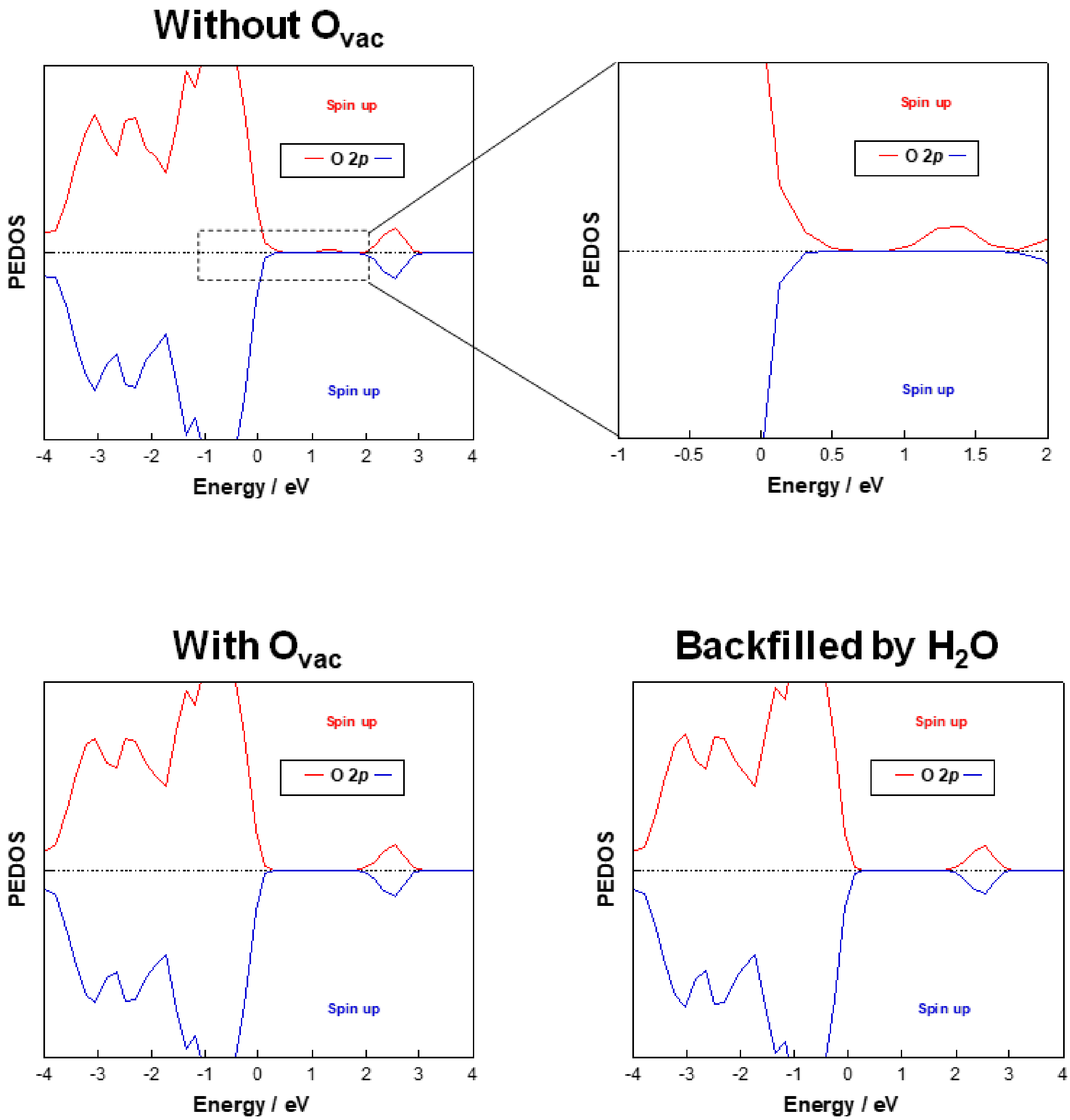

Figure A.2.10. PDOS of O 2*p* for Sc-doped CeO_2 (111) surface. Copyright 2020 AIP Publishing.

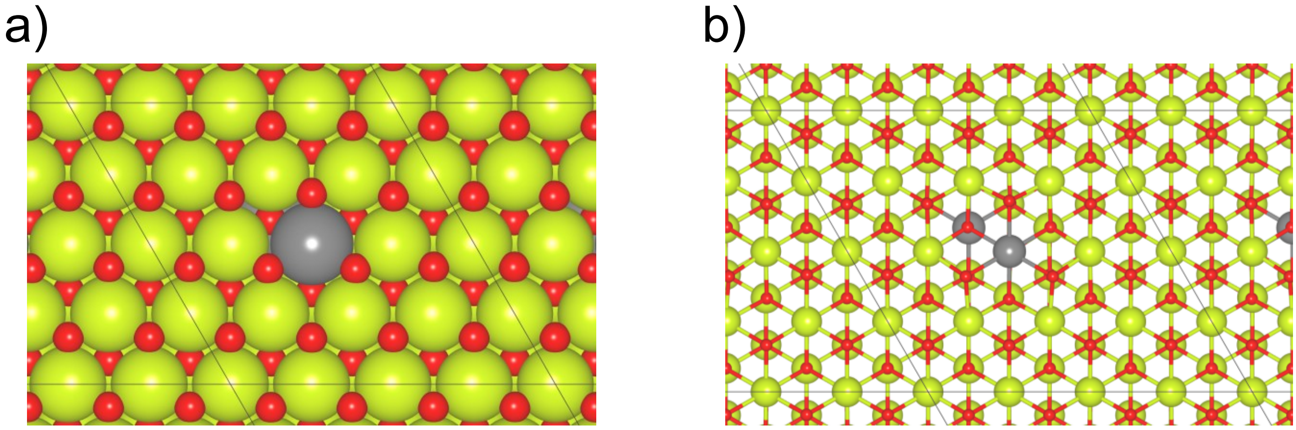

Figure A.2.11. The calculation model that contains at both surface and subsurface.: a) top view, b) top view described using small balls. Yellow ball means Ce, red stands for O, and gray shows heterocation. Copyright 2020 AIP Publishing.

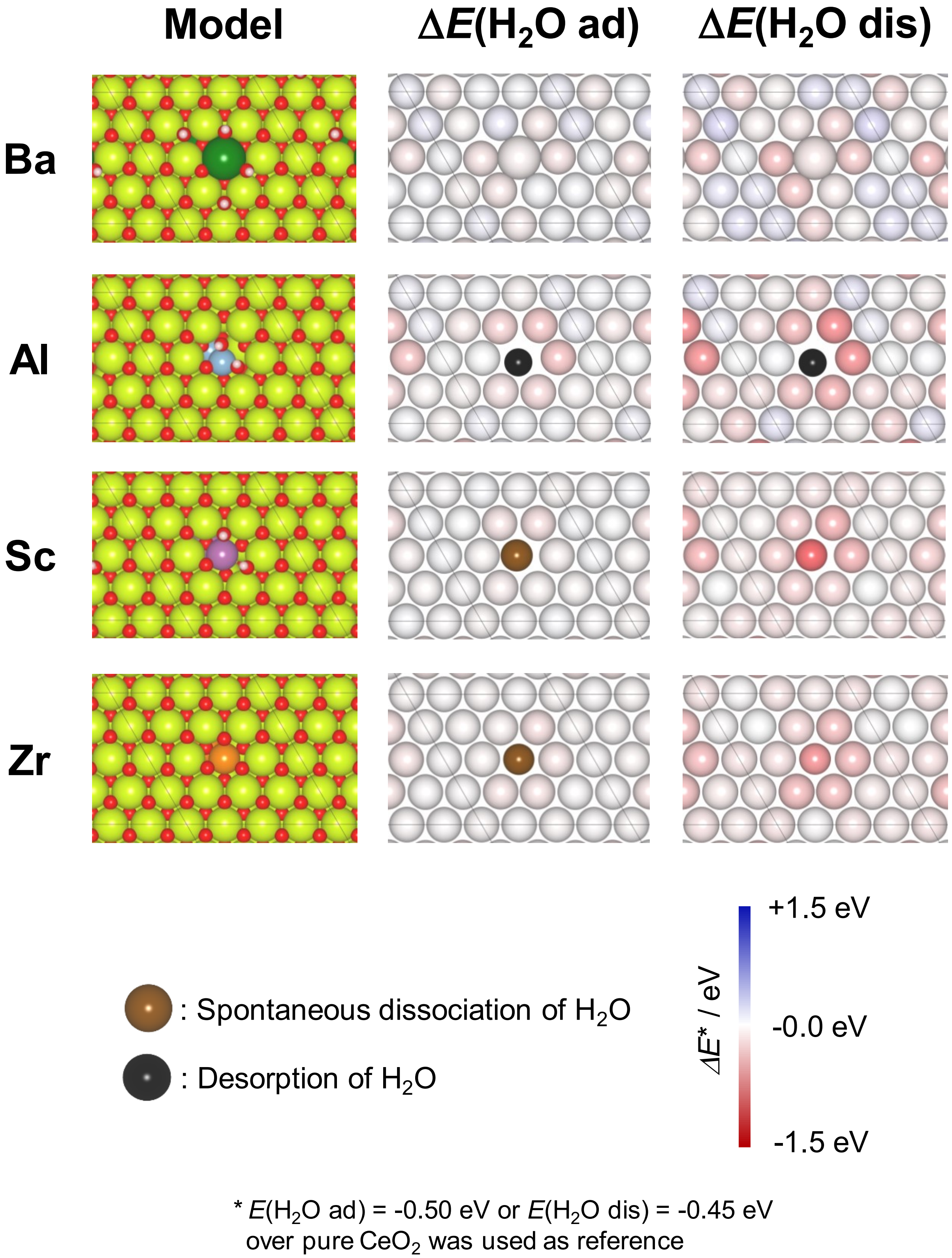

Figure A.2.12. Energy map of the H_2O molecular and dissociative adsorption over calculation models shown in Figure A.2.11. The balls are colored along with the difference in the E(H_2O dis) over pristine CeO_2 (111). Red balls represent the stronger adsorption of H_2O. Blue balls show the opposite site. Brown and black balls meant that the H_2O spontaneous desorb over those sites. Copyright 2020 AIP Publishing.

Table A.2.1. The valence configuration used for DFT calculations.

Atom /-	Valence configuration / -
Al	$3s^2 3p^1$
Ba	$6s^2$
Ca	$4s^2$
Ce	$4f^1 5s^2 5p^6 5d^1 6s^2$
Ga	$3d^{10} 4s^2 4p^1$
H	$1s^1$
La	$5s^2 5p^6 5d^1 6s^2$
O	$1s^2 2s^2 2p^5$
Sc	$3d^1 4s^2$
Sr	$5s^2$
Ti	$3d^2 4s^2$
Y	$4d^1 5s^2$
Zr	$4s^2 4p^6 4d^2 5s^2$

Table A.2.2. Precursors used for preparation of $Ce_{1-x}M_xO_{2-\delta}$.

Cation / -	Precursor / -
Sr	$Sr(NO_3)_2$
Al	$Al(NO_3)_3 \cdot 9H_2O$
Y	$Y(NO_3)_3 \cdot 6H_2O$
Zr	$ZrO(NO_3)_2 \cdot 2H_2O$
Ce	$Ce(NO_3)_3 \cdot 6H_2O$

Table A.2.3. The energy differences from the most stable heterocation arrangements with several amounts of O_{vac} (n). The options of arrangements are shown in Figure A.2.2. The most stable configurations are shown in Figure 2.3. Copyright 2020 AIP Publishing.

Dopant / -	Amount of O_{vac} (n) / -	Dopant arrangement / -	Energy difference from the most stable arrangement / eV
Ba	0	Surf1	0.40
		Surf2	0.00
		Surf3	0.29
	1	Surf1	0.44
		Surf2	0.00
		Surf3	0.25
	2	Surf1	0.47
		Surf2	0.00
		Surf3	0.09
Ga	0	Surf1	0.00
		Surf2	0.99
		Surf3	1.11
	1	Surf1	0.00
		Surf2	0.66
		Surf3	0.75
Sc	0	Surf1	0.00
		Surf2	0.62
		Surf3	0.67
	1	Surf1	0.00
		Surf2	0.52
		Surf3	0.63

Chapter 3 H atom–CeO_2 Interaction Control by Heterocation Doping

The content in this chapter is partly reproduced from K. Murakami, Y. Mizutani, H. Sampei, A. Ishikawa, Y. Tanaka, S. Hayashi, S. Doi, T. Higo, H. Tsuneki, H. Nakai, and Y. Sekine, Theoretical prediction by DFT and experimental observation of heterocation-doping effects on hydrogen adsorption and migration over CeO_2 (111) surface, *Phys. Chem. Chem. Phys.*, *in press*. DOI: 10.1039/D0CP05752E. Copyright RSC Publishing.

3.1. Introduction

H atom adsorption and migration under H_2O and H_2 atmosphere is fundamentally important in the field of catalysis, as described in Chapter 1. [1] Therefore, clear guidelines for controlling the amount and reactivity of H^+ are necessary to facilitate the development of catalytic reactions related to hydroxy groups (OH).

Doping of heterocations into the metal oxides is a promising means of tuning catalyst performance. Reportedly, it can modify various features such as the redox properties [2–10] and subtraction of H atom adsorption related to the cleavage of H–H, C–H, and O–H bond. [11–13] Therefore, in-depth knowledge of heterocation-doping effects is critically important.

In Chapter 2, heterocation-doping effects on interaction between OH and CeO_2 have been considered under a H_2O atmosphere. Results suggest the importance of the ionic radii of heterocation. Herein, we specifically examined heterocation-doping effects on H atom interaction onto CeO_2-based compounds under H_2 atmosphere. Furthermore, we investigated the role of ionic radius and other factors which can be expected to control the interaction. To separate the conceivable heterocation-doping effects (*e.g.* electron transfer induced by heterocations, lattice strain induced by heterocations, lattice strain induced by adsorption) clearly, we applied DFT calculations with multiple flows.

3.2. Experimental

3.2.1. Computational details

We performed all DFT calculations for divalent (Ca, Sr, Ba), trivalent (Al, Ga, Sc, Y, La), and quadrivalent (Hf, Zr, Ti) heterocation-doped CeO_2 in the same conditions as those presented in chapter 2. All calculations were performed using software (VASP 5.4.4). [14–17] Configurations of the valence electrons used for all calculations are presented in Table A.3.1. The PAW method including PBE was applied to expression of the core–valence effect. [18] The cutoff energy was set as 400 eV. Spin polarization was considered. Regarding the *k*-space, 0.04 $Å^{-1}$ in Monkhorst–Pack reciprocal space was used for bulk structures. Also, (1 × 1 × 1) mesh was adopted for surface models. [19] Gaussian smearing was used. The effects of van der Waals force were applied using the DFT-D3 method of Grimme. [20] On-site Coulomb repulsion of Ce 4*f* orbitals was expressed using DFT + *U* method. The *U* value was set as 5.0 eV. [13, 21–27]

A CeO_2 (111) surface was constructed as a repeated (4 × 4) supercell with O-Ce-O tri-layers. Each slab was separated by a 20 Å vacuum gap in the *z*-direction. Dopants were added by replacing two Ce at the uppermost surface. Unless otherwise noted, only the bottom O-Ce-O layer was fixed. H atoms were arranged on the top of the uttermost O_{lat}. Then the geometries were optimized. The calculated most-stable H atom arrangements are presented in Fig. A.3.1. Details of calculation flows are explained in section 3.3.1.

3.2.2. Sample preparation

We synthesized CeO_2 and $Ce_{0.9}M_{0.1}O_{2-\delta}$ (M: Zr, Al, Y, and Sr) using a complex polymerization method in the same manner as that described in Chapter 2. First, citric acid monohydrate and ethylene glycol were dissolved with stoichiometric precursors listed in Table A.2.2. The solution was stirred at 343 K overnight. After evaporation of solvents, the obtained powder was calcined at 773 K for 5 h.

3.2.3. X-ray photoelectron spectroscopy (XPS)

We took XPS measurements (Versa Probe II; Ulvac-Phi Inc.) with Al Kα used as an X-ray source. The spectrum was calibrated using C1*s* peaks assigned to C–H or C–C (284.8 eV). CeO_2 and $Ce_{0.9}M_{0.1}O_{2-\delta}$ (M: Zr, Al, Y, and Sr) were pre-reduced at 773 K for 1 h under N_2: H_2 = 1: 3 (total flow 240 SCCM). After reduction, the sample was transferred to the measurement system without being exposed to the atmosphere. The obtained peaks were fitted using Proctor–Sherwood–Shirley method. [28, 29]

3.3. Results and discussion

3.3.1. Construction of heterocation-doped CeO_2 (111)

We examined the effects of heterocation doping in CeO_2 on the adsorption of H atoms. We used DFT calculation schemes of three types for a clear understanding of the governing factors which control the adsorption energies (Fig. 3.1). First, surfaces of two types ("Fix surface" and "Relax surface") were constructed. "Relax surface" was constructed in the same way as that shown in part 2.3.1. In this chapter, H atom adsorption under H_2 atmosphere was considered. Therefore, surfaces without backfilling of O_{vac} by H_2O were used for subsequent calculations. The O_{vac} formation energies calculated using equation (2.1) are presented in Table A.3.2. Figure 3.2 portrays the obtained “Relax surface”. The “Fix surface” was prepared using heterocations and O_{vac} positions of “Relax surface” as follows. First, using the optimized pristine CeO_2 (111), two of the outermost Ce were replaced by heterocations. Oxygen was removed for charge compensation (as for Al, peroxide ion was set). Later, only heterocation positions were optimized, whereas all other atoms were fixed. The optimized “Fix surface” is depicted in Fig. A.3.2. Next, adsorptions of three types were considered using the two surfaces described above (“Fix surface” and “Relax surface”). Those are denoted as “Fix 1 adsorption”, “Fix 2 adsorption”, and “Relax adsorption”. Regarding “Fix 1 adsorption”, H atom was arranged over “Fix surface.” Then, only adsorbed species were relaxed. Regarding “Fix 2 adsorption” and “Relax adsorption,” adsorbates were arranged over “Relax surface.” Then, only the positions of adsorbed species were optimized for “Fix 2 adsorption”. The surface (two O-Ce-O layers) was also relaxed for “Relax adsorption.” Comparing the adsorption energies of “Fix 1 adsorption” and “Fix 2 adsorption”, the charge difference between “Fix surface” and “Relax surface” induced by lattice strain by heterocations can be considered. Additionally, the difference of adsorption energies between “Fix 2 adsorption” and “Relax adsorption” results from the reconstruction of surfaces according to adsorbed species. The comparison sheds light on effects of lattice strain during adsorption.

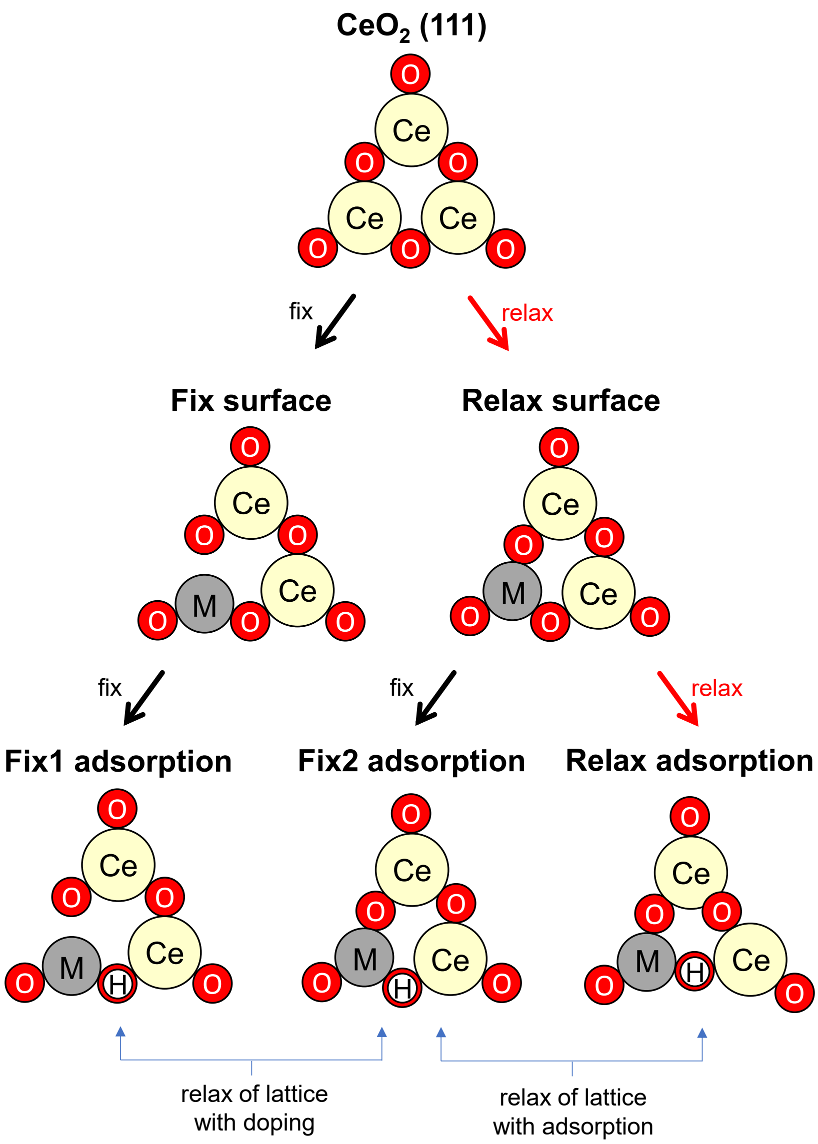

Figure 3.1. Flows of the DFT calculations. The notations "fix" and "relax" near the arrows indicate whether the atomic positions of the surface were relaxed during geometry optimization. In “Fix surface”, only the position of heterocations were optimized. In “Relax surface”, the Ce-O matrix was also optimized. “Fix surface” was applied to the calculation of “Fix1 adsorption”. Then, only the position of H atom was optimized. “Relax surface” was applied to the calculation of “Fix2 adsorption” and “Relax adsorption”. As for “Fix2 adsorption”, only the position of H atom was optimized. The Ce-O matrix was also optimized for “Relax adsorption”. Copyright 2021 RSC publishing.

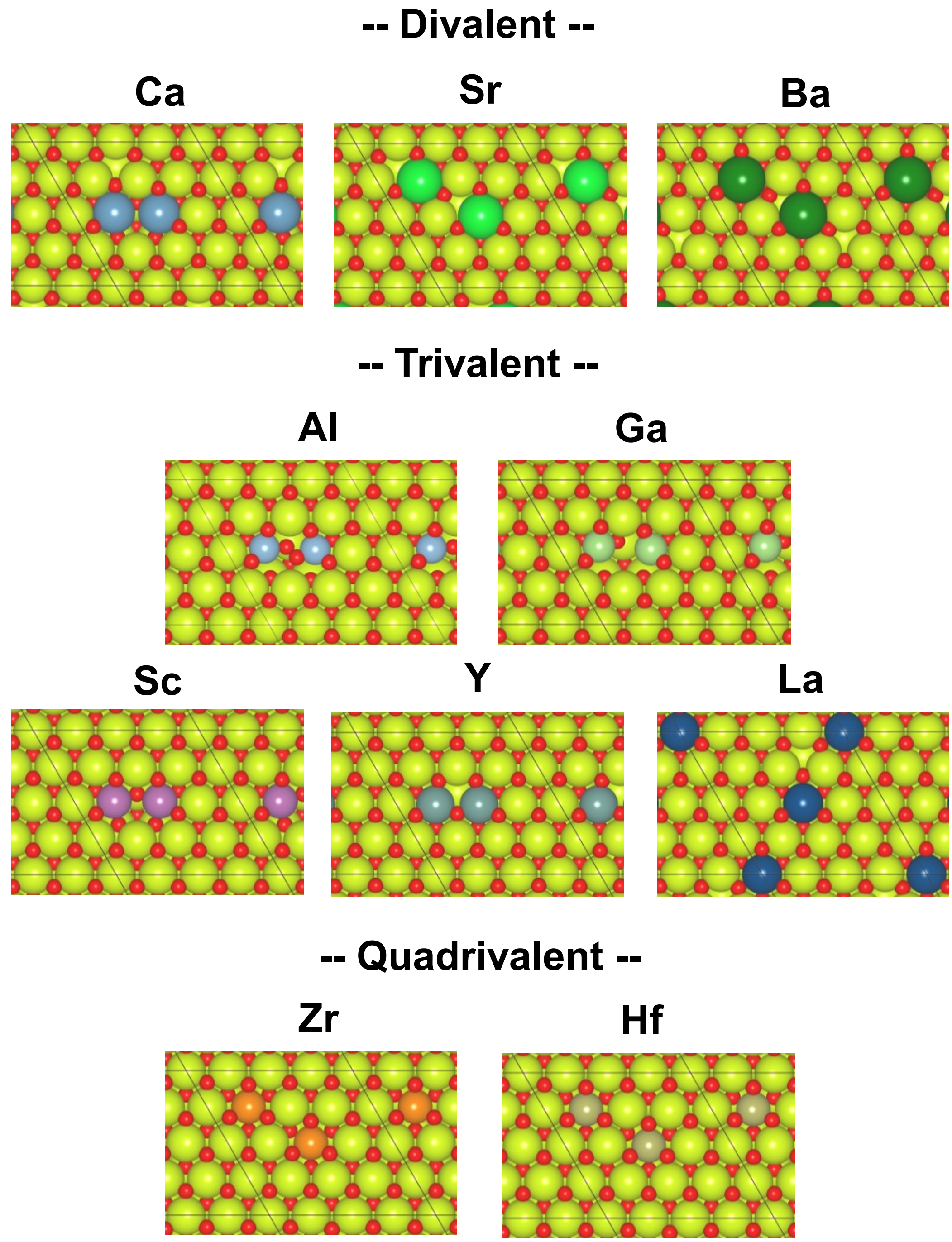

Figure 3.2. DFT-optimized CeO_2 (111) surfaces doped with heterocations considering O_{vac} formation for charge compensation. Yellow ball means Ce, red stands for O, and other colors show dopants. Copyright 2021 RSC publishing.

3.3.2. Heterocation-doping effects on H atoms adsorption over CeO_2 (111)

Reportedly, H atoms prefer to adsorb at surface oxygen. They exist as H^+ over the CeO_2 surface. [30] The H atom adsorptions at all outermost lattice oxygens (O_{lat}) were evaluated for surfaces with dopants. Hereinafter, H atoms adsorbed over O_{lat} are denoted as O_{lat}-H^+. Figure 3.3 presents box plots for H atom adsorption energies calculated through schemes shown in Fig. 3.1. Here, $E(H_{ad})$ stands for adsorption energies for "Relax adsorption". $E(H_{ad}\_fix1)$ and $E(H_{ad}\_fix2)$ respectively represent adsorption energies related to "Fix 1 adsorption" and "Fix 2 adsorption". All adsorption energies ($E(X_{ad})$) were defined as

$$E(X_{ad}) = E(\text{slab with adsorbed species}) - E(\text{slab without adsorbed species}) - 1/2\ E(H_2) \quad (3.1)$$

where *E*(slab with adsorbed species) and *E*(slab without adsorbed species) respectively show energies of surfaces with and without adsorbed species. $E(H_2)$ shows the energies of gaseous H_2. The boxes were colored based on the dopant valences. The black plots signify the average values. In addition, the boxes are arranged based on the ionic radius. Regarding "Fix 1 adsorption" shown in Fig. 3.3 (a), O_{lat}-H^+ was bound strongly by a surface with divalent heterocations. The second was trivalent. The third was quadrivalent heterocations. Reportedly, doping of heterocations with lower valences results in the formation of Lewis acid sites. [31, 32] The formation of Lewis acid sites was induced by the decrease in the electron donation from cations to O_{lat} when the original cations were replaced by less-valent cations. Because of the reasons described above, O_{lat}-H^+ was bound strongly over a surface doped with lower valent heterocations related to "Fix 1 adsorption". Evidently, this trend changed along with relaxation of two types. First is the lattice strain caused by heterocation doping corresponding to the "Fix 2 adsorption." Second is the lattice strain induced by adsorption corresponding to "Relax adsorption." The addition of heterocations with smaller ionic radii positively affected both "Fix 2 adsorption" and "Relax adsorption". Regarding lattice distortion by heterocation doping, the Ce–O bond length is crucially important. Reportedly the electronic state of Ce cations in CeO_2 including O_{vac} depends on the Ce–O bond length. [33] Therefore, it can be inferred that the Ce–O expansion led to the formation of O_{lat} that is devoid of electrons. Conversely, the shrinkage of Ce–O bond induces the formation of electron-rich O_{lat}. The surface oxygen is assumed to be pushed away to the adjacent Ce by heterocation doping with larger cations. That pushing leads to shrinkage of the Ce–O bond as shown in Fig. A.3.3. This shrinkage allows the lattice distortions to overwrite the Lewis acidity induced by heterocations with lower valences. The smaller the ionic radius of the heterocation, the greater the degree to which the influence of Ce–O bond shrinkage diminishes. The changes in the O_{lat} charge because of the heterocation doping and lattice distortion are shown in Figs. A.3.4 – A.3.9. Even with introduction of smaller heterocations, some adsorption sites were found to be more unfavorable for adsorption than sites on pristine CeO_2 without lattice relaxation during adsorption, as shown in Fig. 3.3(b). It is true because the lattice distortion by heterocation doping is complex. On surfaces doped with smaller heterocations, almost all sites bound the O_{lat}-H^+ more strongly than on the CeO_2 surface, regarding "Relax adsorption". In contrast, doping with larger heterocations hindered the adsorption. This difference between "Fix 2 adsorption" and "Relax adsorption" sheds light on the positive effects of lattice flexibility facilitated by doping of heterocations with small ionic radii. Smaller cation addition makes a room for various relaxation patterns. Lattice distortion, which is necessary for adsorption, became energetically feasible by doping of heterocations with a small ionic radius. In addition, Y-doped and Ca-doped CeO_2 (111) bound O_{lat}-H^+ more strongly than CeO_2, even though both ionic radii of dopants are larger than Ce. That strong binding indicates that the ionic radius is not the sole factor governing the adsorption energy. As elucidated in the consideration of "Fix 1 adsorption", valences of dopants also play an important role in O_{lat}-H^+ adsorption.

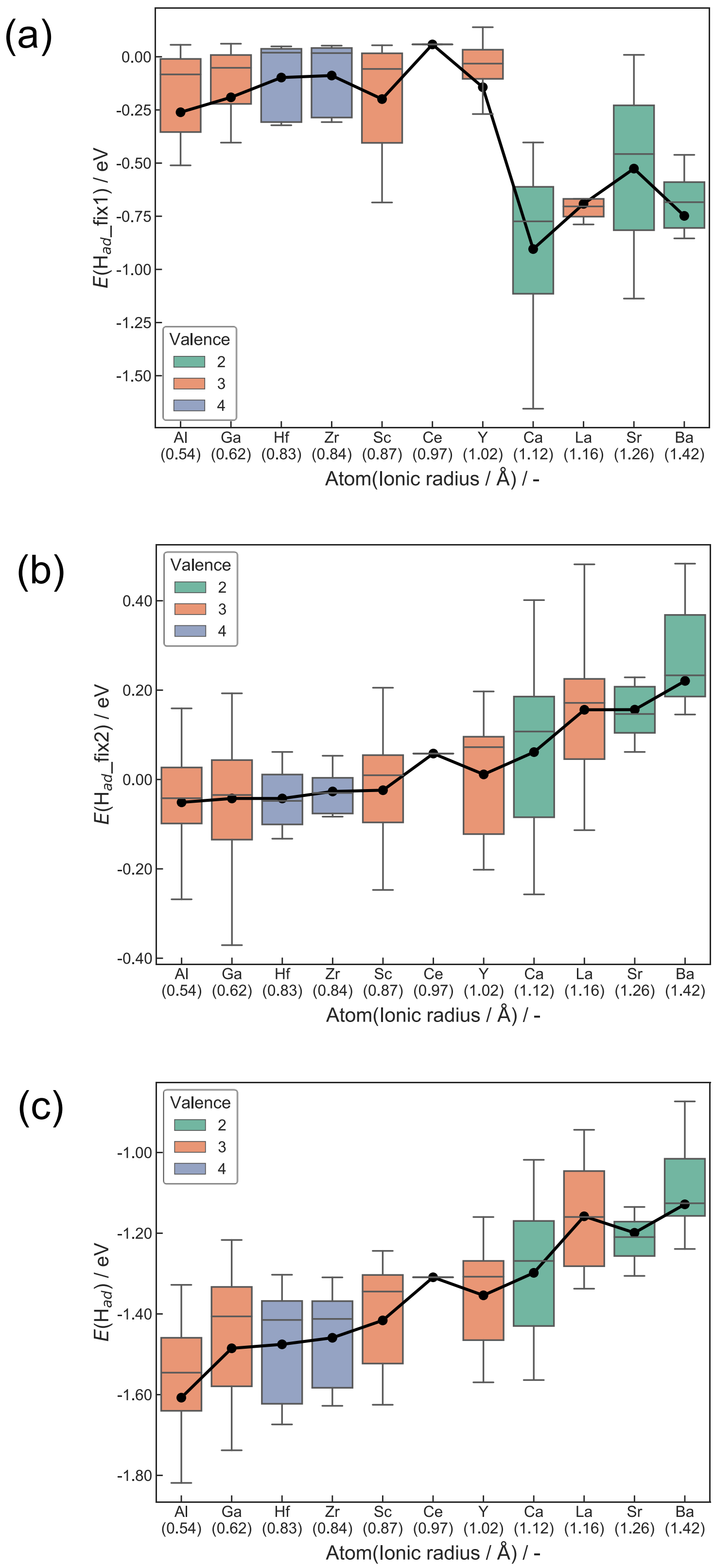

Figure 3.3. Box plots for the energies of H atom adsorption: (a) “Fix1 adsorption”, (b) “Fix2 adsorption”, and (c) “Relax adsorption”. Whisker length is limited to be 1.5 times of interquartile range. Black plots mean average values. Copyright 2021 RSC publishing.

3.3.3. Evaluation of OH amount using XPS

Heterocation-doping effects on O_{lat}-H^+ adsorption over CeO_2-based materials were confirmed using XPS measurements. Figures 3.4 and 3.5 present the O1*s* and C1*s* spectra of pre-reduced CeO_2 and $Ce_{0.9}M_{0.1}O_{2-\delta}$ (M: Sr, Al, Y, and Zr). The differentiated spectrum showed that the O1*s* and C1*s* spectra can be decomposed into two and three peaks. The peaks at around 528 and 530 eV in O 1*s* spectrum are assignable respectively to O_{lat} and O–H or C–O or O–C=O. [34–36] In addition, the peaks at around 285, 286, and 289 eV in C1*s* spectrum are derived respectively from C–C or C–H, C–O, and O–C=O. [34, 37] The OH ratio based on O_{lat} was calculated using the following equation.

$$\text{OH ratio} = \frac{(\text{Area of OH+C-O+O-C=O in O}1s\text{ spectra}) - \text{RSF}_{\text{O}1s}/\text{RSF}_{\text{C}1s}(\text{Area of C-O+O-C=O in C }1s\text{ spectra})}{(\text{Area of O}_{\text{lat}}\text{ in O}1s\text{ spectra})} \quad (3.2)$$

The relative sensitivity factor RSF_x (x = O1*s*, C1*s*) was confirmed by Ulvac-Phi Inc. for each measurement device. The calculated OH ratio describes the amount of O_{lat}-H^+ over CeO_2-based materials after reduction under H_2. A higher OH ratio represents strong binding of O_{lat}-H^+. Figure 3.6 represents the relation between the OH ratio obtained from XPS measurements and averages of DFT-obtained $E(H_{ad})$. Results confirmed clear correlation between DFT calculated values and experimental values. This strong correlation demonstrated the validity of the trend in the adsorption energy of hydrogen atoms suggested by DFT calculations.

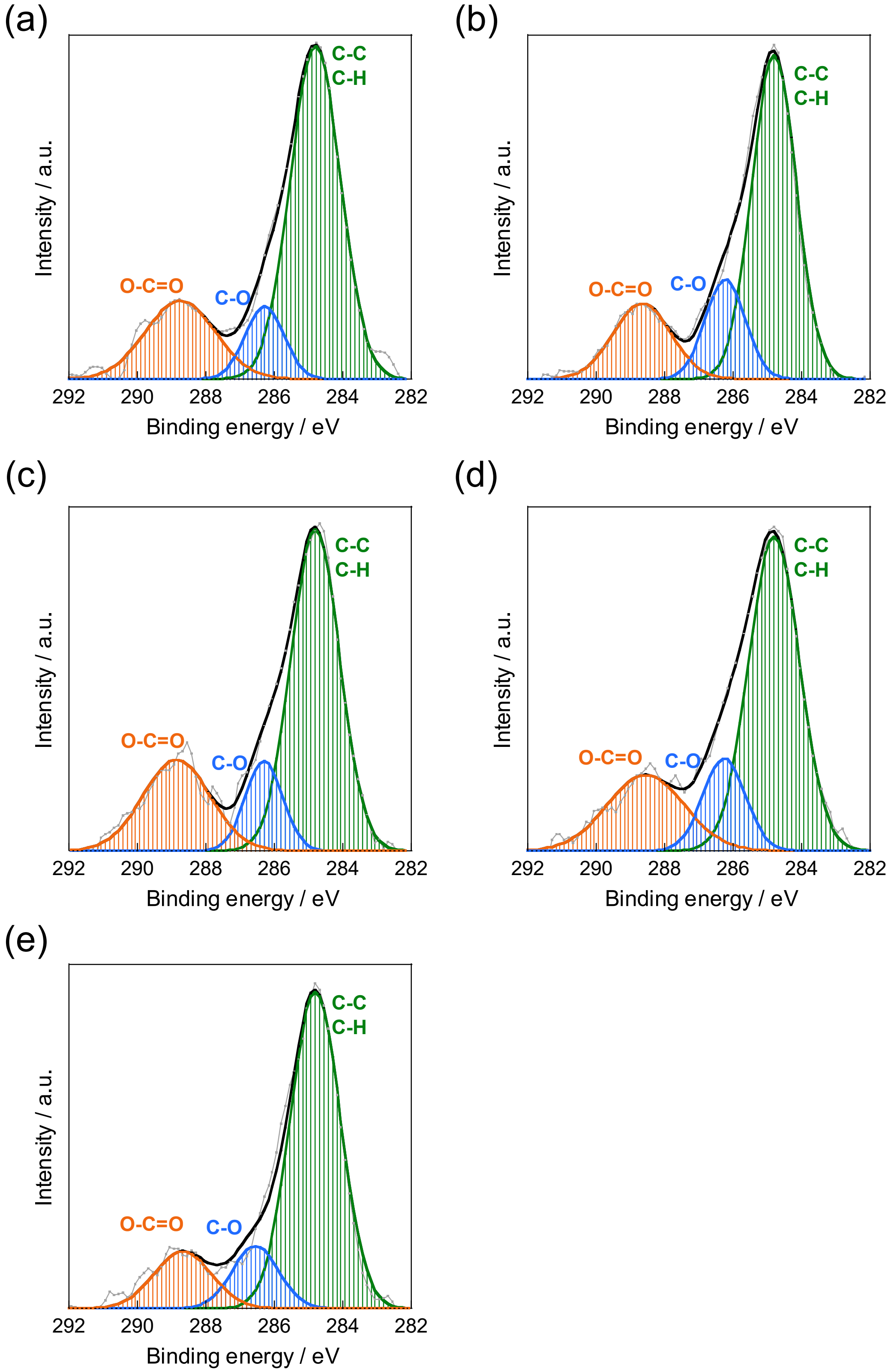

Figure 3.4. X-ray photoelectron spectra of C 1*s* after reduction under H_2 at 773 K for 1 h: (a) CeO_2, (b) $Ce_{0.9}Sr_{0.1}O_{2-\delta}$, (c) $Ce_{0.9}Al_{0.1}O_{2-\delta}$, (d) $Ce_{0.9}Y_{0.1}O_{2-\delta}$, and (e) $Ce_{0.9}Zr_{0.1}O_{2-\delta}$. Copyright 2021 RSC publishing.

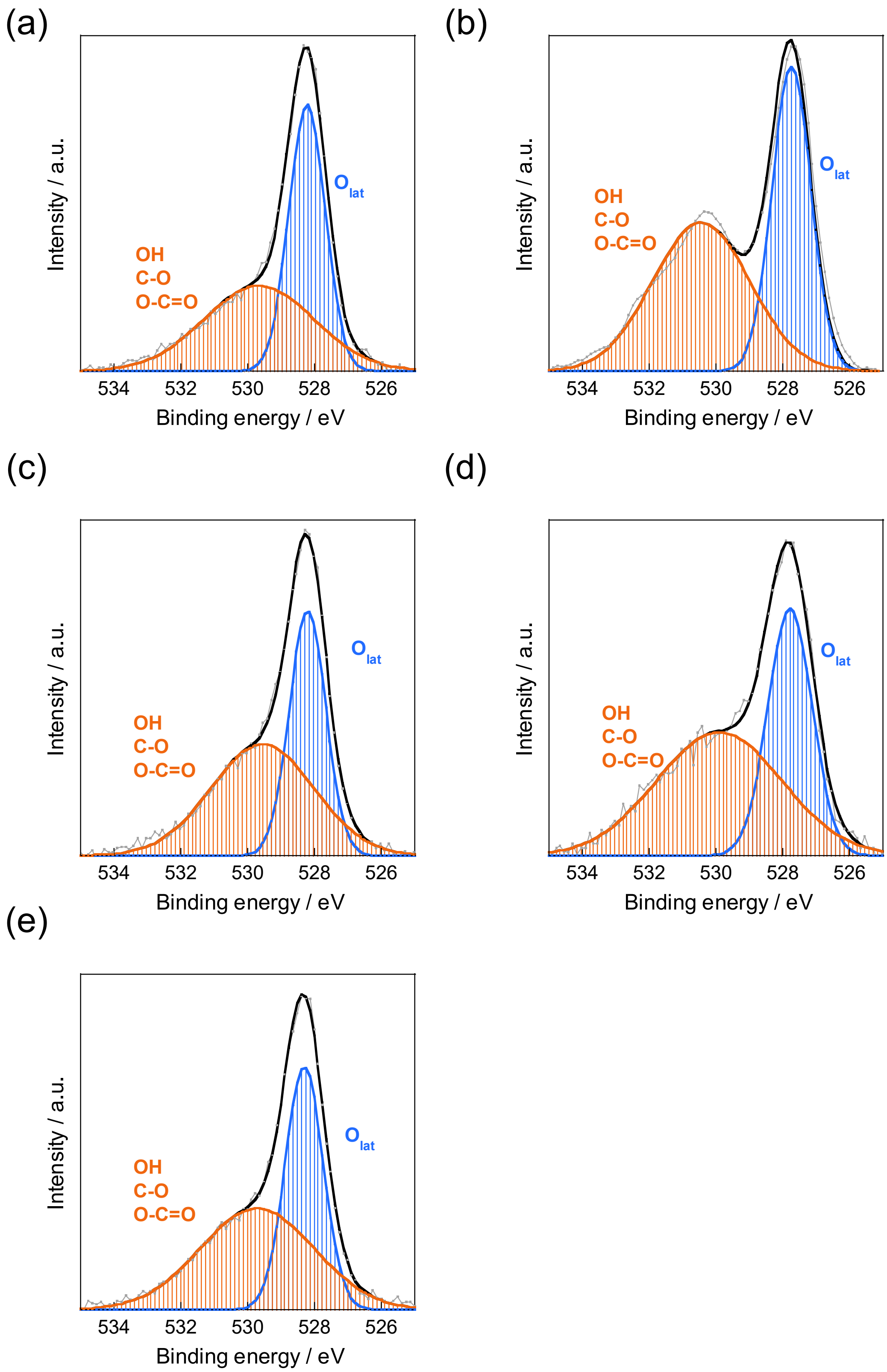

Figure 3.5. X-ray photoelectron spectra of O 1*s* after reduction under H_2 at 773 K for 1 h: (a) CeO_2, (b) $Ce_{0.9}Sr_{0.1}O_{2-\delta}$, (c) $Ce_{0.9}Al_{0.1}O_{2-\delta}$, (d) $Ce_{0.9}Y_{0.1}O_{2-\delta}$, and (e) $Ce_{0.9}Zr_{0.1}O_{2-\delta}$. Copyright 2021 RSC publishing.

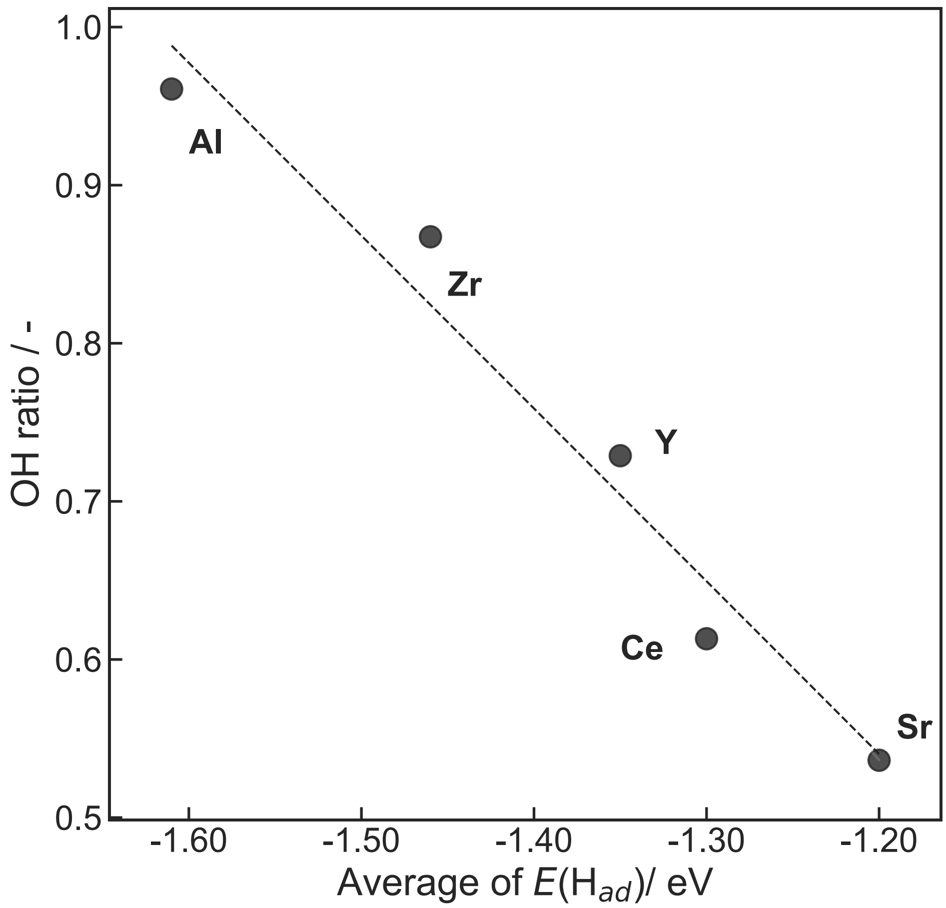

Figure 3.6. Correlation between OH ratio and average of DFT-calculated *E*(H ad). Copyright 2021 RSC publishing.

3.4. Chapter Conclusion

Heterocation-doping effects on H atom adsorption over CeO_2 were elucidated. We performed DFT calculations with multiple flows ("Fix 1 adsorption", "Fix 2 adsorption", and "Relax adsorption") and elucidated the separate influences of valence and ionic radius. The electron-depleted O_{lat} and the flexibility of the lattice play important roles for the strong adsorption of O_{lat}-H^+. Electron-depleted O_{lat} can be formed by doping of heterocations with lower valences and smaller ionic radii. Additionally, doping with smaller heterocations induced high flexibility of CeO_2 matrix. The DFT suggestion was confirmed from XPS measurements. Results experimentally elucidated that O_{lat}-H^+ strongly adsorbed over surfaces doped with heterocations that have lower valence and a smaller ionic radius.

References

1. K. Murakami and Y. Sekine, Recent Progress in use and observation of surface hydrogen migration over metal oxides, *Phys. Chem. Chem. Phys.*, 2020, **22**, 22852 – 22863.
2. H. Saito, H. Sekin, Y. Hosono, T. Higo, J. G. Seo, S. Maeda, K. Hashimoto, S. Ogo, and Y. Sekine, Dehydrogenation of Ethane via Mars–Van Krevelen Mechanism over $La_{0.8}Ba_{0.2}MnO_{3-\delta}$ Perovskite Under Anaerobic Conditions, *J. Phys. Chem. C*, 2019, **123(43)**, 26272 – 2681.
3. T. Higo, K. Ueno, Y. Omori, H. Tsuchiya, S. Ogo, S. Hirose, H. Mikami, and Y. Sekine, Perovskite lattice oxygen contributes to low-temperature catalysis for exhaust gas cleaning, *RSC Adv.*, 2019, **39**, 22721 – 22728.
4. D. Mukai, S. Tochiya, Y. Murai, M. Imori, T. Hashimoto, Y. Sugiura, and Y. Sekine, Role of support lattice oxygen on steam reforming of toluene for hydrogen production over Ni/$La_{0.7}Sr_{0.3}AlO_{3-\delta}$ catalyst, *Appl. Catal. A*, 2013, **453**, 60 – 70.
5. Y. Sekine, D. Mukai, Y. Murai, S. Tochiya, Y. Izutsu, K. Sugiura, N. Hosomura, H. Arai, E. Kikuchi, and Y. Sugiura, Steam reforming of toluene over perovskite-supported Ni catalysts, *Appl. Catal. A*, 2013, **451**, 160 – 167.
6. G. Dutta, U. V. Waghmare, T. Baidya, M. S. Hegde, K. R. Priolkar, and P. R. Sarode, Origin of Enhanced Reducibility/Oxygen Storage Capacity of $Ce_{1-x}Ti_xO_2$ Compared to CeO_2 or TiO_2, *Chem. Matter.*, 2006, **18(14)**, 3249 – 3256.
7. Y. Q. Su, I. A. W. Filot, J. X. Liu, and E. J. M. Hensen, Stable Pd-Doped Ceria Structures for CH_4 Activation and CO Oxidation, *ACS Catal.*, 2018, **8(1)**, 75 – 80.
8. W. Yang, C. Li, H. Wang, X. Li, W. Zhang, and H. Li, Cobalt doped ceria for abundant storage of surface active oxygen and efficient elemental mercury oxidation in coal combustion flue gas, *Appl. Catal. B*, 2018, **239**, 233 – 244.
9. Y. Tang, H. Zhang, L. Cui, C. Ouyang, S. Shi, W. Tang, H. Li, J. S. Lee, and L. Chen, First-principles investigation on redox properties of M-doped CeO_2 (M=Mn,Pr,Sn,Zr), *Phys. Rev. B*, 2010, **82**, 125104.
10. D. A. Andersson, S. I. Simak, N. V. Skorodumova, I. A. Abrikosov, and B. Johansson, Theoretical study of CeO_2 doped with tetravalent ions, *Phys. Rev. B*, 2007, **76**, 174119.
11. K. Toko, K. Ito, H. Saito, Y. Hosono, K. Murakami, S. Misaki, T. Higo, S. Ogo, H. Tsuneki, S. Maeda, K. Hashimoto, H. Nakai, and Y. Sekine, Catalytic Dehydrogenation of Ethane over Doped Perovskite via the Mars–Van Krevelen Mechanism, *J. Phys. Chem. C*, 2020, **124(19)**, 10462 – 10469.
12. W. Zhang, M. Pu and M. Lei, Theoretical Studies on the Stability and Reactivity of the Metal-Doped CeO_2(100) Surface: Toward H_2 Dissociation and Oxygen Vacancy Formation, *Langmuir*, 2020, **36**, 5891 – 5901.
13. M. D. Krcha, A. D. Mayernick, and M. J. Janik, Periodic trends of oxygen vacancy formation and C-H bond activation over transition metal-doped CeO_2 (1 1 1) surfaces, *J. Catal.*, 2012, **293**, 103 – 115.

14. G. Kresse and J. Hafner, *Ab initio* molecular dynamics for liquid metals, *Phys. Rev. B*, 1993, **47**, 558 – 561.
15. G. Kresse and J. Hafner, *Ab initio* molecular-dynamics simulation of the liquid-metal–amorphous-semiconductor transition in germanium, *Phys. Rev. B*, 1994, **49**, 14251 – 14269.
16. G. Kresse, J. Furthmüller, Efficiency of ab-initio total energy calculations for metals and semiconductors using a plane-wave basis set, *Comput. Mat. Sci.*, 1996, **6(1)**, 15 – 50.
17. G. Kresse, J. Furthmüller, Efficient iterative schemes for *ab initio* total-energy calculations using a plane-wave basis set, *Phys. Rev. B*, 1996, **54**, 11169 – 11186.
18. J. P. Perdew, K. Burke, and M. Ernzerhof, Generalized Gradient Approximation Made Simple, *Phys. Rev. Lett.*, 1996, **77**, 3865 – 3868.
19. H. J. Monkhorst and J. D. Pack, Special points for Brillouin-zone integrations, *Phys. Rev. B*, 1976, **13**, 5188 – 5192.
20. S. Grimme, J. Antony, S. Ehrlich, and S. Krieg, A consistent and accurate *ab initio* parametrization of density functional dispersion correction (DFT-D) for the 94 elements H-Pu, *J. Chem. Phys.*, 2010, **132**, 154104.
21. H. T. Chen and J. G. Chang, Oxygen vacancy formation and migration in Ce1−*x*Zr*x*O2 catalyst: A DFT+U calculation, *J. Chem. Phys.*, 2010, **132**, 214702.
22. M. Nolan, Healing of oxygen vacancies on reduced surfaces of gold-doped ceria, *J. Chem. Phys.*, 2009, **130**, 144702.
23. M. Nolan, Enhanced oxygen vacancy formation in ceria (111) and (110) surfaces doped with divalent cations, *J. Mater. Chem.*, 2011, **21**, 9160 – 9168.
24. M. Nolan, Charge Compensation and Ce^{3+} Formation in Trivalent Doping of the CeO_2(110) Surface: The Key Role of Dopant Ionic Radius, *J. Phys. Chem. C*, 2011, **115**, 6671 – 6681.
25. Z. X. Yang, G. X. Luo, Z. S. Lu, and K. Hermansson, Oxygen vacancy formation energy in Pd-doped ceria: A DFT+U study, *J. Chem. Phys.*, 2007, **127**, 074704.
26. A. D. Mayernick, and M. J. Janik, Methane Activation and Oxygen Vacancy Formation over CeO_2 and Zr, Pd Substituted CeO_2 Surfaces, *J. Phys. Chem. C*, 2008, **112(38)**, 14955 – 14964.
27. M. B. Watkins, A. S. Foster, and A. L. Shluger, Hydrogen Cycle on CeO_2 (111) Surfaces: Density Functional Theory Calculations, *J. Phys. Chem. C*, 2007, **111(42)**, 15337 – 15341.
28. D. A. Shirley, High-Resolution X-Ray Photoemission Spectrum of the Valence Bands of Gold, *Phys. Rev. B*, 1972, **5(12)**, 4709.
29. A. Proctor and P. M. A. Sherwood, Data analysis techniques in x-ray photoelectron spectroscopy, *Anal. Chem.*, 1982, **54(1)**, 13–19.
30. M. G. Melchor and N. López, Homolytic Products from Heterolytic Paths in H_2 Dissociation on Metal Oxides: The Example of CeO_2, *J. Phys. Chem. C*, 2014, **118**, 10921–10926.
31. Z. Hu, B. Li, X. Y. Sun, and H. Metiu, Chemistry of Doped Oxides: The Activation of Surface Oxygen and the Chemical Compensation Effect, *J. Phys. Chem. C*, 2011, **115**, 3065 – 3074.
32. E. W. McFarland, and H. Metiu, Catalysis by Doped Oxides, *Chem. Rev.*, 2013, **113**, 4391 – 4427.

33. H. -Y. Li, H. -F. Wang, X. -Q. Gong, Y. -L. Guo, Y. Guo, G. Lu and P. Hu, Multiple configurations of the two excess 4*f* electrons on defective CeO_2 (111):Origin and implications, *Phys*. *Rev*. *B*, 2009, **79**, 193401.
34. E. McCafferty and J. P. Wightman, Determination of the concentration of surface hydroxy groups on metal oxide films by a quantitative XPS method, *Surf. Interface Anal*., 1998, **26**, 549–564.
35. J. T. Newberg, D. E. Starr, S. Yamamoto, S. Kaya, T. Kendelewicz, E. R. Mysak, S. Porsgaard, M. B. Salmeron, G. E. Brown Jr., A. Nilsson and H. Bluhm, Formation of hydroxy and water layers on MgO films studied with ambient pressure XPS, *Surf. Sci.*, 2011, **605**, 89–94.
36. G. P. López, D. G. Castner and B. D. Ratner, XPS O 1s binding energies for polymers containing hydroxy, ether, ketone and ester groups, *Surf. Interface Anal.*, 1991, **17**, 267–272.
37. M. Mantel and J. P. Wightman, Influence of the surface chemistry on the wettability of stainless steel, *Surf. Interface Anal*., 1994, **21**, 595–605.

Appendix of Chapter 3

A.3.1. Bader charge analysis of O_{lat}

Bader charge analysis [1-4] was performed for investing the heterocation-doping effects on electronic state of O_{lat}. "Fix surface" and "Relax surface" were used as calculation models. The heterocation-doping effect is different between the O_{lat} coordinated to the dopants and the other O_{lat} as shown in the former chapter. Therefore, the obtained Bader charges were divided into the charges of the surface O_{lat} coordinated only to Ce (Figure A.3.4) and the charge of the surface O_{lat} coordinated to the dopant (Figure A.3.5). As for surface O_{lat} coordinated to only Ce, doping with lower valent heterocations induced the decrease in the Bader charge of O_{lat} as for "Fix surface", see Figure A.3.4 (a). This decrement suggests the formation of Lewis acid sites by doping of lower valent heterocations. The Lewis acidity becomes pronounced along with the increase in the ionic radius of heterocations. This is caused by the high dispersion of heterocations with larger ionic radius. Some of the Lewis acid sites were supplied electron by lattice relaxation (Figure A.3.4 (b)). The difference in charge between the "Relax surface" and "Fix surface" is presented in Figure A.3.4 (c). The charge transfer became large as the ionic radius of heterocations increased. This is because larger heterocation-doping makes the surrounding Ce-O bonds to contract as shown Figure A.3.3. When O_{lat} was next to dopants, the surface doped with Al, Ga, and Y exhibited a quite different trend from that of the O_{lat} coordinated only to Ce (Figure A.3.5). It suggests that the electronic state of O_{lat} changes significantly when two dopants are adjacent to each other. Comparing Figure 3.2 and Figure A.3.2, the coordination status of O_{lat} around dopants changed significantly as the ionic radius of the heterocations became small remarkably. Hence, significant electron transfer was confirmed for doping of heterocations with small ionic radii (Figure A.3.5 (c)). The obtained Bader charges of all outermost O_{lat} were also summarized in Figure A.3.6. The change of oxygen Bader charge by heterocation-doping were drawn in Figures A.3.7-A.3.9. Only outermost oxygen was drawn as balls. The transparent triangles stand for the planes including O_{lat} and outermost cations. The color of balls means the difference of Bader charge by heterocation doping using the charge of CeO_2 as a reference. Red sites show the electron rich oxygen, and blue sites stand for the electron deficient oxygen. The limit of color scale was set to be ± 0.1 e for increasing the color contrast. When two heterocations are placed next to each other, the electronic state changes significantly even after lattice relaxation as shown in color maps. Results suggest that the distribution of dopants affects the electronic state of O_{lat}.

A.3.2. Reducible heterocation-doping effects

The role of reducibility in heterocation-doping effects was studied using Ti as a model dopant. DFT calculations were performed in the same way as shown in part 3.3.1. Figure A.3.5. portrays the optimized surface ("Relax surface"). The calculated results were inserted in Figure

3.3 as shown in Figure A.3.6. Doping with Ti significantly facilitated the adsorption of O_{lat}-H^+. In particular, the strongest adsorption of H atom was confirmed on surfaces doped with Ti regarding “Fix2 adsorption”. Ti^{4+} is known to be reduced into Ti^{3+} easily. Therefore, it was suggested that Ti^{4+} functioned as an electron reservoir and strongly promoted O_{lat} - H^+ adsorption.

References

1. W. Tang, E. Sanville, and G. Hnkelman, A grid-based Bader analysis algorithm without lattice bias, *J. Phys. Condes. Matter.*, 2009, **21**, 084204.
2. E. Sanville, S. D. Kenny, R. Smith, and G. Henkelman, Valence bond theory for chemical dynamics, *J. Comp. Chem.*, 2007, **28**, 899 – 908.
3. G. Henkelman, A. Arnaldsson, and H. Jónsson, A fast and robust algorithm for Bader decomposition of charge density, *Comut. Mater. Sci.*, 2006, **36**, 354 – 360.
4. M. Yu, and D. R. Trinkle, Accurate and efficient algorithm for Bader charge integration, *J. Chem. Phys.*, 2011, **134**, 064111.

Figures and Tables

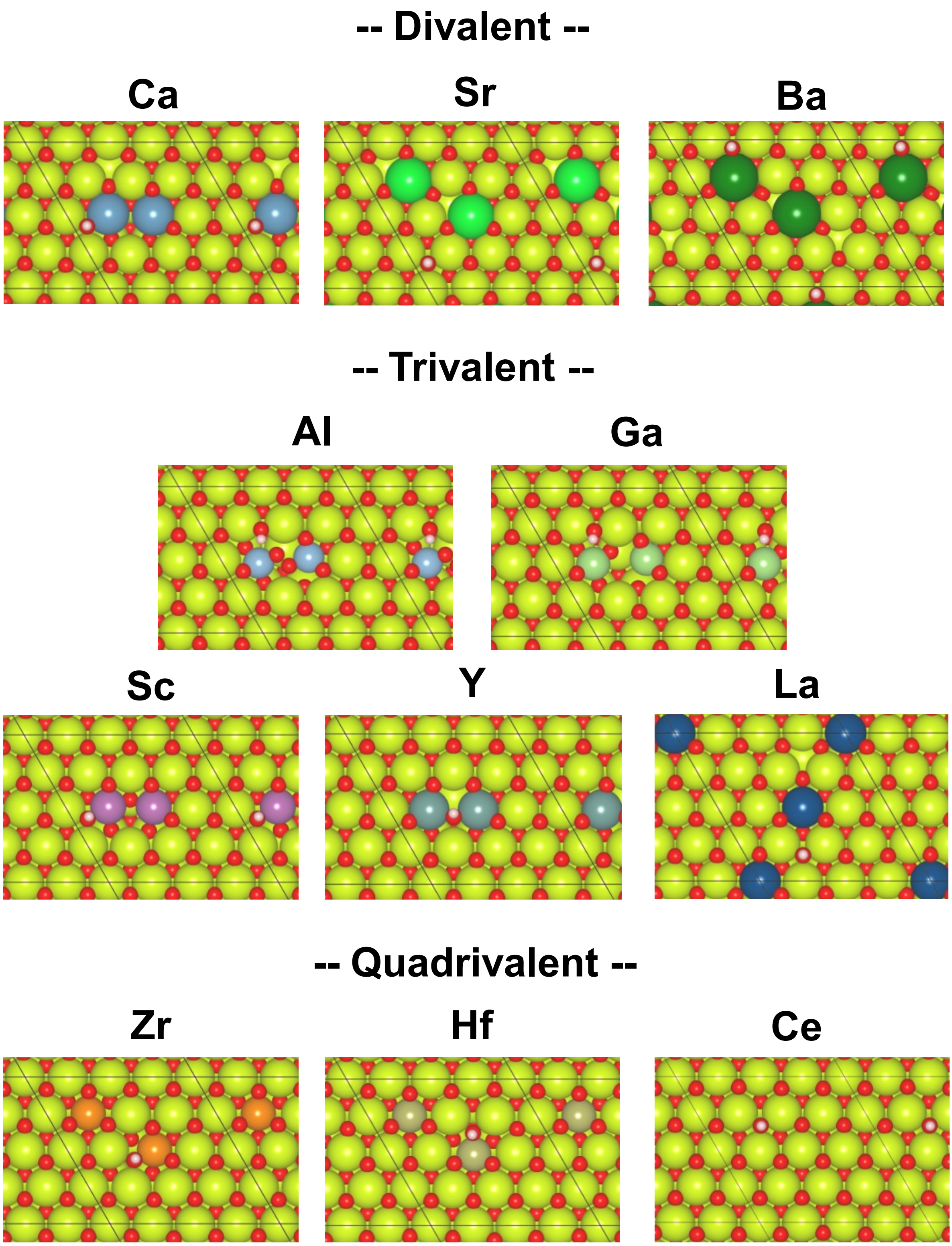

Figure A.3.1. DFT-optimized structures of $Ce_xM_{1-x}O_{2-\delta}$ (111) with H atom ("Relax adsorption" in Figure 3.1). Yellow ball means Ce, red stands for O, pink is H, and other colors show heterocations. Copyright 2021 RSC publishing.

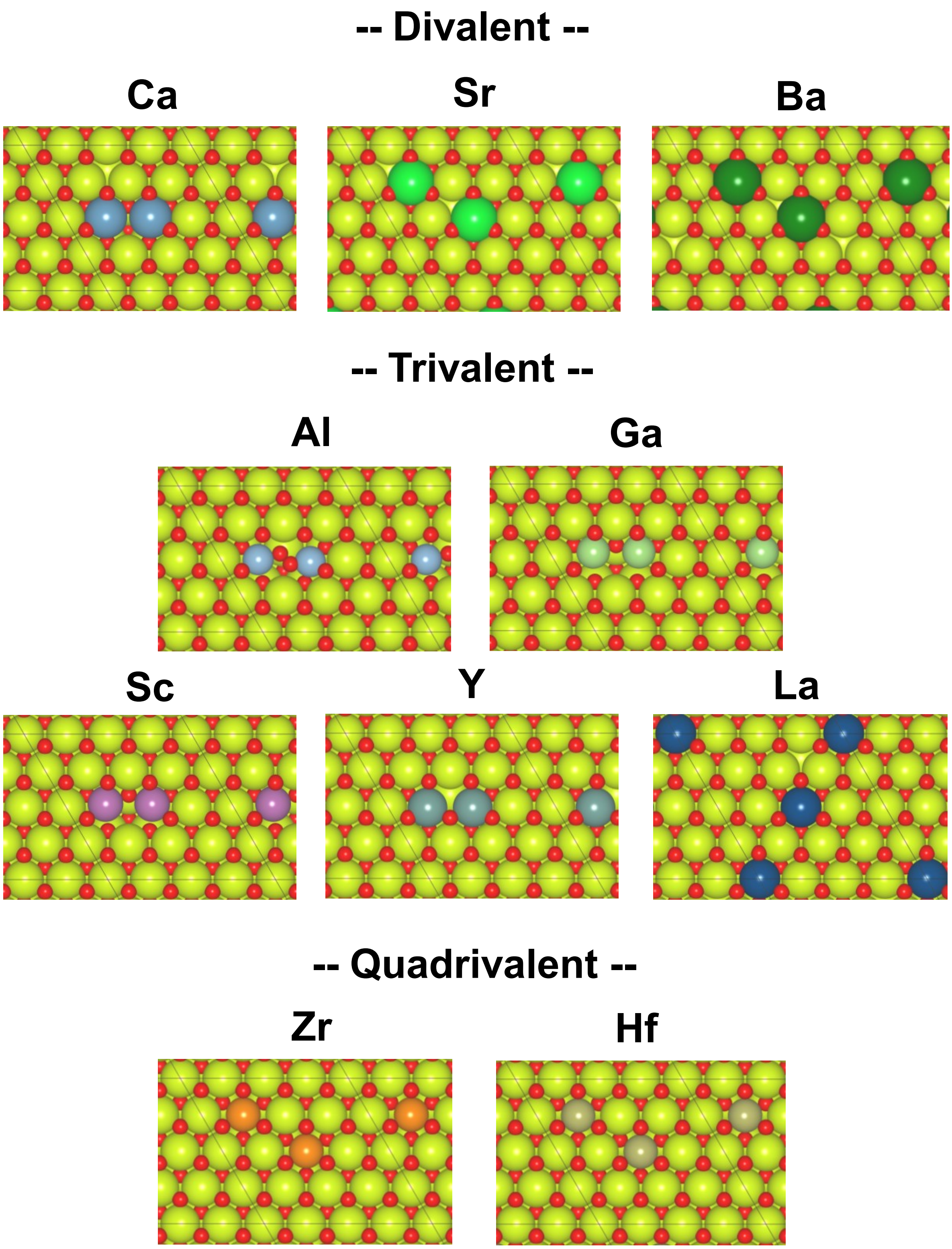

Figure A.3.2. DFT-optimized structures of $Ce_xM_{1-x}O_{2-\delta}$ (111) with O_{vac} for charge compensation ("Fix surface" in Figure 3.1). Yellow ball means Ce, red stands for O, and other colors show heterocations. Copyright 2021 RSC publishing.

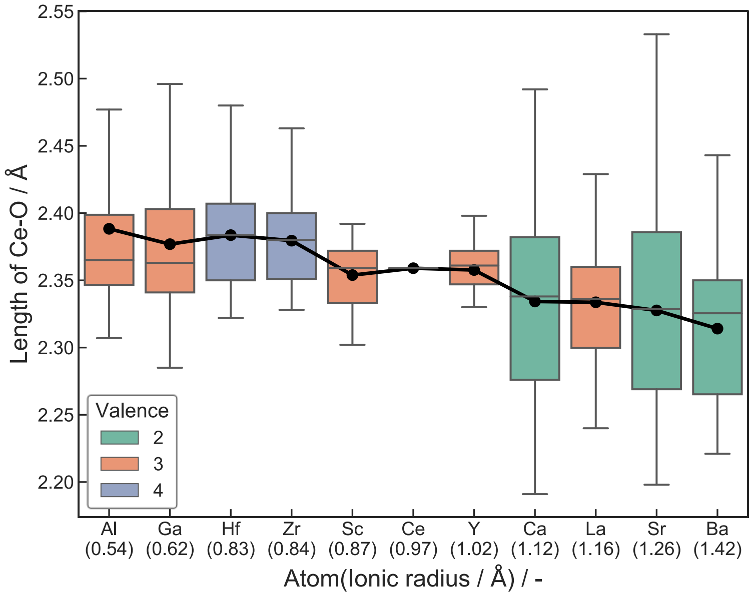

Figure A.3.3. Box plots for the Ce-O length at the outermost surface of "Relax surface". Whisker length is limited to be 1.5 times of interquartile range. Black plots mean average values. Copyright 2021 RSC publishing.

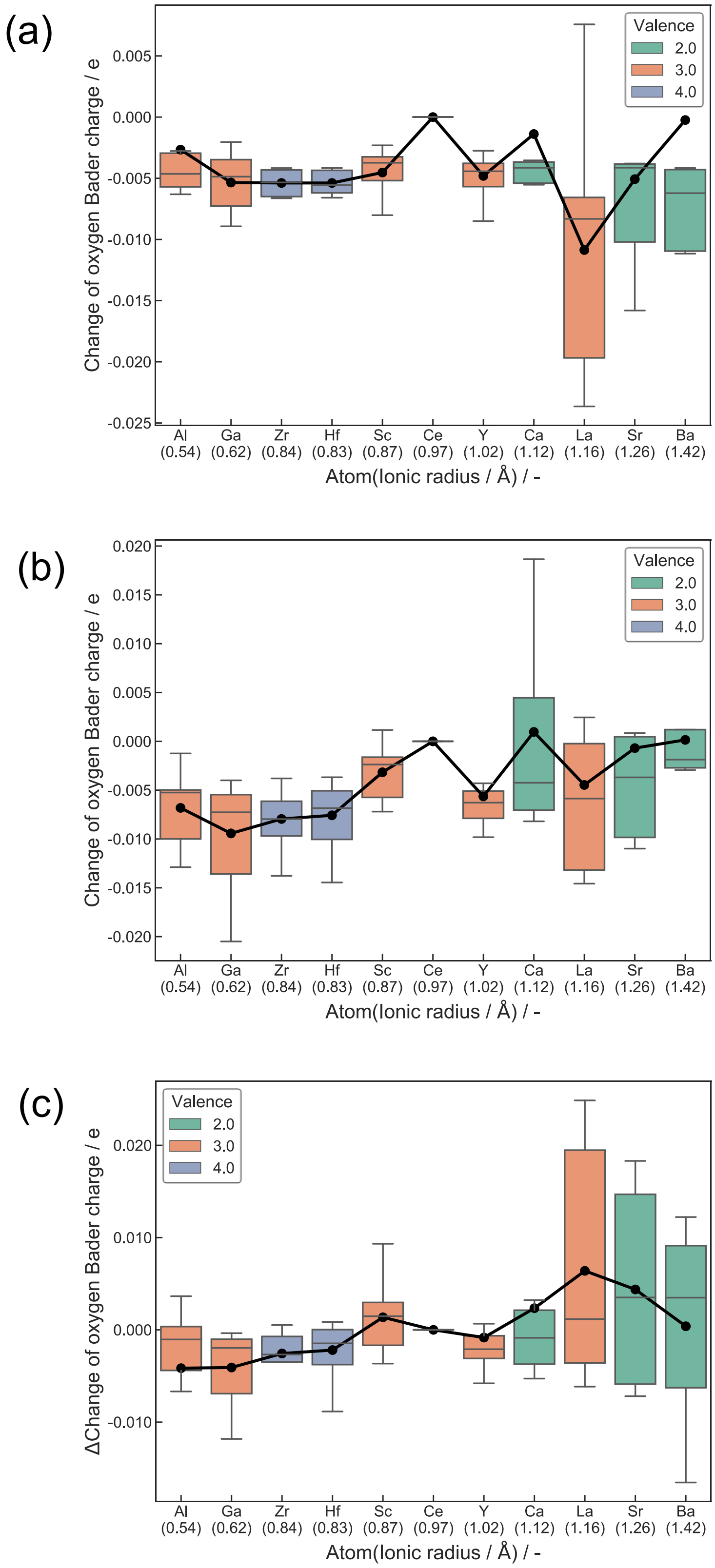

Figure A.3.4. Box plots for the difference in Bader charges of outermost surface O_{lat} next to only Ce. The charge of CeO_2 (111) was used as a reference value. (a) "Fix surface", (b) "Relax surface", and (c) difference between "Relax surface" and "Fix surface". Whisker length is limited to be 1.5 times of interquartile range. Black plots mean average values. Copyright 2021 RSC publishing.

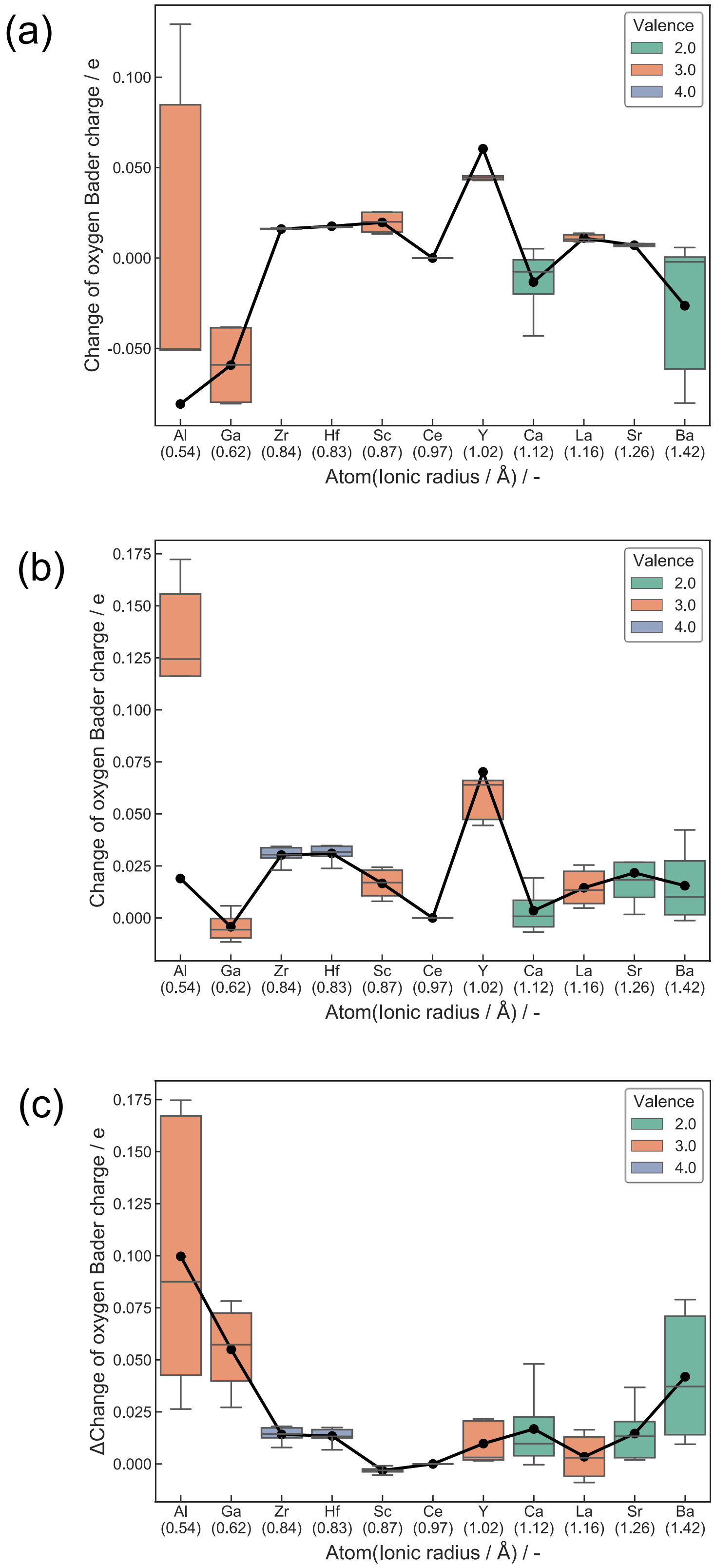

Figure A.3.5. Box plots for the difference in Bader charges of outermost surface O_{lat} next to dopants. The charge of CeO_2 (111) was used as a reference value. (a) “Fix surface”, (b) “Relax surface”, and (c) difference between “Relax surface” and “Fix surface”. Whisker length is limited to be 1.5 times of interquartile range. Black plots mean average values. Copyright 2021 RSC publishing.

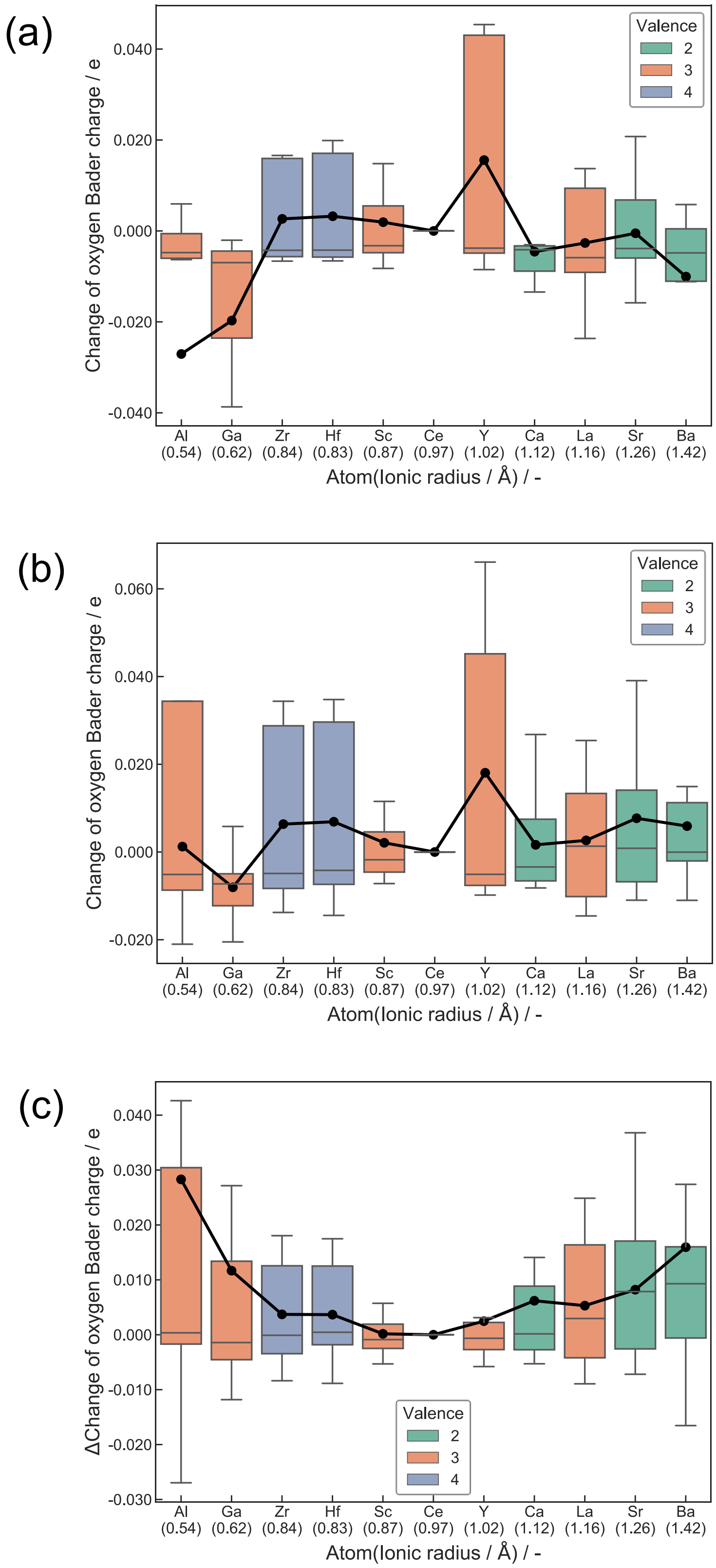

Figure A.3.6. Box plots for the difference in Bader charges of all outermost surface O_{lat}. The charge of CeO_2 (111) was used as a reference value. (a) “Fix surface”, (b) “Relax surface”, and (c) difference between “Relax surface” and “Fix surface”. Whisker length is limited to be 1.5 times of interquartile range. Black plots mean average values. Copyright 2021 RSC publishing.

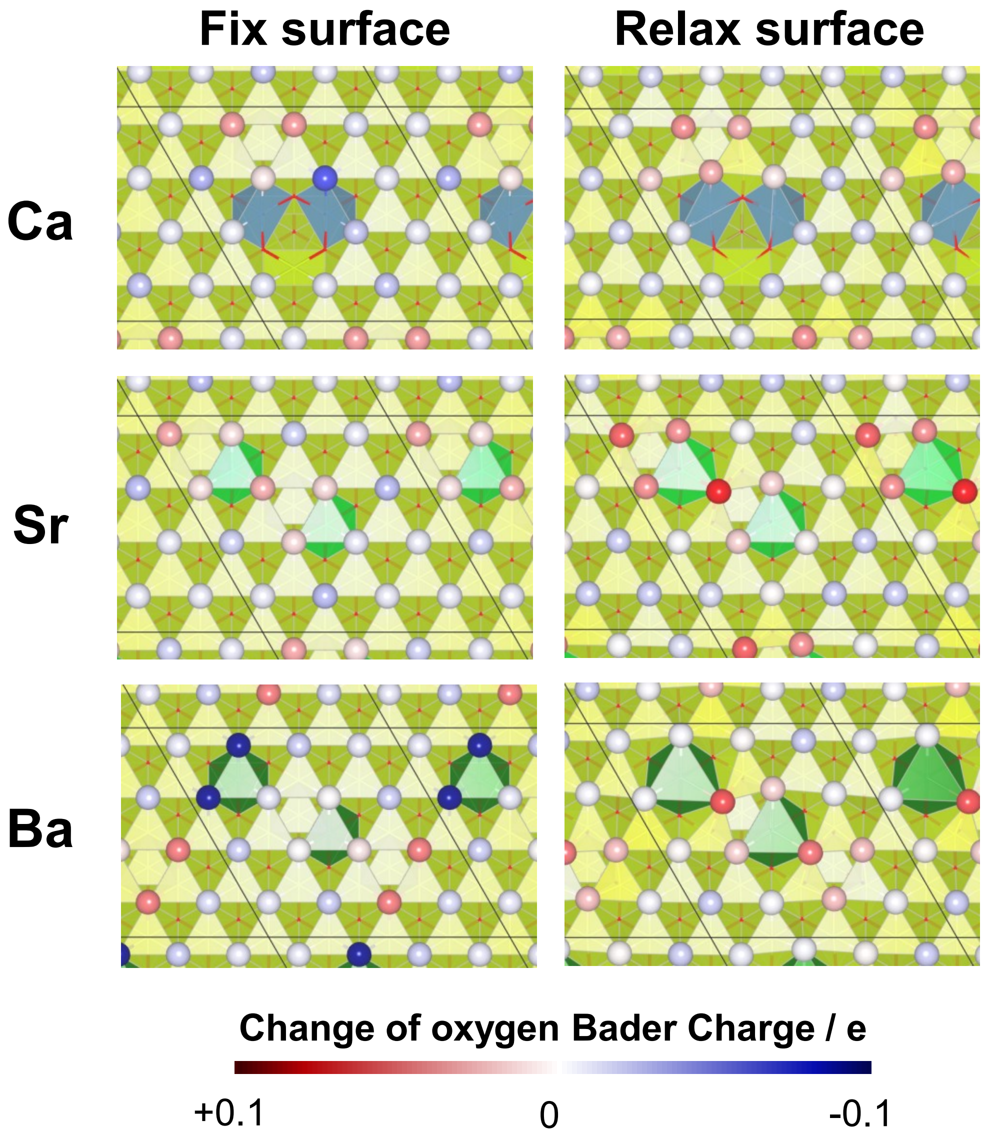

Figure A.3.7. Color maps for change of outermost oxygen charge by divalent heterocation-doping using CeO_2 (111) as a reference value. Left panel shows data of "Fix surface", and right panel is "Relax surface". Red balls indicate the electron rich oxygen, and blue balls show the electron deficient oxygen. Copyright 2021 RSC publishing.

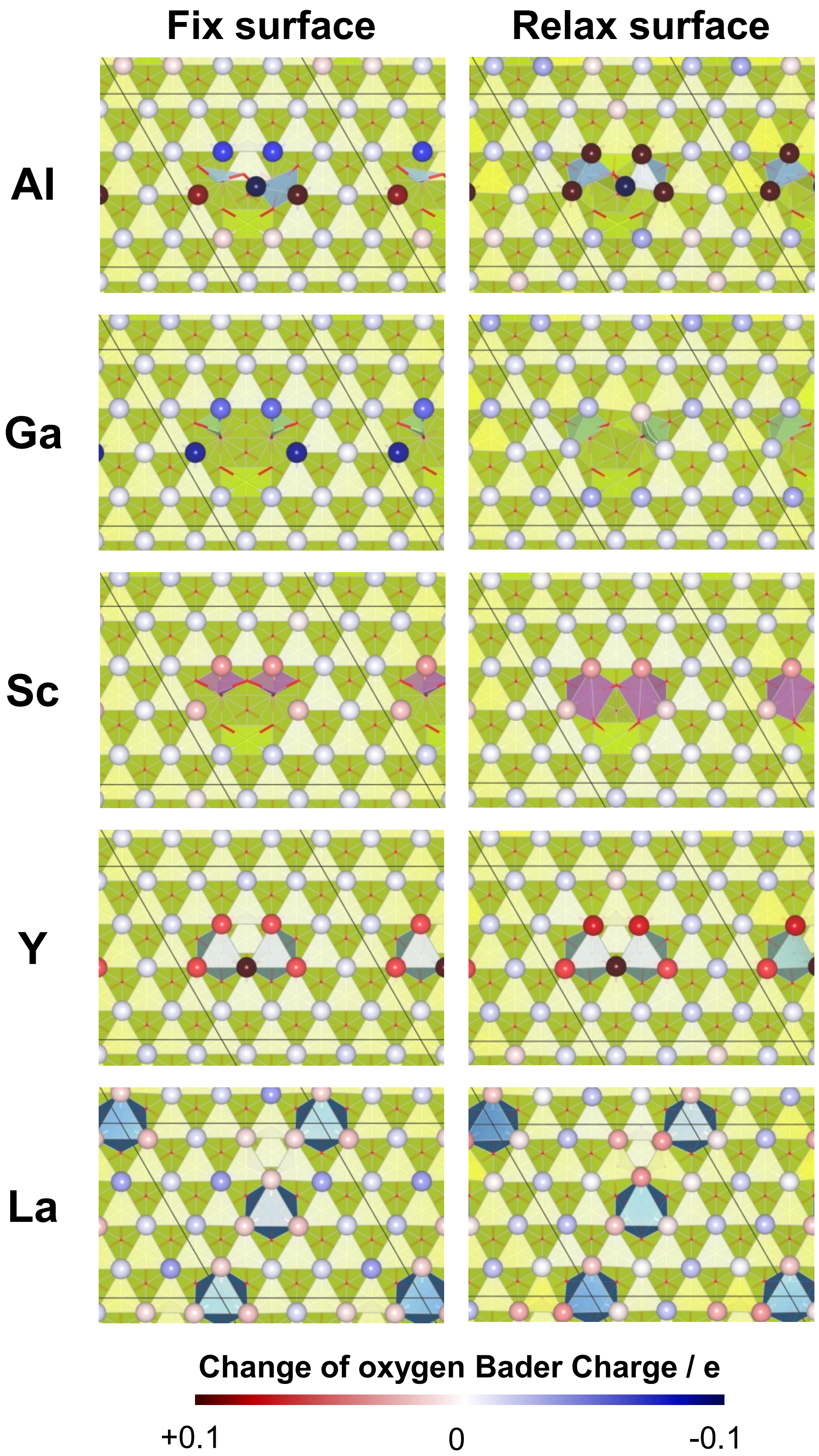

Figure A.3.8. Color maps for change of outermost oxygen charge by trivalent heterocation-doping using CeO_2 (111) as a reference value. Left panel shows data of "Fix surface", and right panel is "Relax surface". Red balls indicate the electron rich oxygen, and blue balls show the electron deficient oxygen. Copyright 2021 RSC publishing.

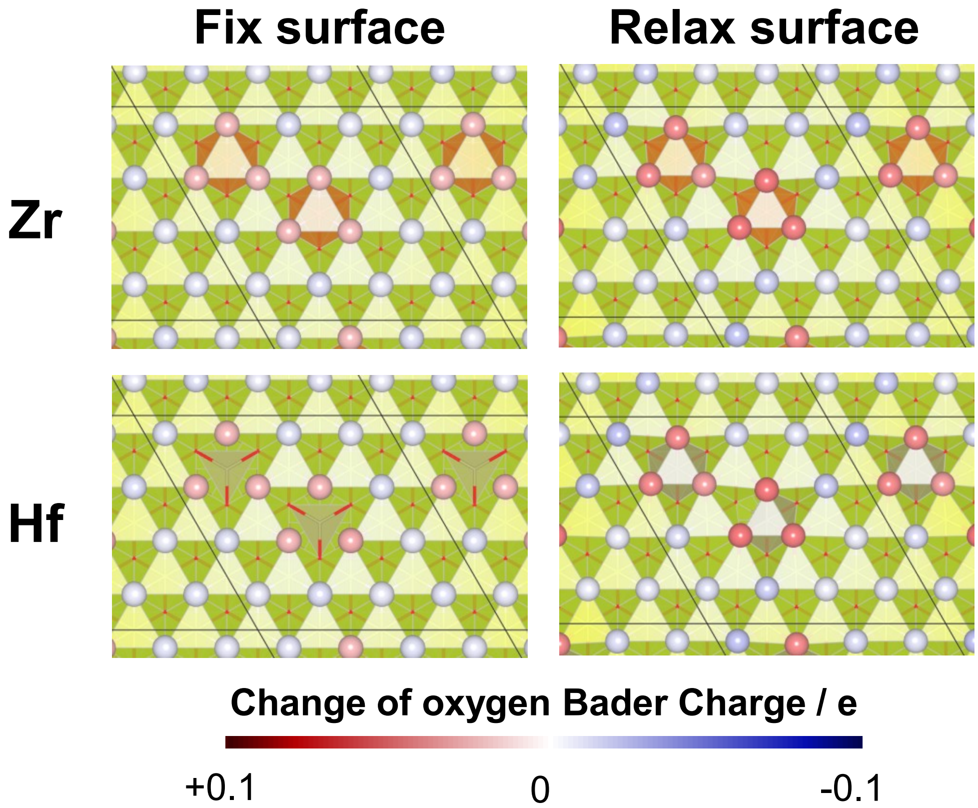

Figure A.3.9. Color maps for change of outermost oxygen charge by quadrivalent heterocation-doping using CeO_2 (111) as a reference value. Left panel shows data of "Fix surface", and right panel is "Relax surface". Red balls indicate the electron rich oxygen, and blue balls show the electron deficient oxygen. Copyright 2021 RSC publishing.

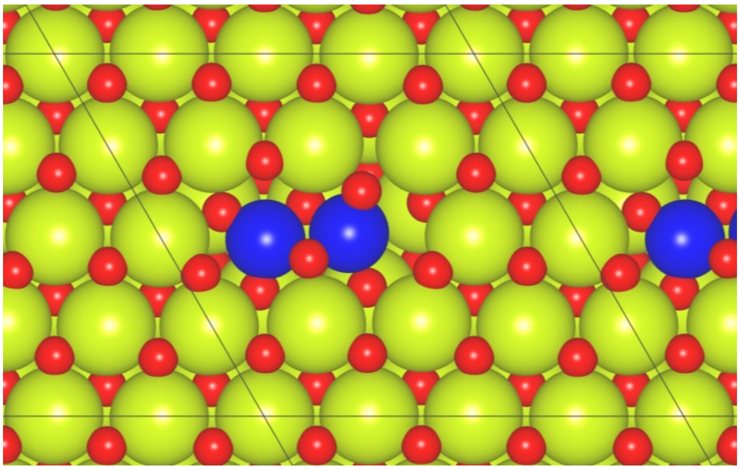

Figure A.3.10. Top view of CeO_2 (111) doped with Ti. Yellow ball means Ce, red stands for O, and blue shows Ti. Copyright 2021 RSC publishing.

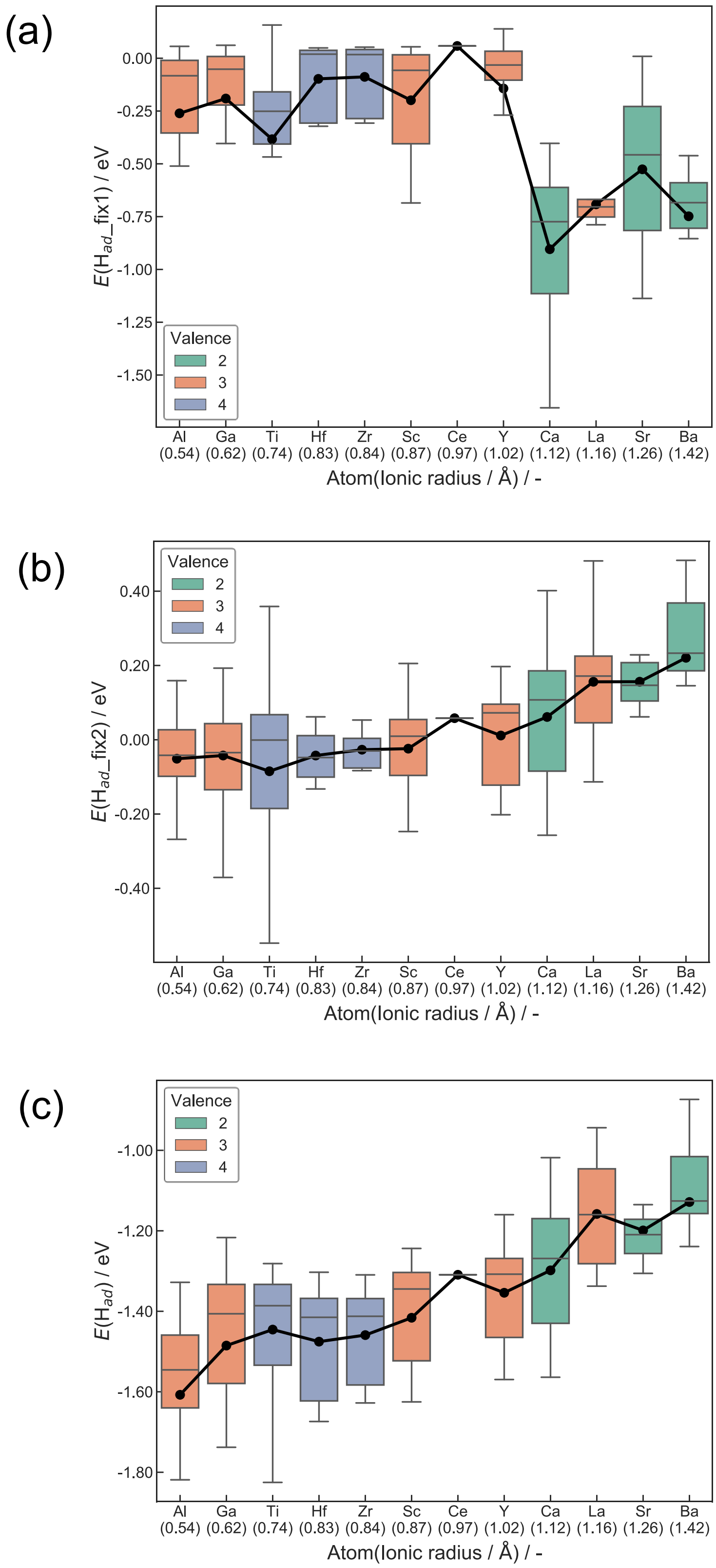

Figure A.3.11. Box plots for the energies of H atom adsorption including data of Ti: (a) "Fix1 adsorption", (b) "Fix2 adsorption", and (c) "Relax adsorption". Whisker length is limited to be 1.5 times of interquartile range. Black plots mean average values. Copyright 2021 RSC publishing.

Table A.3.1. Valence configurations used for DFT calculations. Copyright 2021 RSC publishing.

Atom /-	Valence configuration / -
Ca	$4s^2$
Sr	$5s^2$
Ba	$6s^2$
Al	$3s^2 3p^1$
Ga	$3d^{10} 4s^2 4p^1$
Sc	$3d^1 4s^2$
Y	$4d^1 5s^2$
La	$5s^2 5p^6 5d^1 6s^2$
Ti	$3d^2 4s^2$
Zr	$4s^2 4p^6 4d^2 5s^2$
Hf	$5p^6 5d^2 6s^2$
Ce	$4f^1 5s^2 5p^6 5d^1 6s^2$
O	$1s^2 2s^2 2p^5$
H	$1s^1$

Table A.3.2. Oxygen vacancy (O_{vac}) formation energy ($E(O_{vac})$) over $Ce_{1-x}M_xO_{2-\delta}$ (111). Copyright 2021 RSC publishing.

Dopant / -	n / -	$E(O_{vac})$ / eV
Pristine	1	2.98
Ca	1	-0.80
	2	-1.41
	3	0.83
Sr	1	-0.66
	2	-1.23
	3	1.25
Ba	1	-0.71
	2	-0.61
	3	2.49
Al	1	0.59
Ga	1	-0.63
	2	0.08
Sc	1	-0.95
	2	0.76
Y	1	-0.72
	2	2.36
La	1	-0.67
	2	2.59
Ti	1	0.42
Zr	1	1.92
Hf	1	1.68

Chapter 4 OH Amount Effects on NH_3 Synthesis in the Electric Field

The content in this chapter is partly reproduced from K. Murakami, Y. Tanaka, R. Sakai, Y. Hisai, S. Hayashi, Y. Mizutani, T. Higo, S. Ogo, J. G. Seo, H. Tsuneki, and Y. Sekine, Key factor for the anti-Arrhenius low-temperature heterogeneous catalysis induced by H^+ migration: H^+ coverage over support, *Chem*. *Commun*., 2020, **56**, 3365-3368. Copyright RSC Publishing.

4.1. Introduction

Over the past several decades, industrial catalytic processes have evolved for large-scale plants. They are functioning efficiently under harsh conditions (high-temperatures and pressures) because of various facilities including heat exchangers. By contrast, next-generation catalytic processes must work under milder conditions to manage on-site and on-demand operation. Therefore, moderation of catalyst working conditions using external stimuli (*e.g.* photonic, magnetic, and electric fields) has been a central subject in the field of catalysis. [1–7] Our group has specifically examined application of an electric field on the catalyst beds. [8–10] As described in chapter 1, "the catalytic reactions in the electric field" means the catalytic reactions facilitated by the application of direct current into semiconductor. The reaction in the electric field is totally different from the conventional electrochemical reactions. Also, its promotion effect is not derived from the Joule heating. We have reported that the electric field invoke the reactions between OH groups and reactants like CH_4 and N_2 adsorbed over loading metals. The peculiar role of OH in the electric field enables catalysis of various reactions at low temperatures. Catalytic reactions in an electric field are promising. In-depth knowledge of those novel catalytic reactions is increasingly valuable.

The works presented in this chapter specifically addressed the importance of OH–CeO_2 interactions on catalysis related to surface protonics. NH_3 synthesis facilitated in an electric field was chosen as a model reaction. Actually, NH_3 is an extremely important chemical feedstock used as a raw material for fertilizers, resins, and fibers. These days, it is also receiving attention as a hydrogen carrier because of its high hydrogen content and ease of handling. [11, 12] Therefore, a novel efficient process for NH_3 synthesis is desired from the perspective of developing a sustainable society.

Results presented in the following sections have revealed the contributions of H^+ amounts adsorbed onto O_{lat} (O_{lat}-H^+) to the temperature dependence of NH_3 synthesis in an electric field. Furthermore, we have revealed that the O_{lat}-H^+ amount under a H_2 atmosphere can be tuned by doping of heterocations, as described in chapter 3. Therefore, the heterocation-doping effects on NH_3 synthesis in the electric field were also investigated.

4.2. Experimental

4.2.1. Catalyst preparation

CeO_2 and $Ce_{0.9}M_{0.1}O_{2-\delta}$ (M: Al and Sr) were synthesized as a support. A complex polymerization method was used in the same manner as that shown in Chapters 2 and 3. CeO_2 (JRC-CEO-01), which was supplied from the Catalyst Society of Japan, was also used as a support.

Using the supports listed above, active metals loaded catalysts of 1wt%Ru/support were prepared using an impregnation method. First, $Ru(acac)_3$ was dissolved into acetone. Then, support powders were added to the solutions and stirred at room temperature for 2 h. The slurries were dried over a hot plate for the evaporation of solvents. Subsequently, the obtained powers were reduced at 723 K for 2 h under Ar: H_2 = 1: 1 (total flow, 100 SCCM). Prepared catalysts were molded into 355–500 μm particles for activity tests and DRIFTS measurements.

4.2.2. Catalytic activity tests

All activity tests were conducted using a fixed-bed flow-type reactor under 0.1 MPa. A schematic image of the reactor is shown in Fig. 1.7. Two 2-mm-diameter stainless steel rods were attached to the catalyst beds. Through these electrodes, 0 or 6 mA direct current (Current density: 212 A m^{-2}) was applied to the catalyst bed using a power supply device. Catalyst bed temperatures were detected directly using a thermocouple inside the reactor. The thermocouple was attached to the catalyst beds at the bottom. Applied current and voltage were measured using a digital phosphor oscilloscope (TDS 2001C; Tektronix Inc.). The obtained signals showed that the applied voltages were stable during the activity tests. For all tests, 100 mg of catalysts were charged. Before activity tests, the catalysts were pre-reduced at 723 K for 2 h under N_2: H_2 = 1: 3 (240 SCCM total flow rate, 0.1 MPa total pressure). Synthesized NH_3 during activity tests was trapped in cold distilled water and then quantitatively analyzed using an ion chromatograph (IC-2001; Tosoh Corp.). Unless other notation is given, the activity tests were performed under N_2: H_2 = 1: 3 (240 SCCM total flow rate, 0.1 MPa total pressure).

4.2.3. *In-situ* FT-IR measurement in transmission mode

In-situ FT-IR measurements were performed in transmission mode (FT-IR 6200; Jasco Corp.) using pelletized 1wt%Ru/CeO_2 (JRC-CEO-01). For pellet preparation, 1wt%Ru/CeO_2 (JRC-CEO-01) powders were pressed at 40 kN for 1 min. The measurement scheme is shown in Fig. A.4.1. First, the sample was pre-reduced at 723 K with N_2 (5 SCCM) and H_2 (15 SCCM) supply for 2 h. Later, the cell interior was purged under Ar (20 SCCM) at 673 K for 1 h for removing O_{lat}-H^+. Desorption with purging was confirmed before this test. Then, background data were measured under Ar (20 SCCM) flow at each temperature (323, 373, 423, 473, 573, and 673 K). Finally, peaks assigned to O_{lat}-D^+ stretching were detected under N_2 (5 SCCM) and D_2 (15 SCCM) at each temperature. Before each observation, the catalyst was pre-purged by Ar (20 SCCM) flow at 673 K for 1 h.

4.2.4. *in-situ* DRIFTS measurement

In-situ DRIFTS measurements (FT-IR 6200; Jasco Corp.) with a ZnSe window and MCT detector were conducted using 355–500 μm granules of 1wt%Ru/CeO_2 (JRC-CEO-01). The customized cell for DRIFTS measurements with the electric field is insufficiently heat resistant. Therefore, measurements were conducted at a temperature lower than 473 K. First, the sample was pre-reduced under N_2 (5 SCCM) and H_2 (15 SCCM) at 473 K for 2 h. Later, the cell was purged by Ar (20 SCCM) at 473 K for 1 h. Then, the background spectrum was collected under Ar (20 SCCM) at 323 and 473 K. After N_2 (5 SCCM) and D_2 (15 SCCM) were supplied at each temperature, the spectra were measured at 323 K and 473 K with and without the electric field (0 and 6 mA). Before all measurements under N_2 and D_2, the catalyst was pre-treated under Ar (20 SCCM) at 473 K for 1 h to remove the adsorbed species.

4.3. Results and discussion

4.3.1. Specific temperature dependence of NH_3 synthesis in the electric field

To elucidate the effects of OH-CeO_2 interactions on NH_3 synthesis in the electric field, the temperature and H_2 partial pressure (P_{H2}) dependence of the NH_3 synthesis rate (r) were investigated using 1wt%Ru/CeO_2 (JRC-CEO-01) as a catalyst, as shown in Fig. 4.1. Without the electric field, conventional Arrhenius-like behavior was confirmed (open symbols in Fig. 4.1(a) and Table A.4.1). Applying the electric field caused completely different temperature dependence of the NH_3 synthesis rate (closed symbols in Fig. 4.1(b) and Tables A.4.2). First, conventional Arrhenius-like behavior was detected at the high-temperature region (573–673 K). In contrast, NH_3 synthesis rates increased concomitantly with the decrement in reaction temperatures at around 373–573 K. Additionally, Arrhenius-like behavior was obtained again at temperatures lower than around 373 K. This specific temperature dependence indicates a change in the NH_3 synthesis mechanism by application of the electric field as introduced in Chapter 1. Therefore, one can infer that some factors, which become advantageous at lower temperatures, play important roles in the NH_3 synthesis in the electric field. For further understanding, the P_{H2} dependence was examined (Fig. 4.1(b) and Tables A.4.2–A4.4). At temperature regions where NH_3 synthesis rates increased along with the decrement in reaction temperatures (373–573 K), the reaction rates increased as the P_{H2} increased. The reaction rates did not change at other temperature regions. Reportedly, Ru-based catalysts exhibit negative dependence on P_{H2} because of H_2 poisoning over the Ru surface. [13, 14] Using CeO_2 support, the poisoning over Ru is suppressed by hydrogen spillover. [15] We also confirmed almost identical activities irrespective of P_{H2} without the electric field (Fig. A.4.2 and Tables A.4.1, A4.5–A.4.6). Therefore, the positive effects of P_{H2} on NH_3 synthesis rate over 1wt%Ru/CeO_2 (JRC-CEO-01) in the electric field also suggest a novel reaction mechanism in the electric field. From this specific dependence exhibited in Fig. 4.1, we inferred that the adsorbed species formed by supplied H_2 was a fundamentally important the rate-determining step. As introduced in chapter 1, we have reported that NH_3 synthesis in the electric field proceeds *via* an "associative mechanism", where N_2H is formed from N_2 on active metals and O_{lat}-H^+ over metal oxide supports. [16–20] Therefore, the temperature dependence of the amount of O_{lat}-H^+ over CeO_2 can be inferred as the important factor leading to the peculiar behavior in the electric field shown in Fig. 4.1.

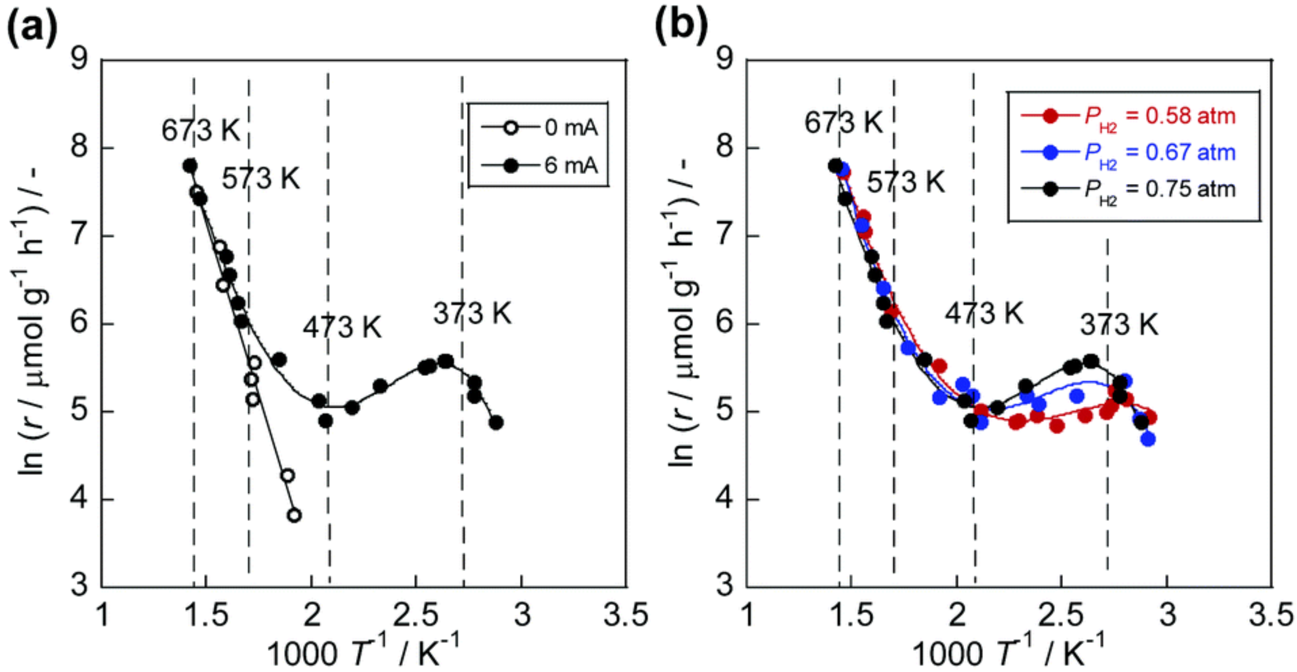

Figure 4.1. Arrhenius plots for NH_3 synthesis rate (r): (a) with and without the electric field (0 and 6 mA) under P_{H2} = 0.75 atm; and (b) P_{H2} dependence in the electric field (0.58, 0.67, and 0.75 atm) with 6 mA: Catalyst, 1wt%Ru/CeO_2 (JRC-CEO-01); total flow rate, 240 SCCM; total pressure, 0.1 MPa. Copyright 2020 RSC Publishing.

4.3.2. Temperature dependence of the O_{lat}-H^+ amount over CeO_2

To evaluate the assumption described above quantitatively, the temperature dependence of O_{lat}-H^+ coverage was assessed using *in situ* DRIFTS measurements in transparent mode without the electric field (Fig. 4.2 (a)) and DRIFTS mode with and without the electric field (Fig. 4.2 (b)). D_2 was supplied as a reactant instead of H_2 to exclude effects of atmospheric H_2O outside of the cell. O_{lat}-D^+ stretching peaks were detected at around 2780 cm^{-1}[21] after D_2 supply. Therefore, probably the O_{lat}-H^+(D^+) considered in chapter 3 exists on the surface of 1 wt%Ru/CeO_2 (JRC-

CEO-01) under H_2 (D_2) atmosphere. Then, the peak area of O_{lat}-D^+ stretching peaks was used for *pseudo*-quantitative analysis of the O_{lat}-H^+ coverage. IR measurements in transmission mode are suitable for quantitative investigation. However, the electric field cannot be applied because of the measurement cell structure. Therefore, we also took DRIFTS measurements to investigate the electric field effects on the O_{lat}-H^+ amount, although DRIFTS cannot evaluate the precise quantitative amount, in principle. Qualitatively, the electric field showed no marked influence. Application of the electric field produces a small amount of Joule heat. Therefore, a small change of the spectrum can be expected to be attributable to the increase in temperature. In addition, the effect of the catalyst bed temperature (*i.e.* difference between 323 K and 473 K) on adsorption is much greater than the electric field effect. Therefore, using the data without the electric field (Fig. 4.2(a)), the relative coverage of O_{lat}-H^+ ($\theta(T)$) was calculated. The area at 323 K (Area (323 K)) was used as a reference.

$$\theta(T) = \text{Area}(T)/\text{Area}(323\ \text{K}) \tag{4.1}$$

The temperature dependence of $\theta(T)$ is shown in Fig. 4.2(b). Accordingly, the O_{lat}-H^+ coverage increased in accordance with the decrease in the temperature. The coverage saturated around 323–373 K.

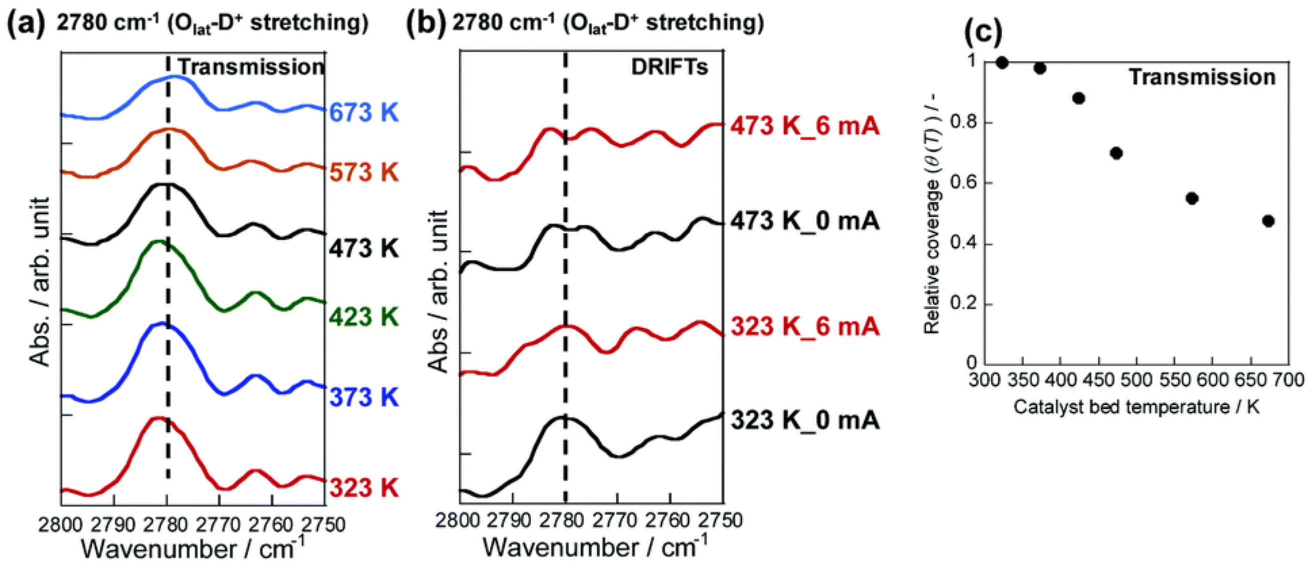

Figure 4.2. Quantitative analysis for O_{lat}-D^+ : (a) *in-situ* IR spectra in transmission mode; and (b) *in-situ* DRIFTS spectra with and without EF; and (c) relative coverage using transmission spectra (θ(T) = Area(T)/Area(323 K)): Catalyst, 1wt%Ru/CeO_2 (JRC-CEO-01); reactant, N_2 : D_2 = 1 : 3; total flow rate, 20 SCCM; total pressure, 0.1 MPa. Copyright 2020 RSC Publishing.

4.3.3. Reaction rate equation considering the temperature dependence of O_{lat}-H^+ amount

The obtained results in IR measurements suggest the contribution of O_{lat}-H^+ coverage on specific temperature dependence in the electric field. At the high-temperature region (> 573 K), the decrease in O_{lat}-H^+ coverage on CeO_2 renders enhancement of the NH_3 synthesis rate by the electric field negligible. The NH_3 synthesis proceeds *via* a conventional "dissociative mechanism". Figure 4.2(a) showed that the O_{lat}-D^+ existed on CeO_2 to some extent, even in a high-temperature region. However, the electric field effects became smaller because of the following reasons. First, the reaction *via* the "dissociative mechanism" is much more active at high temperatures. In addition, the reaction *via* the "associative mechanism" is expected to be limited at the three-phase boundary (TPB), although the reaction through the "dissociative mechanism" can proceed at all regions of the exposed metal surface. Therefore, the reaction sites for the "associative mechanism" are much smaller than those for the "dissociative mechanism". For those reasons, the contribution of the "associative mechanism" became trivial at a high temperature, even though O_{lat}-H^+ remains. However, at a low-temperature region (< 373 K), CeO_2 surface is sufficiently covered by O_{lat}-H^+. In addition, the reaction rate of direct N_2 dissociation is negligible at low temperatures. Therefore, almost all NH_3 is produced reaction *via* the "associative mechanism". At a middle-temperature region (373–573 K), the overall reaction rate can be described by the sum of the reaction rates through both the "dissociative mechanism" and the "associative mechanism". Therefore, we formulated the overall NH_3 synthesis rate in the electric field as shown below.

$$r_{\mathrm{calc}}(T) = r_{\mathrm{dissociative}}(T) + \theta(T) \times r_{\mathrm{associative}}(T) \tag{4.2}$$

In that equation, $r_{\mathrm{dissociative}}(T)$ and $r_{\mathrm{associative}}(T)$ show the extrapolated values according to Fig. 4.3. The Arrhenius plots without the electric field are used for the expression of $r_{\mathrm{dissociative}}(T)$; also, $r_{\mathrm{associative}}(T)$ was calculated using an experimentally obtained approximate straight line at a low temperature (T < 373 K). In this range of low temperatures, the change of $\theta(T)$ was negligible. Therefore, Arrhenius-like behavior was confirmed for NH_3 synthesis rate in the electric field. Results show that the straight line on the right side in Fig. 4.3 represents the temperature dependence of NH_3 synthesis rate *via* the "associative mechanism" when the O_{lat}-H^+ coverage is maximum and does not change along with temperatures. Rate-determining step approximation was applied to the second term of equation (4.2). We assumed that the rate-determining step in the electric field would be the reaction between O_{lat}-H^+ and N_2 (formation of N_2H), meaning that the reaction rate depends linearly on the O_{lat}-H^+ concentration. In terms of the O_{lat}-H^+ concentration, $\theta(T)$ obtained from IR measurements (Fig. 4.2 (c)) were used. Figure 4.3 presents a comparison between the experimentally obtained values and $r_{\mathrm{calc}}(T)$. It is particularly interesting that the calculated value showed excellent matching with the experimental values. This agreement indicates some correlation between the activation of the NH_3 synthesis and O_{lat}-H^+ amount in the electric field. Moreover, this discovery is expected to be extended to other reaction systems. It will provide important guidance for the optimization of catalysts and reaction conditions related OH groups in the electric filed.

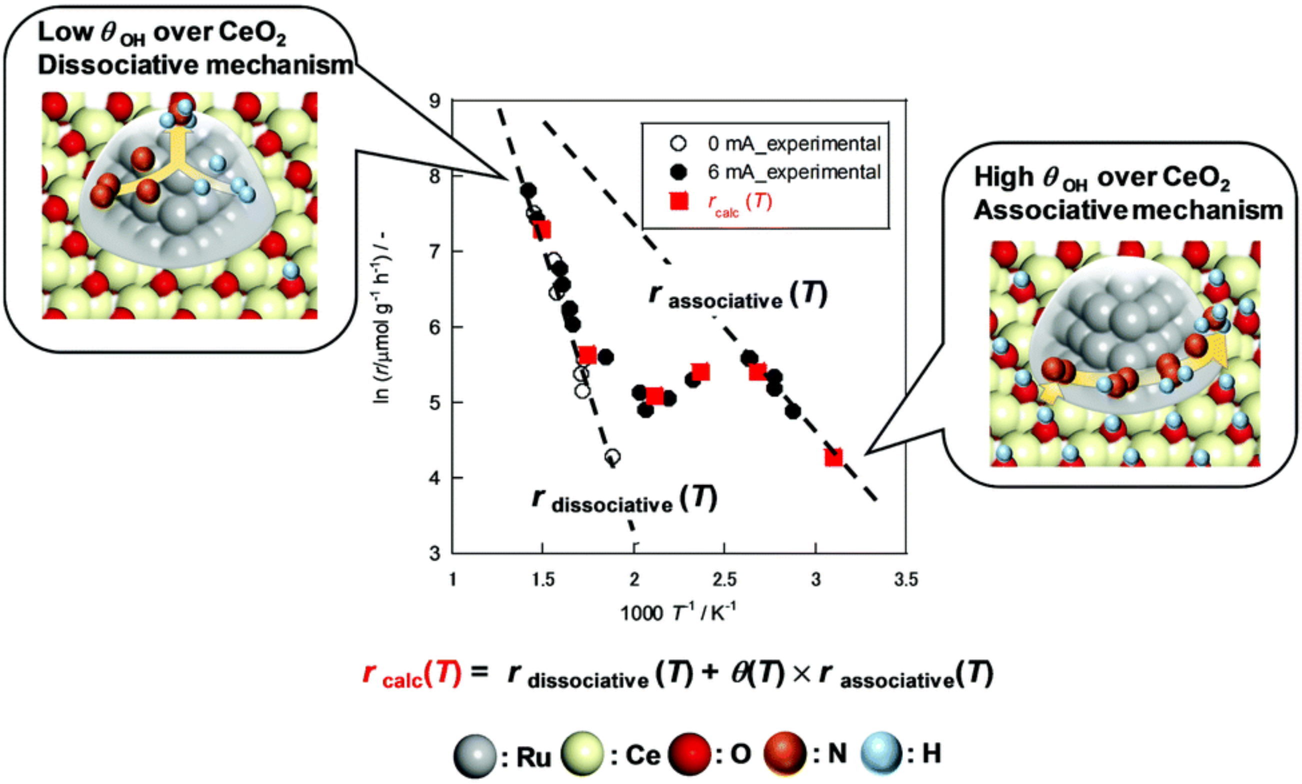

Figure 4.3. Experimental reaction rate under P_{H2} = 0.78 atm and calculated reaction rate ($r_{calc}(T)$). Data in Figure 4.1 are used for $r_{dissociative}$ and $r_{associative}$: Catalyst, 1wt%Ru/CeO_2 (JRC-CEO-01); total flow rate, 240 SCCM; total pressure, 0.1 MPa. Copyright 2020 RSC Publishing.

4.3.4. Heterocation-doping effects on catalytic reactions related to OH

The discussion presented above has elucidated the great importance of O_{lat}-H^+ amount in catalysis with the electric field under H_2 atmosphere. Additionally, results show that the O_{lat}-H^+ amount over CeO_2 can be controlled by heterocation doping in Chapter 3. Therefore, we studied the effect of heterocation doping on the NH_3 synthesis rate in the electric field using 1wt%Ru/CeO_2 and 1wt%Ru/$Ce_{1-x}M_xO_{2-\delta}$ (M : Al and Sr). It has been revealed that Al doping and Sr doping respectively exert positive and negative effects on O_{lat}-H^+ amount (Figs. 3.3 and 3.6). Figure 4.4 and Tables A.4.7–A.4.9 represents heterocation-doping effects on the temperature dependence of NH_3 synthesis rate in the electric field. Consequently, the manipulation of O_{lat}-H^+ amounts by heterocation doping markedly changed the temperature dependence of catalysis involving surface protonics. First, the synthesis rate at around 373–573 K was increased significantly by Al doping. It indicates that high coverage of O_{lat}-H^+ was maintained at around 373–573 K by virtue of the doping of Al. In addition, the NH_3 synthesis rates did not increase with the decrement in catalyst bed temperatures at around 373–573 K because the NH_3 synthesis rate, which proceeds by conventional "dissociative mechanism", begins to increase before a significant decrease in O_{lat}-H^+ as a result of the increase in temperature. Sr doping did not change the temperature dependence to any great degree. However, the increase of NH_3 synthesis rate along with the decrease in temperature did not reach a limit even at around 373 K. That finding indicates that the coverage of O_{lat}-H^+ did not hit a ceiling at 373 K because of the decrease in O_{lat}-H^+ stability by Sr doping. In summary, these findings indicate that heterocation doping can control the catalytic performance involving OH groups in the electric field.

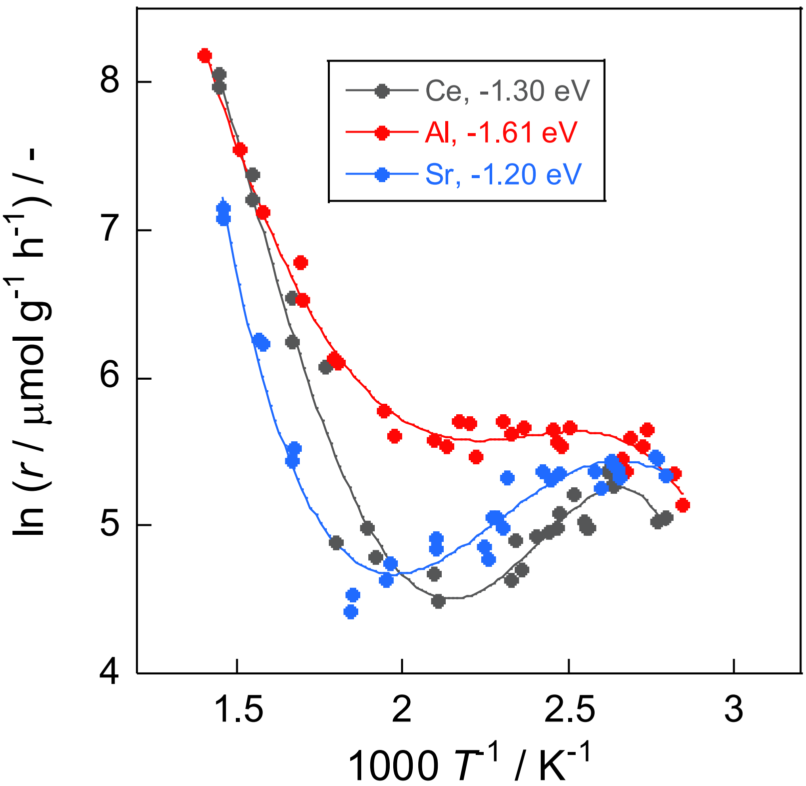

Figure 4.4. Arrhenius plots for NH_3 synthesis rate (r): Catalyst, 1wt%Ru/CeO_2, 1wt%Ru/$Ce_{0.9}Al_{0.1}O_{2-\delta}$, 1wt%Ru/$Ce_{0.9}Sr_{0.1}O_{2-\delta}$; applied current, 6 mA; total flow rate, 240 SCCM; P_{H2}, 0.75 atom, total pressure, 0.1 MPa.

4.4. Chapter Conclusion

We elucidated the key role of O_{lat}-H^+ amount over CeO_2 on catalysis in the electric field under H_2 atmosphere. The rate of NH_3 synthesis proceeding *via* N_2H also increased as the catalyst bed temperature decreased at around 573–373 K. This specific trend results from the increase in O_{lat}-H^+ amount along with the decrement in temperature. The quantitative correlation between O_{lat}-H^+ amount and NH_3 synthesis rate in the electric field was revealed to be in line with *in-situ* IR measurements. In addition, the manipulation of O_{lat}-H^+ amounts by heterocation doping significantly changed the temperature dependence of NH_3 synthesis in the electric field. Those results elucidated the importance of DFT-suggestion about heterocation-doping effects on OH–CeO_2 interaction.

References

1. A. Iwase and A. Kudo, Development of Ir and La-codoped $BaTa_2O_6$ photocatalysts using visible light up to 640 nm as an H_2-evolving photocatalyst for Z-schematic water splitting, *Chem. Commun.*, 2017, **53**, 6156 – 6159.
2. J. Xu, C. Pan, T. Takata and K. Domen, Photocatalytic overall water splitting on the perovskite-type transition metal oxynitride $CaTaO_2N$ under visible light irradiation, *Chem. Commun.*, 2015, **51**, 7191 – 7194.
3. F. Che, J. T. Gray, S. Ha, and J. S. McEwen, Reducing Reaction Temperature, Steam Requirements, and Coke Formation During Methane Steam Reforming Using Electric Fields: A Microkinetic Modeling and Experimental Study, *ACS Catal.*, 2017, **7(10)**, 6957 – 6968.
4. A. Yamamoto, S. Mizuaba, Y. Saeki and H. Yoshida, Platinum loaded sodium tantalate photocatalysts prepared by a flux method for photocatalytic steam reforming of methane, *Appl. Catal., A*, 2016, **521**, 125 – 132.
5. M. Iwamoto, M. Akiyama, K. Aihara, and T. Deguchi, Ammonia Synthesis on Wool-Like Au, Pt, Pd, Ag, or Cu Electrode Catalysts in Nonthermal Atmospheric-Pressure Plasma of N_2 and H_2, *ACS Catal.*, 2017, **7**, 6924 – 6929.
6. Y. Kobayashi, N. Kimua, and Y. Satokawa, *ECS Transactions*, Electrochemical Synthesis of Ammonia Using Proton Conducting Solid Electrolyte and Ru-doped $BaCe_{0.9}Y_{0.1}O_{3-\delta}$ Electrode Catalyst, 2017, **75(42)**, 43 – 52.
7. L. Zhangm L. X. Ding, G. F. Chen, X. Yang, and H. Wang, Ammonia Synthesis Under Ambient Conditions: Selective Electroreduction of Dinitrogen to Ammonia on Black Phosphorus Nanosheets, *Angew. Chem. Int. Ed.*, 2019, **58**, 2612 – 2616.
8. S. Ogo, Y. Sekine, Catalytic reaction assisted by plasma or electric field, *Chem. Rec.*, 2017, **17(8)**, 726 – 738.
9. M. Torimoto, K. Murakami, Y. Sekine, Low-temperature heterogenous catalytic reaction by surface protonics, *Bull. Chem. Soc. Jpn.*, 2019, **92(10)**, 1785 – 1792.
10. Y. Sekine and R. Manabe, Reaction mechanism of low-temperature catalysis by surface protonics in an electric field, *Faraday Discuss.*, *in press*. DOI: 10.1039/C9FD00129H
11. U. B. Demirci, P. Miele, Chemical hydrogen storage: “material” gravimetric capacity *versus* “system” gravimetric capacity, *Energy Environ. Sci.*, 2011, **4**, 3334 – 3341.
12. K. Takise and Y. Sekine, Production, storage, utilization of hydrogen, *Acc. Mater. Surf. Res.*, 2019, **4(3)**, 115 – 134.
13. K. Aika, Role of alkali promoter in ammonia synthesis over ruthenium catalysts-Effect on reaction mechanism, *Catal. Today*, 2017, **286**, 14 – 20.

14. H. Bielawa, O. Hinrichsen, A. Birkner, and M. Muhler, The Ammonia-Synthesis Catalyst of the Next Generation: Barium-Promoted Oxide-Supported Ruthenium, *Angew. Chem., Int. Ed.*, 2001, **40**, 1061 – 1063.
15. Y. Niwa and K. Aika, Ruthenium Catalyst Supported on CeO_2 for Ammonia Synthesis, *Chem*. *Lett*., 1996, **25(1)**, 3 – 4.
16. R. Manabe, H. Nakatsubo, A. Gondo, K. Murakami, S. Ogo, H. Tsuneki, M. Ikeda, A. Ishikawa, H. Nakai, and Y. Sekine, Electrocatalytic synthesis of ammonia by surface proton hopping, *Chem*. *Sci*., 2017, **8**, 5434 – 5439.
17. A. Gondo, R. Manabe, R. Sakai, K. Murakami, T. Yabe, S. Ogo, M. Ikeda, H. Tsuneki, and Y. Sekine, Ammonia Synthesis Over Co Catalyst in an Electric Field, *Catal*. *Lett*., 2018, **148**, 1929 – 1938.
18. K. Murakami, R. Manabe, H. Nakatsubo, T. Yabe, S. Ogo, Y. Sekine, Elucidation of the role of electric field on low temperature ammonia synthesis using isotopes, *Catal*. *Today*, 2018, **303**, 271 – 275.
19. K. Murakami, Y. Tanaka, S. Hayashi, R. Sakai, Y. Hisai, Y. Mizutani, A. Ishikawa, H. Nakai, Y. Sekine, Governing factors of supports of ammonia synthesis in an electric field found using density functional theory, *J. Chem*. *Phys*., 2019, **151**, 064708.
20. K. Murakami, Y. Tanaka, R. Sakai, K. Toko, K. Ito, A. Ishikawa, T. Higo, T. Yabe, S. Ogo, M. Ikeda, H. Tsuneki, H. Nakai, Y. Sekine, The important role of N_2H formation energy for low-temperature ammonia synthesis in an electric field, *Catal*. *Today*, 2020, **351**, 119 – 124.
21. K. Werner, X. Weng, F. Calaza, M. Sterrer, T. Kropp, J. Paier, J. Sauer, M. Wilde, K. Fukutani, S. Shaikhutdinov, and H. J. Freund, Toward an Understanding of Selective Alkyne Hydrogenation on Ceria: On the Impact of O Vacancies on H_2 Interaction with CeO_2(111), *J. Am. Chem. Soc.*, 2017, **139**, 17608 – 17616.

Appendix of Chapter 4

A.4.1. The effects of the electric field on CeO_2 morphology

XRD measurements were conducted to evaluate the effects of the electric field on morphology of CeO_2. Measurement conditions are shown in part 2.2.3. Figure A.4.3 shows the XRD patterns for CeO_2 (JRC-CEO-01), 1wt%Ru/CeO_2 (JRC-CEO-01) before activity tests, and 1wt%Ru/CeO_2 (JRC-CEO-01) after activity tests. Consequently, we confirmed no change of CeO_2 morphology even after applying the electric field.

A.4.2. Applied current dependence of NH_3 synthesis rate in the electric field

Applied current dependence of NH_3 synthesis rate in the electric field was investigated using 1wt%Ru/CeO_2 (JRC-CEO-01), see Figure A.4.4. Here, the synthesis rate was evaluated using the synthesis rate per applied power (r_W) calculated as blow.

$$r_W = \frac{r}{I \times V} \quad \text{(A.4.1)}$$

I and V meant applied currents and voltages, respectively. As a result, r_W showed almost identical values among all applied current. It stands for the importance of applied power for the activation of the NH_3 synthesis. This trend was consistent with previous studies. [1]

A.4.3. CO-pulse

The Ru particle sizes over 1wt%Ru/CeO_2, $Ce_{0.9}Al_{0.1}O_{2-\delta}$, $Ce_{0.9}Sr_{0.1}O_{2-\delta}$ were evaluated using CO pulse (Autosorb-iQ; Quantachrome Instruments Japan G.K.). The catalysts were pre-treated under H_2 flow at 723 K for 2 h and evacuated at 723 K for 1 h. Afterwards, the temperature was decreased to 323 K under He flow, and 10% CO was dosed. The stoichiometric adsorption of CO over Ru and hemisphere approximation were applied when calculating the Ru particle size. Calculated Ru particle sizes are summarized in Table A.4.10. It was found that Ru particles tend to aggregate on Sr-doped CeO_2.

A.4.4. Brunauer-Emmett-Teller (BET)

The specific surface areas of CeO_2, $Ce_{0.9}Al_{0.1}O_{2-\delta}$, $Ce_{0.9}Sr_{0.1}O_{2-\delta}$ were evaluated by N_2 adsorption using Brunauer-Emmett-Teller (BET) method (Gemini VII 2390a; Micromeritics Instrument Corp.). The samples were pre-treated at 473 K for 2 h under N_2 atmosphere. The obtained results are summarized in Table A.4.11.

A.4.5. Heterocation-doping effects on the NH_3 synthesis without the electric field

Heterocation-doping effect on NH_3 synthesis without the electric field was investigated using 1wt%Ru/CeO_2, $Ce_{0.9}Al_{0.1}O_{2-\delta}$, $Ce_{0.9}Sr_{0.1}O_{2-\delta}$ (Figures A.4.5-A.4.6, and Tables A.4.12-4.14). As shown in Figures A.4.5, 1wt%Ru/$Ce_{0.9}Sr_{0.1}O_{2-\delta}$ exhibited smaller activity than other catalysts. The decrement would be caused by the sintering of Ru particles as shown in part A.4.2. Hence, turnover frequency normalized by the amount of the exposed metal Ru (TOF-s) was calculated using Ru particle sizes. All catalysts exhibited almost identical TOFs as shown in Figure A.4.6.

References

1. M. Torimoto, S. Ogo, D. Harjowinoto, T. Higo, J. G. Seo, S. Furukawa and Y. Sekine, Enhanced methane activation on diluted metal–metal ensembles under an electric field: breakthrough in alloy catalysis, *Chem*. *Commun*., 2019, **55**, 6693-6695.

Figures and Tables

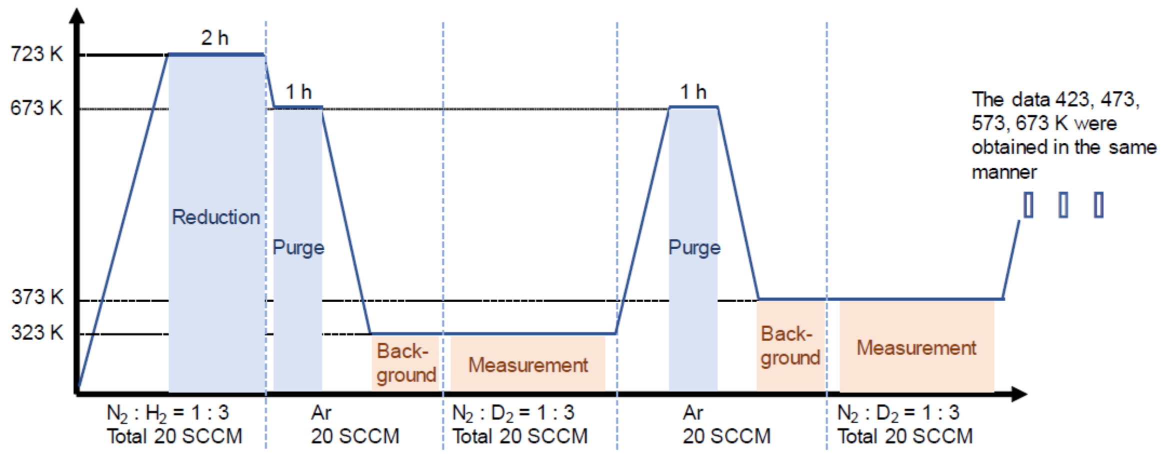

Figure A.4.1. Schematic image of flow for *in-situ* IR measurement in transparent mode. Copyright 2020 RSC Publishing.

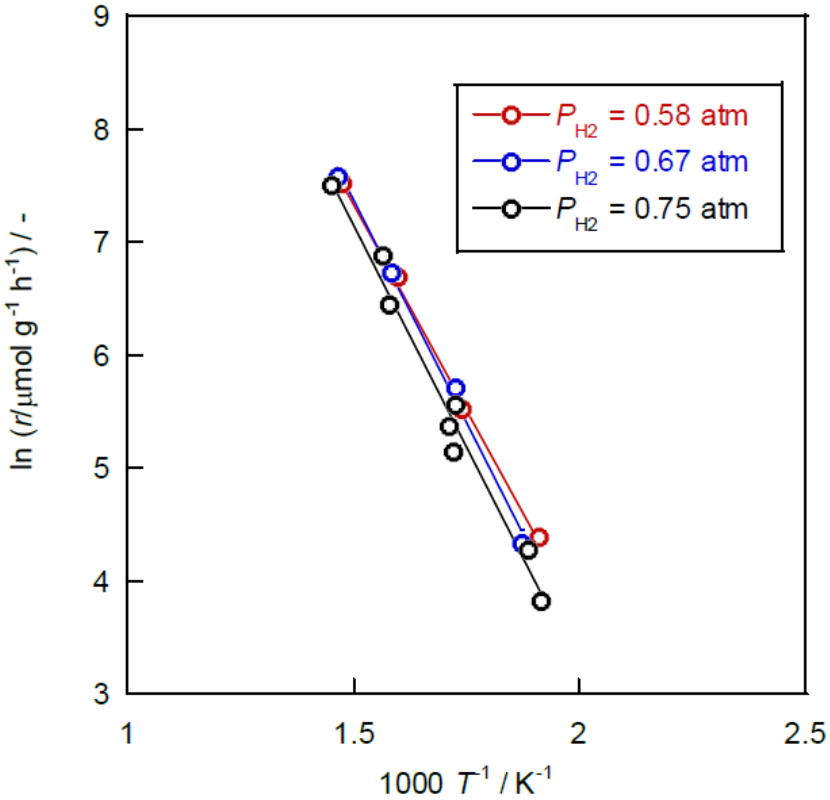

Figure A.4.2. Arrhenius plots for NH_3 synthesis rate (r) under several P_{H2} (0.58, 0.67 and 0.75 atm): Catalyst, 1wt%Ru/CeO_2 (JRC-CEO-01); applied current, 0 mA; total flow rate, 240 SCCM; total pressure, 0.1 MPa. Copyright 2020 RSC Publishing.

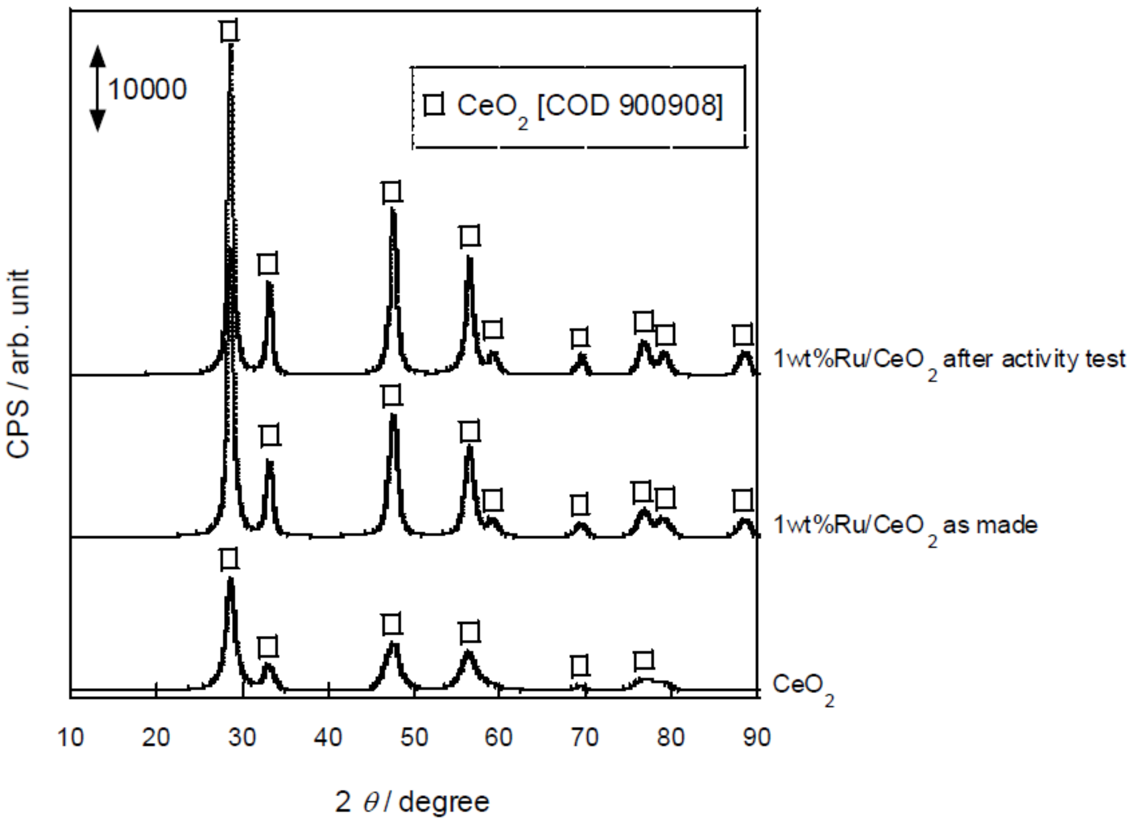

Figure A.4.3. XRD spectra for CeO_2 (JRC-CEO-01) and 1wt%Ru/CeO_2 (JRC-CEO-01) as made and after activity test. Copyright 2020 RSC Publishing.

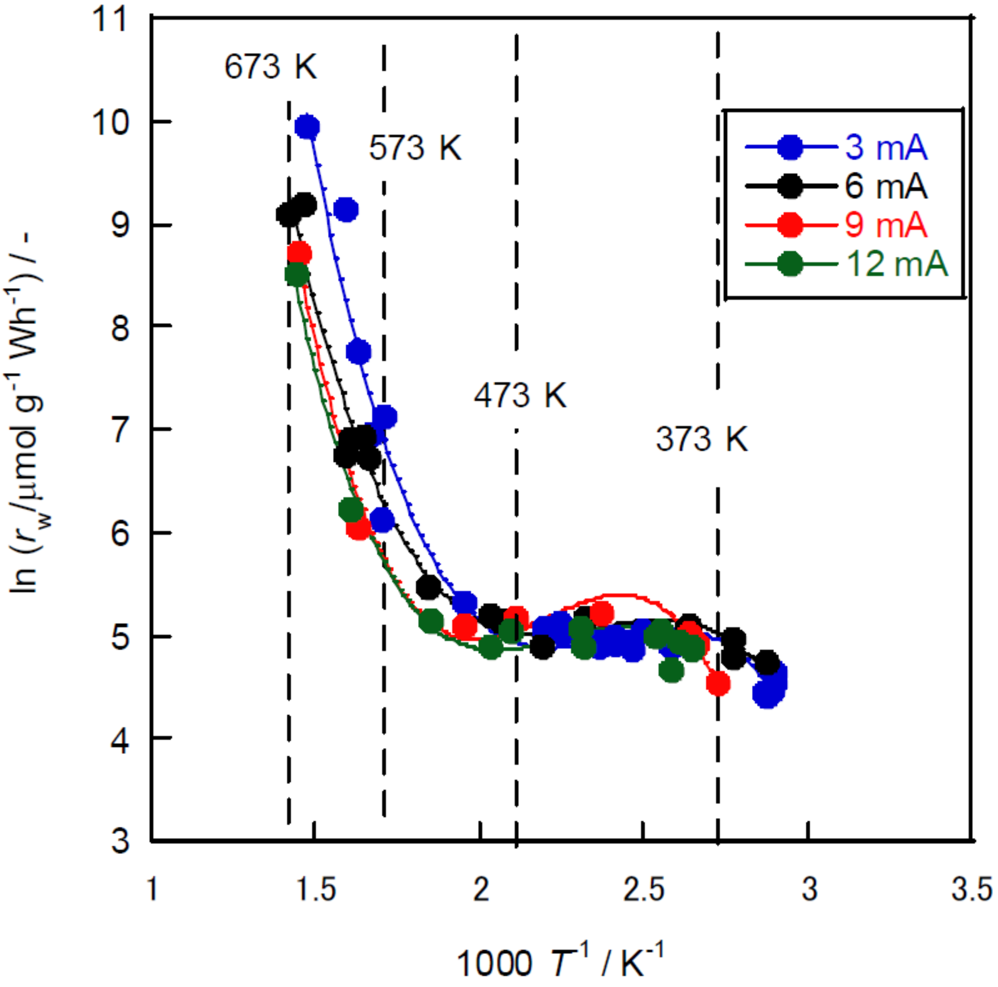

Figure A.4.4. Arrhenius plots for NH_3 synthesis rate per input power (r_w): Catalyst, 1wt%Ru/CeO_2 (JRC-CEO-01); applied current, 3-12 mA; total flow rate, 240 SCCM; P_{H2}, 0.75 atom; total pressure, 0.1 MPa. Copyright 2020 RSC Publishing.

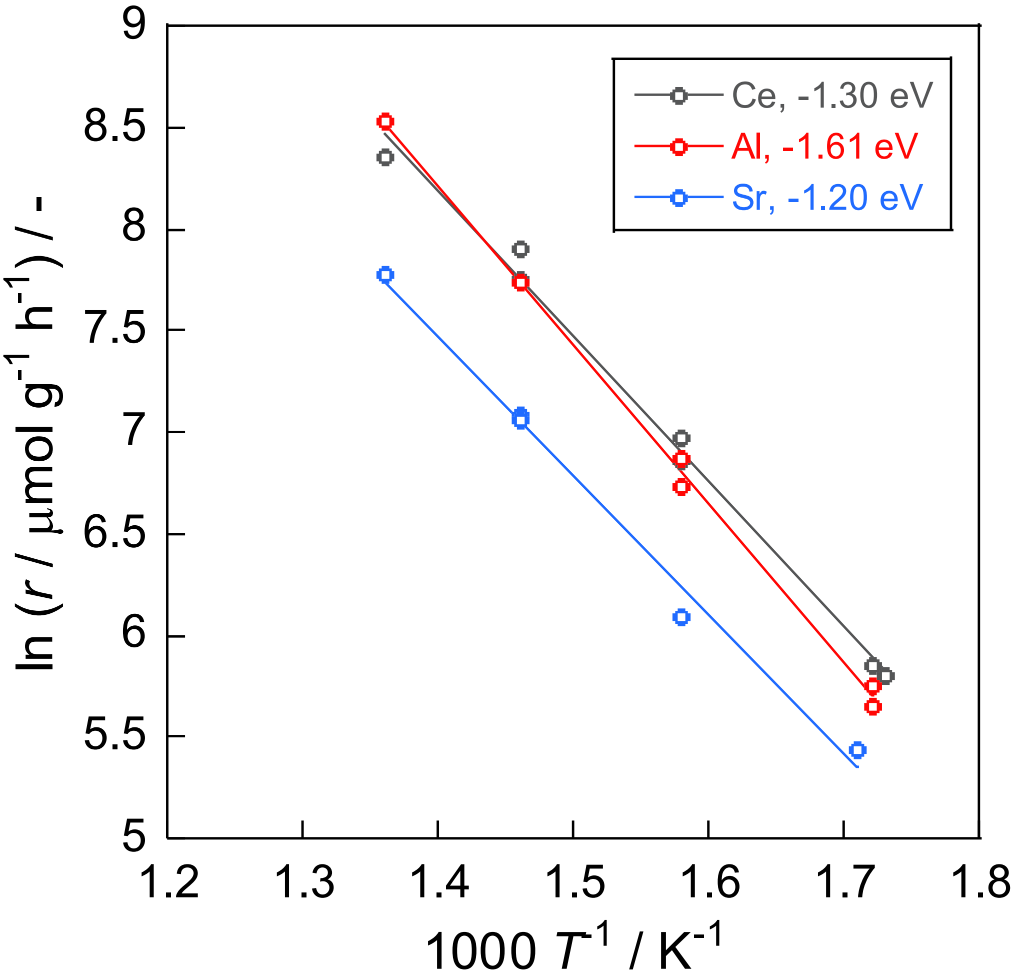

Figure A.4.5. Arrhenius plots for NH_3 synthesis rate (r): Catalyst, 1wt%Ru/CeO_2, $Ce_{0.9}Al_{0.1}O_{2-\delta}$, $Ce_{0.9}Sr_{0.1}O_{2-\delta}$; applied current, 0 mA; total flow rate, 240 SCCM; total pressure, 0.1 MPa.

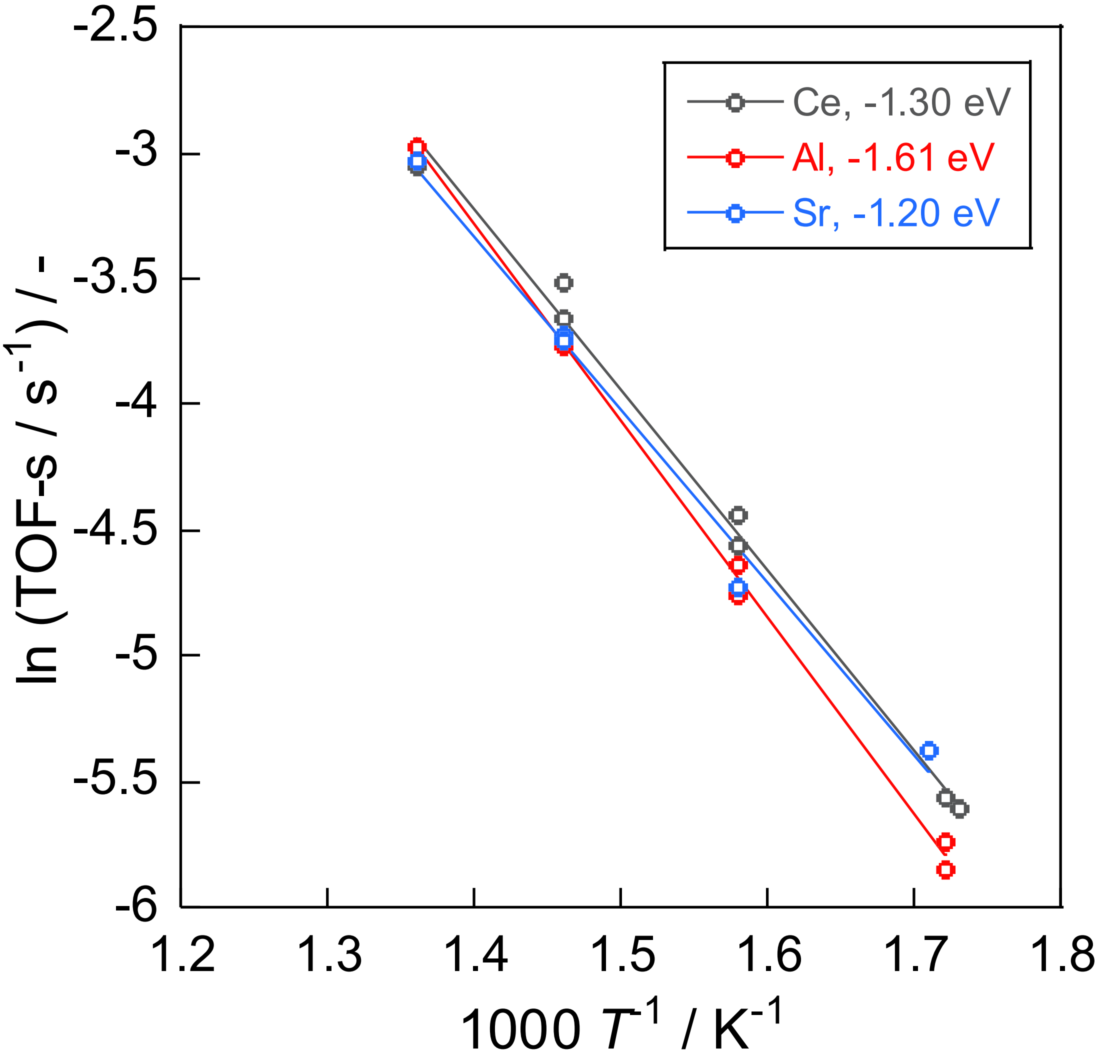

Figure A.4.5. Arrhenius plots for TOF-s: Catalyst, 1wt%Ru/CeO_2, $Ce_{0.9}Al_{0.1}O_{2-\delta}$, $Ce_{0.9}Sr_{0.1}O_{2-\delta}$; applied current, 0 mA; total flow rate, 240 SCCM; P_{H2}, 0.75 atom; total pressure, 0.1 MPa.

Table A.4.1. NH_3 synthesis rate (*r*): Catalyst, 1wt%Ru/CeO_2 (JRC-CEO-01); applied current, 0 mA; total flow rate, 240 SCCM; P_{H2}, 0.75 atom; total pressure, 0.1 MPa.

Catalyst bed temperature / K	NH_3 synthesis rate / μmol g^{-1} h^{-1}	1000/*T* / K^{-1}	ln *r* / -
522	46.4	1.91	3.84
530	73.0	1.89	4.29
580	261.1	1.72	5.57
581	173.9	1.72	5.16
585	215.6	1.71	5.37
634	637.8	1.58	6.46
641	988.4	1.56	6.90
690	1837.9	1.45	7.52

Table A.4.2. NH_3 synthesis rate (r): Catalyst, 1wt%Ru/CeO_2 (JRC-CEO-01); applied current, 6 mA; total flow rate, 240 SCCM; P_{H2}, 0.75 atom; total pressure, 0.1 MPa. Copyright 2020 RSC Publishing.

Catalyst bed temperature / K	Response voltage / kV	NH_3 synthesis rate / μmol g^{-1} h^{-1}	$1000/T$ / K^{-1}	ln r / -
348	-0.19	131.4	2.88	4.88
360	-0.25	181.0	2.78	5.20
361	-0.24	208.3	2.77	5.34
379	-0.28	265.5	2.64	5.58
379	-0.28	266.4	2.64	5.58
430	-0.19	199.2	2.32	5.29
457	-0.20	157.7	2.19	5.06
484	-0.13	135.2	2.07	4.91
492	-0.16	168.0	2.03	5.12
541	-0.19	273.6	1.85	5.61
600	-0.08	416.5	1.67	6.03
606	-0.09	517.0	1.65	6.25
622	-0.12	716.3	1.61	6.57
629	-0.17	876.3	1.59	6.78
683	-0.03	1694.9	1.46	7.44
705	-0.05	2476.3	1.42	7.81

Table A.4.3. NH_3 synthesis rate (*r*): Catalyst, 1wt%Ru/CeO_2 (JRC-CEO-01); applied current, 6 mA; total flow rate, 240 SCCM; P_{H2}, 0.67 atom; total pressure, 0.1 MPa. Copyright 2020 RSC Publishing.

Catalyst bed temperature / K	Response voltage / kV	NH_3 synthesis rate / μmol g^{-1} h^{-1}	1000/*T* / K^{-1}	ln *r* / -
357.8	-0.22	212.5	2.79	5.36
389.5	-0.20	181.1	2.57	5.20
428.1	-0.20	177.8	2.34	5.18
482.2	-0.14	180.8	2.07	5.20
521.7	-0.12	176.7	1.92	5.17
566.3	-0.13	310.2	1.77	5.74
606.8	-0.10	610.1	1.65	6.41
646.7	-0.06	1254.5	1.55	7.13
689.5	-0.02	2367.4	1.45	7.77

Table A.4.4. NH_3 synthesis rate (*r*): Catalyst, 1wt%Ru/CeO_2 (JRC-CEO-01); applied current, 6 mA; total flow rate, 240 SCCM; P_{H2}, 0.58 atom; total pressure, 0.1 MPa. Copyright 2020 RSC Publishing.

Catalyst bed temperature / K	Response voltage / kV	NH_3 synthesis rate / μmol g^{-1} h^{-1}	1000/*T* / K^{-1}	ln *r* / -
342.5	-0.21	141.2	2.92	4.95
356.3	-0.22	173.4	2.81	5.16
364.0	-0.24	190.9	2.75	5.25
365.4	-0.19	161.3	2.74	5.08
369.3	-0.19	148.9	2.71	5.00
383.0	-0.18	143.6	2.61	4.97
404.0	-0.15	126.6	2.48	4.84
420.1	-0.18	144.0	2.38	4.97
436.7	-0.17	136.0	2.29	4.91
438.6	-0.16	131.8	2.28	4.88
472.8	-0.13	144.8	2.12	4.98
473.8	-0.14	152.6	2.11	5.03
521.7	-0.15	253.2	1.92	5.53
591.9	-0.06	466.5	1.69	6.15
639.8	-0.06	1156.5	1.56	7.05
643.7	-0.02	1371.7	1.55	7.22
684.2	-0.02	2304.3	1.46	7.74

Table A.4.5. NH_3 synthesis rate (r): Catalyst, 1wt%Ru/CeO_2 (JRC-CEO-01); applied current, 0 mA; total flow rate, 240 SCCM; P_{H2}, 0.67 atom; total pressure, 0.1 MPa. Copyright 2020 RSC Publishing.

Catalyst bed temperature / K	NH_3 synthesis rate / µmol g^{-1} h^{-1}	1000/T / K^{-1}	ln r / -
535.2	77.4	1.87	4.35
579.7	305.7	1.73	5.72
631.8	849.2	1.58	6.74
683.3	1985.2	1.46	7.59

Table A.4.6. NH_3 synthesis rate (r): Catalyst, 1wt%Ru/CeO_2 (JRC-CEO-01); applied current, 0 mA; total flow rate, 240 SCCM; P_{H2}, 0.58 atom; total pressure, 0.1 MPa. Copyright 2020 RSC Publishing.

Catalyst bed temperature / K	NH_3 synthesis rate / µmol g^{-1} h^{-1}	1000/T / K^{-1}	ln r / -
524	81.3	1.91	4.40
576	250.4	1.74	5.52
627	805.7	1.60	6.69
678	1854.5	1.47	7.53

Table A.4.7. NH_3 synthesis rate (*r*): Catalyst, 1wt%Ru/CeO_2; applied current, 6 mA; total flow rate, 240 SCCM; P_{H2}, 0.75 atom; total pressure, 0.1 MPa.

Catalyst bed temperature / K	Response voltage / kV	NH_3 synthesis rate / μmol g^{-1} h^{-1}	1000/*T* / K^{-1}	ln *r* / -
358	-0.28	159.1	2.79	5.07
361	-0.26	153.5	2.77	5.03
379	-0.29	194.8	2.64	5.27
379	-0.28	197.0	2.64	5.28
382	-0.29	215.4	2.62	5.37
391	-0.26	146.2	2.56	4.98
392	-0.24	147.2	2.55	4.99
393	-0.25	153.2	2.55	5.03
398	-0.27	183.9	2.51	5.21
405	-0.24	163.0	2.47	5.09
406	-0.23	147.4	2.46	4.99
410	-0.24	143.5	2.44	4.97
416	-0.19	140.0	2.40	4.94
424	-0.22	110.2	2.36	4.70
428	-0.29	135.1	2.34	4.91
430	-0.13	104.1	2.32	4.64
475	-0.14	89.5	2.10	4.49
478	-0.15	108.5	2.09	4.69
521	-0.15	120.2	1.92	4.79
528	-0.16	147.9	1.89	5.00
557	-0.07	133.7	1.80	4.90
567	-0.07	437.7	1.76	6.08
600	-0.07	517.9	1.67	6.25
601	-0.07	693.9	1.66	6.54
646	-0.12	1360.2	1.55	7.22
646	-0.13	1618.3	1.55	7.39
692	-0.07	3169.0	1.45	8.06
692	-0.07	2931.9	1.44	7.98

Table A.4.8. NH_3 synthesis rate (r): Catalyst, 1wt%Ru/$Ce_{0.9}Al_{0.1}O_{2-\delta}$; applied current, 6 mA; total flow rate, 240 SCCM; P_{H2}, 0.75 atom; total pressure, 0.1 MPa.

Catalyst bed temperature / K	Response voltage / kV	NH_3 synthesis rate / μmol g^{-1} h^{-1}	1000/T / K^{-1}	ln r / -
352	-0.21	171.8	2.84	5.15
355	-0.23	213.4	2.81	5.36
366	-0.29	285.6	2.73	5.65
367	-0.30	257.2	2.72	5.55
373	-0.32	272.0	2.68	5.61
374	-0.31	215.7	2.67	5.37
376	-0.29	236.2	2.66	5.46
399	-0.31	288.3	2.50	5.66
404	-0.27	255.1	2.47	5.54
405	-0.27	261.2	2.47	5.57
408	-0.28	285.8	2.45	5.66
423	-0.27	289.6	2.36	5.67
430	-0.27	278.7	2.33	5.63
435	-0.27	301.6	2.30	5.71
451	-0.27	239.5	2.22	5.48
454	-0.31	297.4	2.20	5.70
462	-0.30	303.9	2.17	5.72
470	-0.26	255.7	2.13	5.54
478	-0.27	266.7	2.09	5.59
507	-0.21	273.2	1.97	5.61
515	-0.25	327.3	1.94	5.79
555	-0.24	450.7	1.80	6.11
558	-0.26	462.1	1.79	6.14
590	-0.21	693.2	1.69	6.54
592	-0.23	886.7	1.69	6.79
633	-0.15	1245.8	1.58	7.13
664	-0.12	1902.9	1.51	7.55
713	-0.07	3616.3	1.40	8.19

Table A.4.9. NH_3 synthesis rate (r): Catalyst, 1wt%Ru/$Ce_{0.9}Sr_{0.1}O_{2-\delta}$; applied current, 6 mA; total flow rate, 240 SCCM; P_{H2}, 0.75 atom; total pressure, 0.1 MPa.

Catalyst bed temperature / K	Response voltage / kV	NH_3 synthesis rate / μmol g^{-1} h^{-1}	1000/T / K^{-1}	ln r / -
358	-0.18	208.6	2.79	5.34
361	-0.23	234.2	2.77	5.46
362	-0.24	238.4	2.76	5.47
377	-0.26	206.7	2.66	5.33
378	-0.27	217.7	2.65	5.38
380	-0.26	226.0	2.63	5.42
381	-0.29	230.9	2.63	5.44
385	-0.26	193.7	2.60	5.27
388	-0.27	216.4	2.58	5.38
405	-0.27	214.0	2.47	5.37
409	-0.27	204.2	2.45	5.32
413	-0.26	215.9	2.42	5.37
433	-0.25	207.9	2.31	5.34
435	-0.24	146.7	2.30	4.99
438	-0.25	156.9	2.28	5.06
441	-0.26	158.1	2.27	5.06
443	-0.21	119.7	2.26	4.78
445	-0.21	128.9	2.25	4.86
476	-0.21	138.1	2.10	4.93
476	-0.20	127.0	2.10	4.84
510	-0.19	115.4	1.96	4.75
513	-0.19	103.9	1.95	4.64
542	-0.16	94.1	1.85	4.54
543	-0.17	83.7	1.84	4.43
599	-0.05	253.7	1.67	5.54
599	-0.05	231.6	1.67	5.45
634	-0.02	508.2	1.58	6.23
640	-0.02	523.6	1.56	6.26
687	-0.02	1277.8	1.46	7.15
687	-0.02	1201.1	1.46	7.09

Table A.4.10. Ru particle sizes over 1wt%Ru/CeO_2, $Ce_{0.9}Al_{0.1}O_{2-\delta}$, and $Ce_{0.9}Sr_{0.1}O_{2-\delta}$.

Catalyst / -	Ru particle size / nm
1wt%Ru/CeO_2	2.05
1wt%Ru/$Ce_{0.9}Al_{0.1}O_{2-\delta}$	1.88
1wt%Ru/$Ce_{0.9}Sr_{0.1}O_{2-\delta}$	3.75

Table A.4.11. Specific surface area of CeO_2, $Ce_{0.9}Al_{0.1}O_{2-\delta}$, $Ce_{0.9}Sr_{0.1}O_{2-\delta}$.

Sample / -	Specific surface area / m^2 g^{-1}
CeO_2	25
$Ce_{0.9}Al_{0.1}O_{2-\delta}$	83
$Ce_{0.9}Sr_{0.1}O_{2-\delta}$	51

Table A.4.12. NH_3 synthesis rate (r): Catalyst, 1wt%Ru/CeO_2; applied current, 0 mA; total flow rate, 240 SCCM; P_{H2}, 0.75 atom; total pressure, 0.1 MPa.

Catalyst bed temperature / K	NH_3 synthesis rate / μmol g^{-1} h^{-1}	TOF-s / s^{-1}	1000/T / K^{-1}	ln r / -	ln TOF-s / -
580	335.0	0.004	1.73	5.81	-5.60
581	349.9	0.004	1.72	5.86	-5.56
631	1066.5	0.012	1.58	6.97	-4.44
632	951.1	0.010	1.58	6.86	-4.56
684	2713.0	0.030	1.46	7.91	-3.51
686	2337.2	0.026	1.46	7.76	-3.66
737	4286.2	0.047	1.36	8.36	-3.05

Table A.4.13. NH_3 synthesis rate (r): Catalyst, 1wt%Ru/$Ce_{0.9}Al_{0.1}O_{2-\delta}$; applied current, 0 mA; total flow rate, 240 SCCM; P_{H2}, 0.75 atom; total pressure, 0.1 MPa.

Catalyst bed temperature / K	NH_3 synthesis rate / μmol g^{-1} h^{-1}	TOF-s / s^{-1}	1000/T / K^{-1}	ln r / -	ln TOF-s / -
582	318.6	0.003	1.72	5.76	-5.74
583	283.9	0.003	1.72	5.65	-5.85
634	962.2	0.010	1.58	6.87	-4.63
634	843.4	0.009	1.58	6.74	-4.76
686	2288.2	0.023	1.46	7.74	-3.77
737	5089.3	0.051	1.36	8.53	-2.97

Table A.4.14. NH_3 synthesis rate (r): Catalyst, 1wt%Ru/$Ce_{0.9}Sr_{0.1}O_{2-\delta}$; applied current, 0 mA; total flow rate, 240 SCCM; P_{H2}, 0.75 atom; total pressure, 0.1 MPa.

Catalyst bed temperature / K	NH_3 synthesis rate / μmol g^{-1} h^{-1}	TOF-s / s^{-1}	1000/T / K^{-1}	ln r / -	ln TOF-s / -
583	230.7	0.005	1.71	5.44	-5.37
634	440.4	0.009	1.58	6.09	-4.72
686	1175.8	0.024	1.46	7.07	-3.74
686	1204.9	0.024	1.46	7.09	-3.72
738	2399.1	0.048	1.36	7.78	-3.03

Chapter 5 General Conclusion

Control of OH groups over the CeO_2 surface and its utilization for catalysis has been described throughout this thesis.

Chapter 2 described the tuning of interaction between H_2O and surfaces of CeO_2-based materials by heterocation doping. H_2O adsorption plays an important role in various catalyses related to surface H atom migration including surface protonics in the electric field. First, DFT calculations were performed. Then CeO_2 (111) surfaces doped with two heterocations were constructed. Results revealed differences in heterocation distribution. Heterocations with smaller ionic radii and smaller valences preferably adjoin mutually. The same trend was confirmed using XRD and Raman measurements. Secondly, heterocation-doping effects on H_2O adsorption were investigated using the optimized $Ce_{1-x}M_xO_{2-\delta}$ (111) surfaces. Results revealed that the H_2O–CeO_2 interaction was governed by the ionic radius of the heterocations. Surfaces doped with smaller heterocations present benefits for strong binding. Moreover, *in-situ* DRIFTS measurements were taken to confirm the suggestion from DFT calculations. Results show that the peaks derived from the stretching vibrations in O–H are red-shifted by doping of heterocations with smaller ionic radii. The validity of DFT-calculated results was confirmed.

Chapter 3 described the heterocation-doping effects on interaction between H atoms over lattice oxygen (O_{lat}-H^+) and CeO_2-based materials under a H_2 atmosphere. To separate possible heterocation-doping effects (*e.g.* heterocation-induced electron transfer, heterocation-induced lattice distortion, and adsorption-induced lattice distortion), DFT calculations with multiple flows were performed. The results indicate that electron-depleted lattice oxygen and lattice flexibility play important roles in the strong adsorption of H atoms. Electron-depleted lattice oxygen can be formed by doping of heterocations with low valences and small ionic radii. Doping of heterocations with smaller ionic radii provides a high degree of CeO_2 matrix flexibility. The DFT-suggestion was confirmed experimentally using XPS measurements.

Chapter 4 described the importance of the OH–CeO_2 interaction for catalysis in the electric field under H_2 atmosphere. NH_3 synthesis in the electric field was chosen as a model reaction. First, the temperature dependence of the synthesis rate in the electric field was considered. Results revealed the specific temperature dependence of the NH_3 synthesis rate during application of the electric field. Three regions were confirmed: The synthesis rate increased as the temperature decreased at around 373–573 K. Arrhenius-like behavior was confirmed in the other two regions ($T > 573$ K or $T < 373$ K). Findings reported herein show that NH_3 synthesis in the electric field proceeds *via* the "associative mechanism", where N_2H is formed from N_2 on active metals and O_{lat}-H^+ over supports. Therefore, *in-situ* FT-IR measurements were conducted to investigate the temperature dependence in O_{lat}-H^+ coverage over CeO_2. Consequently, O_{lat}-H^+ coverage increased concomitantly with the decrease in catalyst bed temperatures. Those results suggest the importance of O_{lat}-H^+ coverage in the catalysis in the electric field. The overall reaction rate in the electric field was formulated based on the inference described above. Then, the calculated values showed excellent agreement with the experimentally obtained values, elucidating the fundamentally important role of O_{lat}-H^+ coverage quantitatively. Finally, we studied the effects on the NH_3 synthesis rate obtained with control of O_{lat}-H^+ contents by doping. The NH_3 synthesis rate in the electric field at around 373–573 K increased by increasing the OH coverage with the addition of Al.

Through the work described in this thesis, the objectives listed below were achieved.

1. Elucidation of the controlling factors of interactions between H_2O and CeO_2: The ionic radius dominates the H_2O adsorption over CeO_2.
2. Elucidation of the governing factors of interactions between O_{lat}-H^+ atoms and CeO_2: Electron-deficiency of lattice oxygen and lattice flexibility plays an important role in H atom adsorption. Ionic radii and valences of heterocations strongly influence the controlling factors described above.
3. Elucidating the importance of O_{lat}-H^+ coverage on catalysis in the electric field under H_2 atmosphere: The increment of O_{lat}-H^+ coverage led to higher catalytic reactions in the electric field.

This knowledge can be a great milestone for the further development of catalysis related to OH groups.

Acknowledgement

I would like to express my sincere thanks to my supervisor, Prof. Yasushi Sekine (Waseda University). He guided me through discussions and gave me opportunities to try research in various fields including experiments and DFT calculations. I would like to express my gratitude to the referees of my doctoral thesis, Prof. Hiromi Nakai (Waseda University), Prof. Toshiyuki Momma (Waseda University), and Prof. Hideaki Tsuneki (Waseda University). They gave me valuable suggestions for my doctoral thesis. Prof. Nakai instructed me on DFT calculations. Prof. Momma gave me guide from the viewpoint of electrochemistry. Prof. Tsuneki has given me various proposals as a collaborator since he had worked at Nippon Shokubai Co., Ltd.

I would like to show my gratitude to Dr. Atsushi Ishikawa (National Institute for Materials Science). He gave me various suggestions for DFT calculations. I would like to show my greatest appreciation to Assistant Prof. Shuhei Ogo (Kochi University) for helpful suggestions on my research and collaborations in DFT calculations for polyoxometalate. I am deeply grateful to Associate Prof. Jeong Gil Seo (Hanyang Univesrity) for various suggestions on my research and collaborations in CO_2 capture and storage (CCS) using an external electric field. I owe my gratitude to Assistant Prof. Takuma Higo (Waseda University) and Assistant Prof. Tomohiro Yabe (University of Tokyo) for helpful on my research. I would like to express my appreciation to Ms. Masami Kawaharabata for the arrangement of the office procedures as a secretary in Sekine Laboratory.

I would like to be grateful to Mr. Masatoshi Ikeda (Nippon Shokubai Co., Ltd.), Mr. Hayahide Yamasaki (Nippon Shokubai Co., Ltd.), and Mr. Naomichi Haginiwa (Nippon Shokubai Co., Ltd.), who are the collaborations in NH_3 synthesis. They provided us financial supports and the design of the high-pressure reaction system.

This work was financially supported by JST-Mirai (Grant No. JPMJMI17E5). DFT calculations was conducted partly using the supercomputer system at the Information Initiative Center, Hokkaido University, Sapporo, Japan.

I would like to offer my special thanks to Mr. Hideaki Nakatsubo, Mr. Shota Manabe, Dr. Ryo Manabe, Ms. Ami Gondo, and Ms. Yukiko Kamite, who are the seniors in Sekine Laboratory. They instructed me when I was a student in Bachelor and Master course. Without their guidance, I would not have been able to achieve my results in doctoral course. Finally, I want to express my gratitude to all my colleagues: Mr. Yuta Tanaka, Mr. Ryuya Sakai, Mr. Yudai Hidai, Mr. Kazuharu Ito, Mr. Kenta Toko, Mr. Sasuga Hayashi, Mr. Yuta Mizutani, Mr. Hiroshi Sampei, and Ms. Sae Doi. Their help was essential to my research achievements.

Tokyo, December 2020

Kota Murakami

早稲田大学　博士（工学）　学位申請　研究業績書

(List of research achievements for application of doctorate (Dr. of Engineering), Waseda University)

氏 名　村上　洸太 (Kota MURAKAMI)

（As of January, 2021）

種 類 別 (By Type)	連名者（申請者含む）、題名、発表・発行掲載誌名、発表・発行年月 (name of authors inc. yourself, theme, journal name, date & year of publication)
Academic papers	
○	K. Murakami, Y. Mizutani, H. Sampei, A. Ishikawa, Y. Tanaka, S. Hayashi, S. Doi, T. Higo, H. Tsuneki, H. Nakai, Y. Sekine, Theoretical prediction by DFT and experimental observation of heterocation-doping effects on hydrogen adsorption and migration over CeO_2 (111) surface, *Phys. Chem. Chem. Phys.*, *in press*. DOI: 10.1039/D0CP05752E.
○	K. Murakami, Y. Tanaka, R. Sakai, Y. Hisai, S. Hayashi, Y. Mizutani, T. Higo, S. Ogo, J. G. Seo, H. Tsuneki, Y. Sekine, Key factor for the anti-Arrhenius low-temperature heterogeneous catalysis induced by H^+ migration: H^+ coverage over support, *Chem. Commun.*, 2020, **56**, 3365-3368.
○	R. Sakai, K. Murakami, Y. Mizutani, Y. Tanaka, S. Hayashi, A. Ishikawa, T. Higo, S. Ogo, H. Tsuneki, H. Nakai, Y. Sekine, Agglomeration Suppression of Fe-Supported Catalyst and its Utilization for Low-Temperature Ammonia Synthesis in an Electric Field, *ACS Omega*, 2020, **5(12)**, 6846-6851.
○	Y. Hisai, K. Murakami, Y. Kamite, Q. Ma, E. Vøllestad, R. Manabe, T. Matsuda, S. Ogo, T. Norby, Y. Sekine, First observation of surface protonics on $SrZrO_3$ perovskite under H_2 atmosphere, *Chem. Commun.*, 2020, **56**, 2699-2702.
○	K. Murakami, S. Ogo, A. Ishikawa, Y. Takeno, T. Higo, H. Tsuneki, H. Nakai, Y. Sekine, Heteroatom doping effects on interaction of H_2O and CeO_2 (111) surfaces studied using density functional theory: Key roles of ionic radius and dispersion, *J. Chem. Phys.*, 2020, **152**, 014707.
○	K. Murakami, Y. Tanaka, R. Sakai, K. Toko, K. Ito, A. Ishikawa, T. Higo, T. Yabe, S. Ogo, M. Ikeda, H. Tsuneki, H. Nakai, Y. Sekine, The important role of N_2H formation energy for low-temperature ammonia synthesis in an electric field, *Catal. Today*, 2020, **351**, 119-124.
○	K. Murakami, Y. Tanaka, S. Hayashi, R. Sakai, Y. Hisai, Y. Mizutani, A. Ishikawa, T. Higo, S. Ogo, J. G. Seo, H. Tsuneki, H. Nakai, Y. Sekine, Governing factors of supports of ammonia synthesis in an electric field found using density functional theory, *J. Chem. Phys.*, 2019, **151**, 064708.
○	K. Murakami, R. Manabe, H. Nakatsubo, T. Yabe, S. Ogo, Y. Sekine, Elucidation of the role of electric field on low temperature ammonia synthesis using isotopes, *Catal. Today*, 2018, **303**, 271-275.
	A. Gondo, R. Manabe, R. Sakai, K. Murakami, T. Yabe, S. Ogo, M. Ikeda, H. Tsuneki, Y. Sekine, Ammonia Synthesis Over Co Catalyst in an Electric Field, *Catal. Lett.*, 2018, **148(7)**, 1929-1938.
	R. Manabe, H. Nakatsubo, A. Gondo, K. Murakami, S. Ogo, H. Tsuneki, M. Ikeda, A. Ishikawa, H. Nakai, Y. Sekine, Electrocatalytic synthesis of ammonia by surface proton hopping, *Chem. Sci.*, 2017, **8**, 5434-5439.

早稲田大学　博士（工学）　学位申請　研究業績書

(List of research achievements for application of doctorate (Dr. of Engineering), Waseda University)

種 類 別 (By Type)	連名者（申請者含む）、題名、　発表・発行掲載誌名、発表・発行年月 (name of authors inc. yourself, theme, journal name, date & year of publication)
Reviews ○	K. Murakami, Y. Sekine, Recent Progress in Use and Observation of Surface Hydrogen Migration over Metal Oxides, *Phys. Chem. Chem. Phys.*, 2020, **22**, 22852-22863. M. Torimoto, K. Murakami, Y. Sekine, Low-temperature heterogeneous catalytic reaction by surface protonics, *Bull. Chem. Soc. Jpn.*, 2019, **92(10)**, 1785-1792.
Lectures	K. Murakami, Y. Tanaka, S. Hayashi, R. Sakai, Y. Hisai, S. Ogo, J. G. Seo, A. Ishikawa, H. Tsuneki, Y. Sekine, Insight into the governing factors for ammonia synthesis in the electric field using a DFT study, The 49th Petroleum-Petrochemical Symposium of JPIJS International Session, Yamagata, Japan, November 2019. (Oral) K. Murakami, Y. Tanaka, R. Sakai, T. Yabe, S. Ogo, Y. Sekine, Development of a Highly Efficient Ammonia Synthesis Using Base Metals in an Electric Field, 12th Natural Gas Conversion Symposium, Texas, America, June 2019. (Poster) K. Murakami, Y. Tanaka, R. Sakai, S. Ogo, T. Yabe, H. Tsuneki, M. Ikeda, A. Ishikawa, H. Nakai, Y. Sekine, Ammonia synthesis using base metal catalysts in an electric field, 17th Korea-Japan Symposium on Catalysis, Jeju, Korea, May 2019. (Oral) K. Murakami, R. Manabe, S. Ogo, T. Yabe, H. Tsuneki, M. Ikeda, A. Ishikawa, H. Nakai, Y. Sekine, Activation of N-N bond by surface protonics on Ru-support interface for ammonia synthesis at low temperature, The 8th Tokyo Conference on Advance Catalytic Science and Technology, Yokohama, Japan, August 2018. (Oral) K. Murakami, H. Nakatsubo, R. Manabe, Y. Hisai, A. Ishikawa, T. Yabe, S. Ogo, H. Tsuneki, M. Ikeda, H. Nakai, Y. Sekine, Low temperature catalytic ammonia synthesis in an electric field, 2018 International Symposium on Advancement and Prospect of Catalysis Science & Technology, July 2018. (Oral) K. Murakami, H. Nakatsubo, R. Manabe, Y. Kamite, Y. Hisai, A. Ishikawa, T. Yabe, S. Ogo, H. Tsuneki, M. Ikeda, Y. Sekine, Reaction mechanism of ammonia synthesis by surface proton hopping over catalyst surface, TAILOR2018, Ystad, Sweden, June 2018. (Poster) K. Murakami, H. Nakatsubo, R. Manabe, S. Ogo, H. Tsuneki, M. Ikeda, Y. Sekine, Low temperature catalytic ammonia synthesis in electric field, Florence, Italy, August 2017. (Oral) K. Murakami, H. Nakatsubo, R. Manabe, S. Ogo, H. Tsuneki, M. Ikeda, Y. Sekine, Low temperature catalytic ammonia synthesis in an electric field, 16th Korea-Japan Symposium on Catalysis, Sapporo, Japan, May 2017. (Oral) (Other 6 lectures in Japan)

早稲田大学　博士（工学）　学位申請　研究業績書

(List of research achievements for application of doctorate (Dr. of Engineering), Waseda University)

種 類 別 (By Type)	連名者（申請者含む)、題名、　発表・発行掲載誌名、発表・発行年月 (name of authors inc. yourself, theme, journal name, date & year of publication)
Other Publications	K. Toko, K. Ito, H. Saito, Y. Hosono, K. Murakami, S. Misaki, T. Higo, S. Ogo, H. Tsuneki, S. Maeda, K. Hashimoto, H. Nakai, Y. Sekine, Catalytic Dehydrogenation of Ethane over Doped Perovskite via the Mars–Van Krevelen Mechanism, *J. Phys. Chem. C*, 2020, **124(19)**, 10462-10469. T. Yabe, K. Yamada, K. Murakami, K. Toko, K. Ito, T. Higo, S. Ogo, Y. Sekine, Role of Electric Field and Surface Protonics on Low-Temperature Catalytic Dry Reforming of Methane, *ACS Sus. Chem. Eng.*, 2019, **7(6)**, 5690-5697. K. Takise, A. Sato, K. Murakami, S. Ogo, J. G. Seo, K. Imagawa, S. Kado, Y. Sekine, Irreversible catalytic methylcyclohexane dehydrogenation by surface protonics at low temperature, *RSC Adv.*, 2019, **9**, 5918-5924. S. Ogo, H. Nakatsubo, K. Iwasaki, A. Sato, K. Murakami, T. Yabe, A. Ishikawa, H. Nakai, Y. Sekine, Electron-Hopping Brings Lattice Strain and High Catalytic Activity in the Low Temperature Oxidative Coupling of Methane in an Electric Field, *J. Phys. Chem. C*, 2018, **122(4)**, 2089-2096. 村上 洸太, 関根 泰, 低温で化学反応が速く進む手法を世界で初めて発見, 自動車技術, 2020, 104-105. 村上 洸太, 関根 泰, オンデマンド・低温で駆動可能なアンモニア合成プロセスのための触媒開発, 化学工業, 2019, **70(11)**, 46-51. 村上 洸太, 関根 泰, アンモニア合成法の最新動向, 現代化学, 584, 30-33 (2019) 田中 雄太, 村上 洸太, 関根 泰, 卑金属触媒を用いた低温電場アンモニア合成, ファインケミカル, 2019, **48(9)**, 12-18. 村上 洸太, 関根 泰, 電場触媒反応を利用した低温域で進むアンモニア合成, 化学工業, 2018, **6**, 403-408. 村上 洸太, 関根 泰, 表面プロトニクスによる低温アンモニア合成, ファインケミカル, 2017, **12**, 15-22.